Hydrodynamic drag reduction in turbulent boundary layer flow using riblets

S. Bezuijen

Experimental studies in the cavitation tunnel

P&E report no.:2815

Hydrodynamic drag reduction for turbulent boundary layer flow using riblets

by

S. Bezuijen

to obtain the degree of Master of Science
at the Delft University of Technology,
to be defended publicly on Monday April 10, 2017 at 14.00 PM.

Student number: 4090829
Project duration: November 24, 2015 - April 10, 2017
Thesis committee:

Prof. Dr. ir. J. Westerweel	Delft University of Technology
Dr. ir. W.-P. Breugem	Delft University of Technology
Dr. Ir. G.H. Keetels	Delft University of Technology
Ir. O.W. Salomons	Océ Technologies B.V.
Ir. H.O.G. Benschop	Delft University of Technology

TU Delft

Abstract

Reducing the hydrodynamic drag of marine vessels is a key approach to decrease energy consumption. In addition to saving fuel costs, this also decreases greenhouse gas emissions. One possible method to reduce turbulent drag for a ship is coating its hull with riblets. Riblets are micro-fabricated structures whose design is based on shark skin. Earlier riblet studies have reported maximum drag reduction of 10%.

The goal of the present work is to accurately measure the drag of 3 different riblet coatings in the cavitation tunnel. This setup, located at the Ship Hydromechanics group of the TU Delft generates a turbulent boundary layer for freestream velocities between 0.3 and 3.5 $[\frac{m}{s}]$.

Two steps were taken to achieve this goal. Firstly an accurate measurement procedure was developed, which allows 1% accurate drag reduction studies in the cavitation tunnel. This procedure is then subsequently used to study the 3 different riblet coatings. These were provided by Fraunhofer IFAM and Océ, who used a mould pressing and elevated printing technology respectively.

Cavitation tunnel measurements were analysed using the propagation of uncertainty and Particle Imaging Velocimetry[PIV]. The former determines the contribution of individual measuring sensors to the uncertainty of the measured drag reduction. It was found that the velocity and drag force require the longest measuring time to guarantee statistically converged results. PIV studies were used to determine the correct magnitude of the freestream velocity, as the pressure sensor of the cavitation tunnel systematically overestimated the freestream velocity.

Measurements for the supplied coatings showed drag reduction for all plates. For Fraunhofer IFAM maximum drag reduction amounted to 7%, while for Océ this value is 5%. Comparing with values from literature shows slight under performance. This is presumably caused by small manufacturing effects on the riblet surface.

To improve current work, the velocity region where accurately can be measured must be enlarged. This is because the expected optimal performance for the Océ and Fraunhofer IFAM coatings are located before and beyond this region respectively. For the low limit velocities, small ranged force and velocity sensors should provide more accurate results. For high velocities entrained air must be removed from the setup. This can be done using a vacuum pump, although more analyses on this system is required as the measured drag is affected by this device.

Nomenclature

Acronyms

ACF	autocorrelation function
FOV	Field of view
PIV	Particle image velocimetry
PSD	power spectral density
SEM	scanning electron microscope
TBL	Turbulent boundary layer
TCS	Turbulent coherent structures

Symbols

u	streamwise velocity at wall normal distance y	$\frac{m}{s}$
α	volumetric expansion coefficient	$\frac{1}{\mathrm{T}}$
β	Clauser parameter	—
δ^*	displacement thickness	m
δ^{99}	TBL thickness based on 99% criteria	m
δ_ν	w	
δ_x	TBL thickness	m
ϵ	wall rougness	m
γ	wall intercept	-
κ	von Kármán constant	-
μ	dynamic viscosity	$\frac{\mathrm{kg}}{\mathrm{ms}}$
μ_x	uncertainty of variable x	—
ν	kinematic viscosity	$\frac{\mathrm{m}^2}{\mathrm{s}}$
$\overline{U}$	Average test section velocity	$\frac{\mathrm{m}}{\mathrm{s}}$
ρ	fluid density	$\frac{\mathrm{kg}}{\mathrm{m}^3}$
ρ_0	reference density	$\frac{\mathrm{kg}}{\mathrm{m}^3}$

ρ_{ij}	Pearson correlation coefficient	–
ρ_p	tracer particle density	$\frac{\mathrm{kg}}{\mathrm{m}^3}$
τ_{wall}	wall shear stress	$\frac{\mathrm{N}}{\mathrm{m}^2}$
θ	momentum thickness	m
A	test plate surface	m^2
C_D	drag coefficient	–
d_p	tracer particle diameter	m
DC	drag change	–
dx	vector spacing PIV	m
F_D	drag force	N
H	shape factor	–
L	test plate length	m
M	magnification factor	–
N_{PIV}	number of paired snapshots	s
Re_L	Reynolds number	–
$Re_L(U_\infty)$	Reynolds number based on $\overline{U}$	m
s	riblet spacing	m
s^+	Karman number	–
S_{t_p}	tracer particle Stokes number	–
T	temperature	°C
t_{int}	difference time scale	s
t_{int}	interrogation time scale	s
t_{PIV}	measurement time PIV	s
t_p	tracer particle time scale	s
u^+	scaled streamwise wall velocity	–
U_∞	contraction exit velocity	$\frac{\mathrm{m}}{\mathrm{s}}$
u_τ	wall shear velocity	$\frac{\mathrm{m}}{\mathrm{s}}$
U_{pos}^{FOV}	PIV recorded velocity for field of view at position	$\frac{\mathrm{m}}{\mathrm{s}}$
W	test plate width	m
y	wall normal distance	m
$\triangle P$	differential pressure	$\frac{\mathrm{N}}{\mathrm{m}^2}$

Contents

List of Figures

List of Tables

Chapter 1

Introduction and outline

This chapter presents a general introduction into the thesis. First the motivation for the work is presented, which is closely related to the objectives of the SEAFRONT project. This EU sponsored project is a collaboration of 19 partners, who aim to limit the growth of biofouling while simultaneously reduce the hydrodynamic drag for marine vessels.
One of these partners Fraunhofer IFAM, provided two mould pressed coatings that reduced the drag and two which possessed additional anti fouling properties. Another company Océ, outside the SEAFRONT project, also provided a drag reducing coating, which was produced using an inkjet printing technique.
All provided coatings were manufactured according to a riblet design, which is shortly introduced in the next section. Riblets are a specific form of orientated roughness, which have shown the ability to reduce drag in turbulent flows. This section also treats the manufacturing process of the Fraunhofer IFAM and Océ riblets.
To determine the drag reduction of all coatings, accurate measurements are required. This is discussed in the next section, which introduces the measuring setup and the research objectives. The chapter concludes with an outline of the thesis structure.

1.1 Motivation

The United Nations climate change Paris agreement [UN, 2015], signed by all world major countries, states the agreement between all participants to keep global temperature rise below 2°C.
To achieve this challenging goal, a great emphasis is made on reducing greenhouse emissions on a global scale. Besides proposed transitions to sustainable energy sources, a need for more efficient appliances is urged as well.
The EU sponsored SEAFRONT project can be categorized in the latter. Its main goal is to develop coatings for marine purposes that limit biofouling, while simultaneously reducing the drag. Biofouling is the attachment and growth of an bio-layer of organisms to a surface, see fig. 1.1. This rough layer causes an increase in drag, which is an undesired effect that increases fuel costs and greenhouse gas emissions.

Figure 1.1: Severe case of biofouling, with the waterline clearly visible[Marengo, 2017]

The work in this project does not study the anti-fouling but the drag reducing properties of coatings delivered by SEAFRONT partner Fraunhofer IFAM. This company provided 4 mould pressed coatings, two which only reduce drag and two with additional anti fouling properties. Another company outside the SEAFRONT project, Océ also provided a drag reducing coating. All coatings are manufactured with a riblet surface, which is discussed next.

1.2 Riblets

Textbook theory shows that drag increases for wall bounded flows when the surface is rough. One clear example is the mentioned biofouling, which generates a roughness layer on top of the smooth hull. However, micro-fabricated roughness has proven to reduce drag for specific flow conditions.
A pioneering study that showed ordered roughness could reduce drag was by Walsh [1983]. Using micro-milling, a texture similar to the one in fig. 1.2 was produced. When the drag was measured for this texture and compared against a smooth surface, it was found this texture yielded a lower flow resistance.

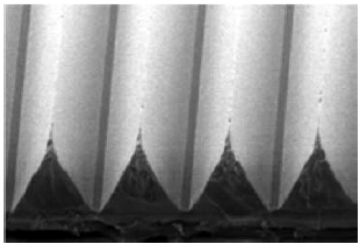

Figure 1.2: Riblets similar to Walsh [1983] from a reproducing study by Koeltzsch et al. [2002]

As a result from this finding, riblets structures where thoroughly investigated the next decade. The most thorough work was produced by Bechert et al. [1997], who performed an optimisation study. He found that the most effective riblets had a thin fence like cross section, with very sharp tips.
The riblet coatings studied in this work are not fence like, but trapezoidal shaped for which Bechert et al. [1997] measured a maximum drag reduction of 8%. This cross section was chosen because of its relative easy to manufacture.

1.3 Research objectives and thesis scope

To analyse the supplied coatings mentioned above, drag measurements were performed in the cavitation tunnel at the Ship Hydromechanics group, see fig. 1.3. Because the property of interest is drag reduction, very accurate measurements of force, velocity and temperature are essential.

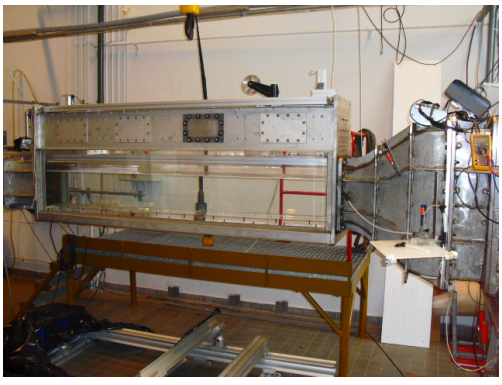

Figure 1.3: Cavitation tunnel

To achieve this, specific measuring routines and times are required to reduce the uncertainty and eliminate as much systematic bias as possible. This proved to be a significant challenge, resulting in the first research objective

1. Develop an accurate drag plate measurement procedure that allows 1% precise drag reduction studies at the TU Delft cavitation tunnel

which is done by analysing the velocity, force and temperature measurements separately. Also various tests into bias influences are performed.
In addition the flow is studied as well, because riblets only reduce drag for a limited velocity range and specific flow conditions. One essential condition for drag reduction is turbulent flow, which is confirmed using flow imaging techniques.

Once the setup and flow are thoroughly analysed, the mentioned coatings from Fraunhofer IFAM and Océ can be measured, yielding the second objective

2. Measure and analyse the drag reduction from the Fraunhofer IFam and Océ plates, using the developed measurement procedure in this work

which also includes the evaluation of Fraunhofer IFAM and Océ plates that only reduce drag against the literature values of Bechert et al. [1997]. This is important as it validates the setups ability to reproduce literature references.

1.4 Outline

The remainder of the thesis is as follows. First a literature study regarding riblets and turbulent boundary layer flow is given. It also contains a short section into coherent flow structures, which are closely linked to the drag reducing mechanism of riblets. Although a full treatment is beyond the scope of this work, visualisation of the flow helps understanding this mechanism.
Chapter 3 analyses the cavitation tunnel and its instrumentation. The individual uncertainty contributions of the velocity, force and temperature to the overall accuracy are analysed, using the propagation of uncertainty. This tool also allows the determination of the required measuring time for statistically converged results. This chapter concludes with qualitatively analysing several bias errors and discussing the reproducibility of the measured results.
Chapter 4 treats the second part of research objective 1 by analysing the flow in the tunnel. Using *Particle Imaging Velocimetry*; the mean flow, boundary layer and the near wall flow are measured. The latter can be used to obtain local estimates of the drag force and reduction.

With chapter 3 and 4 devoted to answering research objective 1, the second question is treated in chapter 5. First the riblets by Fraunhofer IFAM and Océ that do not possess the anti fouling property are measured. Once these are compared to Bechert et al. [1997], the anti fouling plates are discussed as well.

Every chapter ends with discussing the results and relates them to the corresponding research question. Chapter 6 summarizes all these findings and treats both research questions. It also gives recommendations to improve current work and suggestions for further research.

Chapter 2

Literature study and theoretical background

This literature study aims to present a comprehensive introduction into the topic of drag reduction by riblets. To achieve this, the chapter comprises 3 sections.

First the textbook theory of the turbulent boundary layer [TBL] is recapped. Using the law of the wall, the effect of roughness on both near wall velocity and drag is explained. According to classical theory, roughness always has a drag increasing effect.
The second section contradicts this modeling by introducing riblets. These are a specific form of ordered roughness that have been proven to reduce drag for certain flow conditions. This mechanism is discussed next, which is closely related to the physics of the TBL. One important aspect is the study of turbulent coherent structures [TCS]. Though a full treatment of this subject is beyond the scope of this work, some basic thoughts and understanding helps visualize the flow around riblets.
Most riblet studies have been performed under developed flow conditions, such as pipe or duct flow. Because in this thesis project riblets are studied for TBL conditions, the second part concludes with discussing the few works that have done similar studies.

The chapter concludes with the most recent developments in riblet research. With increasing precision in micro production industry, research has started to produce even more specific riblets such as the 'herringbone' riblet. It also discusses the FIK identity, which allows the decomposition of the surface drag in several components.

2.1 Turbulent boundary layer

As measurements are performed for TBL conditions it is important to understand the basic physics of this flow. This traces back to the earliest days of fluid mechanics and has now become text book knowledge. The theory presented here, unless otherwise stated, has been drawn from Nieuwstadt [1992], White [1999] and Pope [2001].

2.1.1 Canonical description of the smooth wall TBL

Since the concept of a boundary layer was introduced by Ludwig Prantdtl in 1904, research has been ongoing to apply it to turbulent flows. The main challenge is that the flow properties are statistic in contrast to laminar boundary layer flow for which the analytical Blasius solution can be derived. Theodore van Kármán introduced a model in 1930 that has now become an essential part for every turbulence class.
First the boundary layer is divided into two domains. An inner layer where viscous effects dominate, and an outer layer that is dominated by turbulence. The velocities in these regions are described by the "Law of the wall". They are connected by the log law in the overlap region, implying the velocity increases logarithmically with the wall distance.

$$
\begin{aligned}
u^+ &= \frac{1}{\kappa} \ln y^+ + \gamma \\
u^+ &= \frac{u}{u_\tau} \quad y^+ = \frac{y u_\tau}{\nu}
\end{aligned}
\tag{2.1}
$$

Here u is the mean streamwise velocity at wall distance y and u^+ ,y^+ are the respective non-dim. quantities. u_τ is the wall friction velocity, ν the kinematic viscosity, κ the von Kármán constant and γ the wall intercept, which is a constant representing the wall roughness. When the wall is considered "smooth", γ equals 5. The log law is valid for the interval $30 \leq y^+$ and $y \leq 0.3\delta$, where δ is the boundary layer thickness.

Neglecting surface effects, eq. 2.1 is closed by determining u_τ and κ. The latter is determined from experiments and usually chosen within range $0.38 \leq \kappa \leq 0.42$. u_τ is obtained by the following formula:

$$
u_\tau = \sqrt{\frac{\tau_{wall}}{\rho}} \tag{2.2}
$$

where τ_{wall} is the wall shear stress and ρ is the density. The local shear stress, $\tau_{wall}(x)$ can be determined by using Prandtl's assumption regarding the boundary layer growth:

$$
\begin{aligned}
\delta_x &= 0.16 \frac{x}{Re_x^{\frac{1}{7}}} \\
Re_x &= \frac{U_\infty x}{\nu}
\end{aligned}
\tag{2.3}
$$

Which models the boundary layer thickness δ_x by a one-seventh power law related to the Reynolds number. Re_x for TBL is based on the freestream velocity U_0, the distance from the leading edge of plate x and ν. Eq. 2.3 assumes δ_0=0, for which τ_{wall} is given by:

$$
\tau_{wall}(x) = 0.0135 * (\rho\nu)^{\frac{1}{7}} \rho^{\frac{6}{7}} U_\infty^{\frac{13}{7}} x^{-\frac{1}{7}} \tag{2.4}
$$

From which it can be seen τ_{wall} decreases, and thus u_τ, as the distance from the leading edge increases. With u_τ known the boundary layer at every position can now be scaled by eq. 2.1, see fig. 2.1. It shows the log law against measured velocities for a smooth wall.

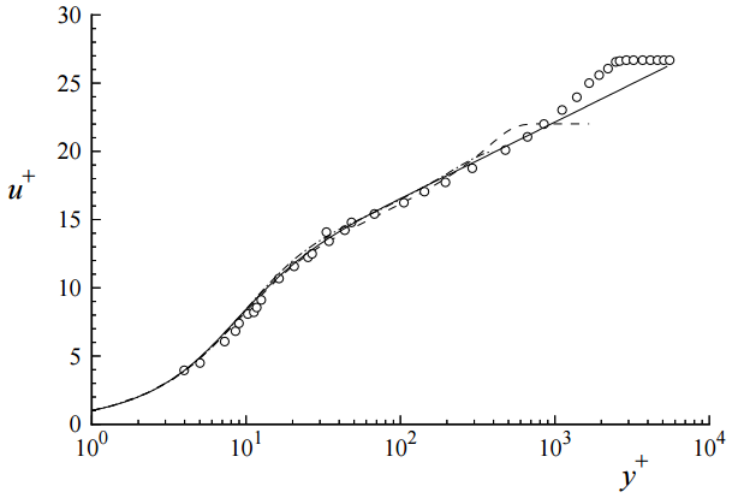

Figure 2.1: Scaled streamwise velocity [Pope, 2001]

By integrating the local wall shear stress over the plate's surface the integral drag force can be computed:

$$F_D = W \int_0^L \tau_{wall}(x) \mathrm{d}x \tag{2.5}$$

Where L and W are the plate's length and width respectively. Which can be used to define the drag coefficient:

$$C_D = \frac{2F_D}{\rho U_0^2 LW} \tag{2.6}$$

If the TBL starts at the leading edge, δ_0=0, eq. 2.4 can be inserted into eq. 2.6 given the expression:

$$C_D = \frac{0.031}{Re_L^{\frac{1}{7}}} \tag{2.7}$$

2.1.2 Canonical treatment of roughness

When a surface cannot be considered smooth, the wall intercept is given by:

$$\begin{aligned} \gamma &= 2.5 \ln \frac{\epsilon u_\tau}{\nu} + 5 \\ \text{smooth} : \frac{\epsilon u_\tau}{\nu} &\leq 1 \qquad \text{rough} : \frac{\epsilon u_\tau}{\nu} \geq 1 \end{aligned} \tag{2.8}$$

which non dimensionalizes its roughness ϵ in similar fashion to y. Corresponding to one of the given limits, the surface is either hydrodynamically smooth or rough. For classical cases, where ϵ is considered positive it can be seen from equations 2.8 and 2.1 that the intercept and therefore u^+ in the log layer increases.
Fig. 2.2 shows the effect of roughness on C_D. It displays the drag curve for a smooth wall, corresponding to eq. 2.6. From its curve several branches representing decreasing roughness, $\frac{L}{\epsilon}$ are given.
If roughness becomes important, the corresponding C_D is increased and becomes constant with increasing Re_L. This represent the limit where $\frac{\epsilon u_\tau}{\nu} \longrightarrow \infty$ and viscous effects on C_D become negligible.
Fig. 2.2 also displays a transition region, which represents a TBL which does not originate at the leading edge. In that case the boundary layer starts laminar at the leading edge of the plate. Once local Re_x becomes sufficiently high, it transitions to turbulence. C_D is then also determined by a small laminar contribution, which lowers the overall drag coefficient.

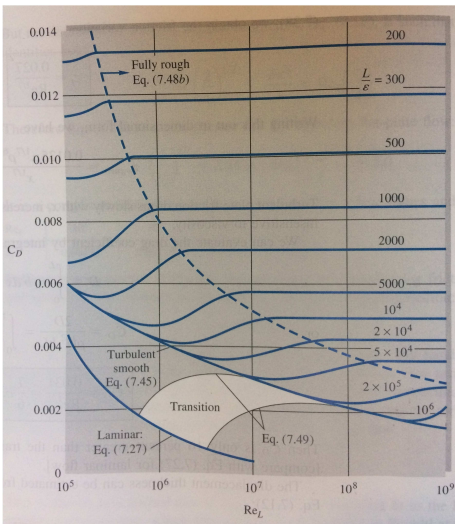

Figure 2.2: C_D for smooth and rough TBL [White, 1999]

2.2 Riblets

The theory described in the former section dates from a time when micro fabrication was non existent. Therefore roughness was modeled as an isotropic distribution. With the development of techniques such as honing, inkjet printing and laser ablation it is possible to manufacture surfaces with anisotropic 'orientated' roughness. Marusic et al. [2010] gives an overview for several pipe flow tests which where honed with specific orientation. These experiments show that the typical increase in C_D becomes more complex, indicating the previous modeling of the TBL is insufficient to capture this behaviour.

2.2.1 Conventional riblets

The idea that anisotropic or ordered roughness could actually reduce drag was conceived in the 70's. Caused by the oil crisis, reduced fuel consumption was essential. Walsh [1983] gave one of the first studies that showed that riblets were able to reduce drag, although by a small percentage. Riblets in his and other mentioned studies are small fences with varying cross section alligned to the flow, see figures taken respectively from Bechert et al. [1997] and Koeltzsch et al. [2002].

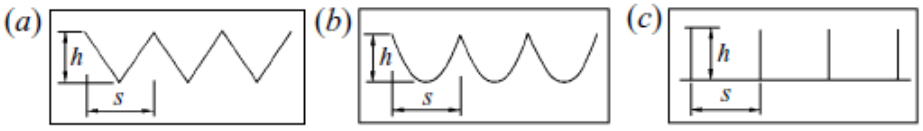

Figure 2.3: Various riblet cross sections[Bechert et al., 1997]

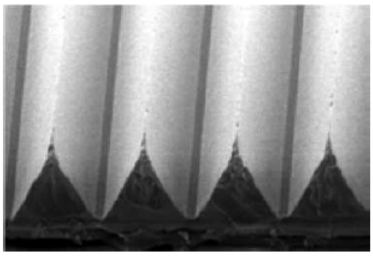

Figure 2.4: Surface covered with riblets [Koeltzsch et al., 2002]

The experiments of Walsh [1983] where performed for the cross sections a) and b) in fig.2.3 in fully developed channel flow. During the late 90's the group of Bechert in Germany performed many tests trying to improve riblet drag reduction. In 1997 they produced their thorough study in which they not only reproduced, but also improved the early results by Walsh as can be seen in fig. 2.5.

In these figures the drag change is plotted against the Karman number which has now become the convention for displaying riblet performance. The Karman number can be expressed as:

$$s^+ = \frac{su_\tau}{\nu} \tag{2.9}$$

Where s is the riblet spacing, see fig. 2.5. The drag change, DC, is given as the percential ratio of the wall shear stress τ_{riblet} measured with the riblet case and the reference wall shear stess τ_0 for the smooth wall:

$$\begin{aligned} DC &= \frac{\triangle\tau}{\tau_0} \\ \triangle\tau &= \tau_0 - \tau_{smooth} \end{aligned} \tag{2.10}$$

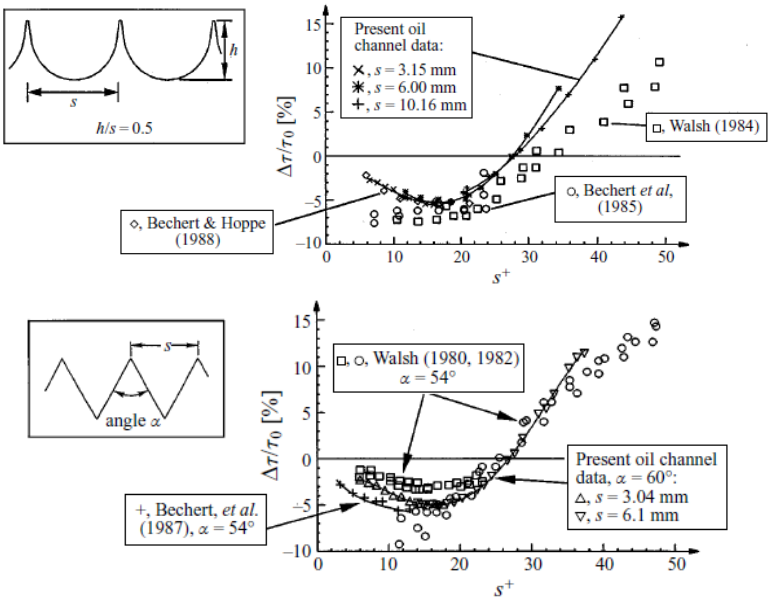

Figure 2.5: Results from Walsh and Bechert [Bechert et al., 1997]

The results in fig. 2.5 show that riblet performance varies as s^+ changes by varying u_τ. An optimum in drag reduction can be seen around s^+=17 and this value has become a guideline for riblet design and optimisation.
Bechert et al. [1997] also investigated various crossections as shown in figures 2.5 and 2.6. They found that for blade riblets in fig. 2.6 gave the best performance, reducing drag by almost 10%.

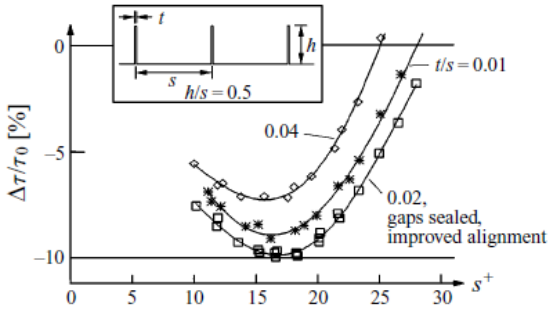

Figure 2.6: Optimal drag reduction for riblets [Bechert et al., 1997]

2.2.2 Drag causing mechanism of the TBL

The designer rules given in the former subsection leave a fundamental question unanswered: *"How do riblets decrease drag?"*. This is inseperable from the more general question:*"What generates the substantial drag increase inside the TBL compared to its laminar counterpart?"*
Although this question has not yet been resolved, consensus within the scientific community lies that turbulent coherent structures play a key part. Robinson [1991] describes these as:
"Coherent structures are regions of flow over which at least one fundamental flow variable displays strong correlation with itself, or another variable over a range of space/time which is significantly larger than the smallest flow scale."

TCS have been studied since for nearly halve a century. To discuss all research since then surpasses the scope of this work, therefore interested readers are referred to Robinson [1991], Marusic et al. [2010] and Nugroho [2015] for more details. This section will introduce the two coherent structures that are mostly coined with riblet performance, namely:

1. *Near wall streaks*
2. *Hairpin vortices*

which will be explained concept wise followed up by their relation with drag increasing/reducing behaviour. This will then be coupled to current riblet research.

Near wall streaks

Near wall streaks were the first phenomena that were discovered in the TBL by Kline et al. [1967]. In a series of works using hydrogen bubble flow visualization they investigated the viscous sublayer. Instead of the assumed laminar behaviour they discovered the behaviour in fig. 2.7
It shows regions, which they called streaks, of low speed occupying the sublayer. These streaks seemed to be be lifted up from the near wall region, burst and then grow away from the wall. They proposed a model that discussed the streak formation for which they used the concept of vortex elements. These streaks seemed to be be lifted up from the near wall region, burst and then grow away from the wall. They also proposed a model that discussed the streak formation for which they used the concept of vortex elements.

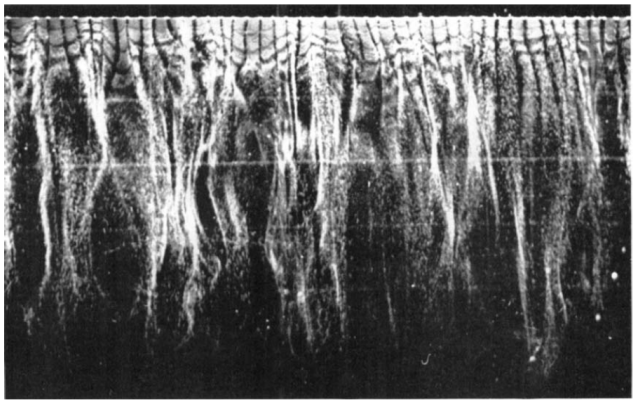

Figure 2.7: Streaks in the viscous region at $y^+ = 2.7$ [Kline et al., 1967]

This model was gradually expanded with the discovery of sweeps, which are regions where fluid with higher velocity are transported towards the wall, by Corino and Brodkey [1969]. Latter also found that ejection described by Kline et al. [1967] accounts for 50-70 % of the turbulence production.
A few years later Kline et al. [1967] first mentioned that streaks could be part of a larger streamwise regenerative cycle. They also mention possible interaction between the streaks and near-wall vorticity.

Hairpin vortices

This last proposition was actually an attempt to combine results with the vorticity models proposed by Theodorsen [1952] and Townsend [1956]. Visualizations of their hairpin/horse-shoe and attached eddy hypothesis can be seen in fig. 2.8. Both realised that the vorticity in the turbulent boundary layer commonly can be identified as a horseshoe/hairpin shape. Both modeled a coherent structure which originates from the viscous region and is lifted up from the surface.
Due to limitations in flow measuring techniques, it took over 30 years before these structures were actually visualized. Nugroho [2015], Panton [2001] and Robinson [1991] give a good overview of the many research that was performed the last decades. Robinson [1991] also proposed a model which relates hairpin formation to the near wall streaks and sweeps given in fig. 2.9.

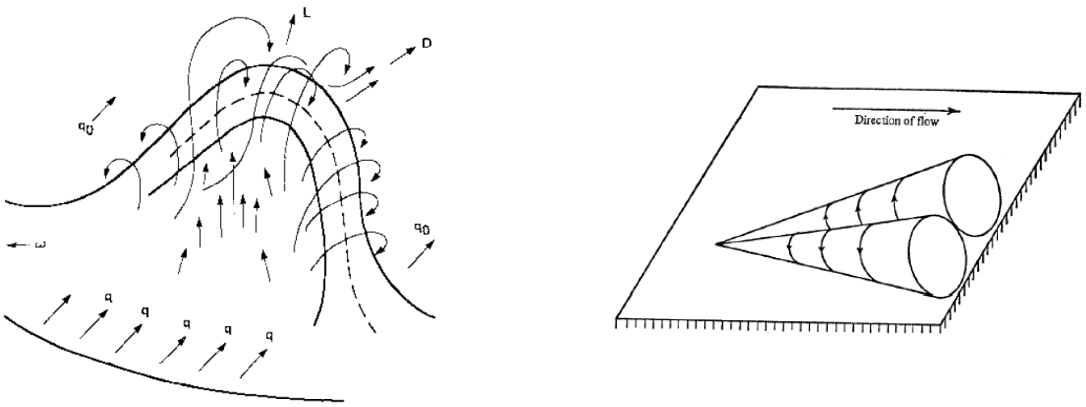

Figure 2.8: Left : Harpin vortex model by Theodorsen [1952]
Right : Attached eddy hypothesis by Townsend [1956]

In this model quasi-streamwise vortices form in the near wall region, which are related to the near wall streaks and sweeps. From the near wall into the wake region these streamwise vortices arc up and organize themselves into arch-like structures which finally form the hairpins.

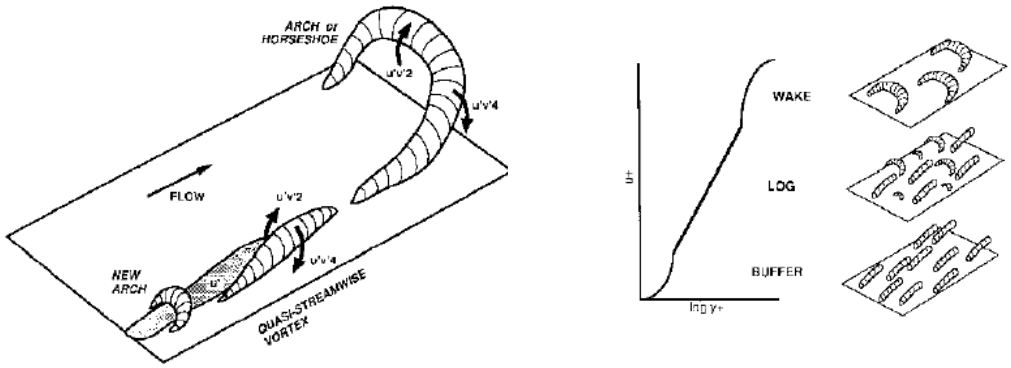

Figure 2.9: Hairpin vortices formation [Robinson, 1991]

Relation of coherent structures to drag

Besides origin and formation, the contribution of hairpins and the sweeps/jets to the drag has been investigated. Orlandi and Jimenez [1994] showed numerically and analytically that for moderate Re_x, sweeps and jets in the turbulent boundary layer increase the drag. This is caused by an increase of turbulent transport of momentum towards the wall by these structures.
A similar analysis was made by Kim [2011], who proposed a qualitative model. Based on this model, he concluded that if the drag is to be decreased, the formation of structures in fig. 2.9 has to be disrupted/hampered. As the near wall velocity streaks are related to the described phenomena, this will also influence the hairpin vortices.
Studies that deal with decreasing the drag from the coherent structures viewpoint are the works of Kim et al. [2008] and Tamano et al. [2014]. Both alter the flow occurring in the TBL by injection of polymer or usage of non-ionic fluid respectively. Both observe similar behaviour for the drag reducing case; suppression of hairpin packet formation and near wall jets and sweeps. This further supports the model and suggestion made by Kim [2011].

2.2.3 Drag reducing mechanism of riblets

The drag reducing property of riblets was discussed in the first section. The main mechanism causing this effect has not yet been resolved. Walsh [1983] stated the main thought that riblets hinder the formation of streaks and sweeps in the near wall region. As observed by Orlandi and Jimenez [1994] it is thought that the turbulent production in this region is the main source for skin friction.
Because riblets hinder the spanwise movement, it is believed that this hampers or damps the formation of the streamwise streaks and therefore reduces drag. Bechert and Bartenwerfer modeled this by introducing the protrusion height in 1989. The protrusion height can be defined as the difference in offset between the spanwise and the streamwise flow, see fig. 2.10. Luchini et al. [1991] refined this model and derived an analytical solution for the drag change for the limit case, $\lim_{s^+ \to 0} DC$.

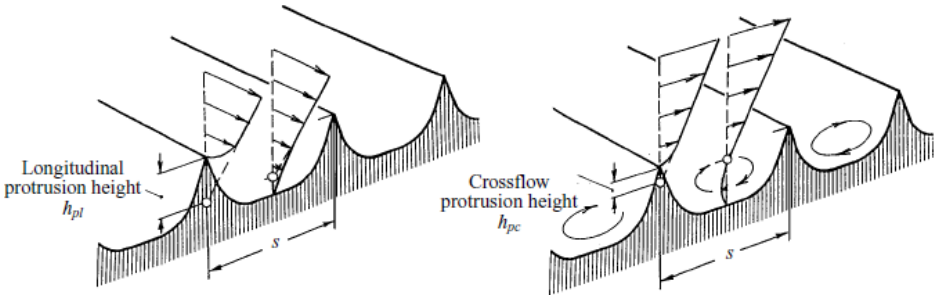

Figure 2.10: Protrusion height concept as introduced by Luchini [Bechert et al., 1997]

In their major work, Bechert et al. [1997] compared the analytical expression from Luchini et al. [1991] with their results for various cross sections with varying protrusion height, given in fig. 2.11. Although a good match in slopes is observed for the viscous regime, Luchini's method does not give an optimization for riblet design. Main reason is the difficulty of determining the correct protrusion height, which varies with the riblet geometry. However as Bechert et al. [1997] mention, it can be used as a guideline for first design.

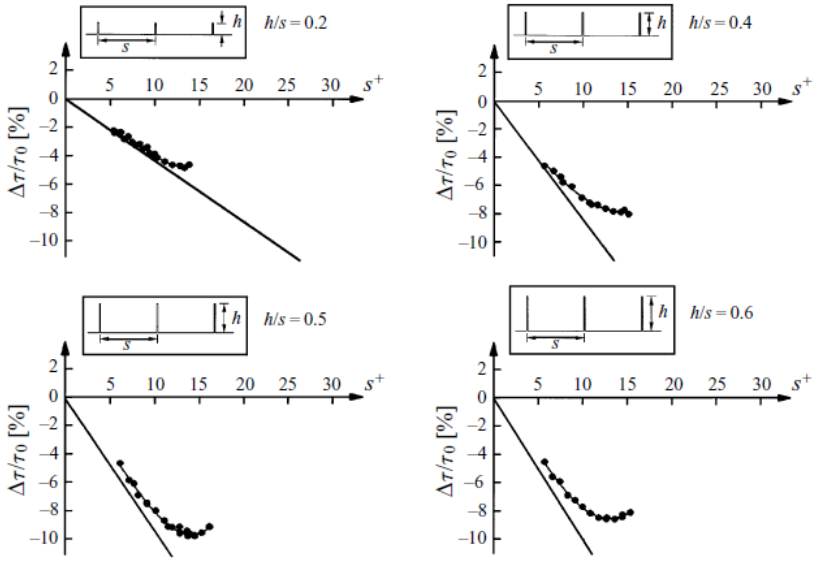

Figure 2.11: Results from Bechert with initial drag slope by Luchini (Bechert et al. [1997])

More recently, Garcia-Mayoral and Jimenez [2011] produced a paper in which they investigate the deterioration of riblet performance past the optimum of s^+=17. Currently the scientific opinion on this matter can be divided into two groups.
The first group argues that as s^+ increases the generation of secondary streamwise vortices over the riblets cause an increase in Reynolds shear stress and thus the drag. There are however works, such as those of Jung et al. [1992] that challange this view by showing that spanwise oscillation of the wall can decrease drag by inducing streamwise motion.

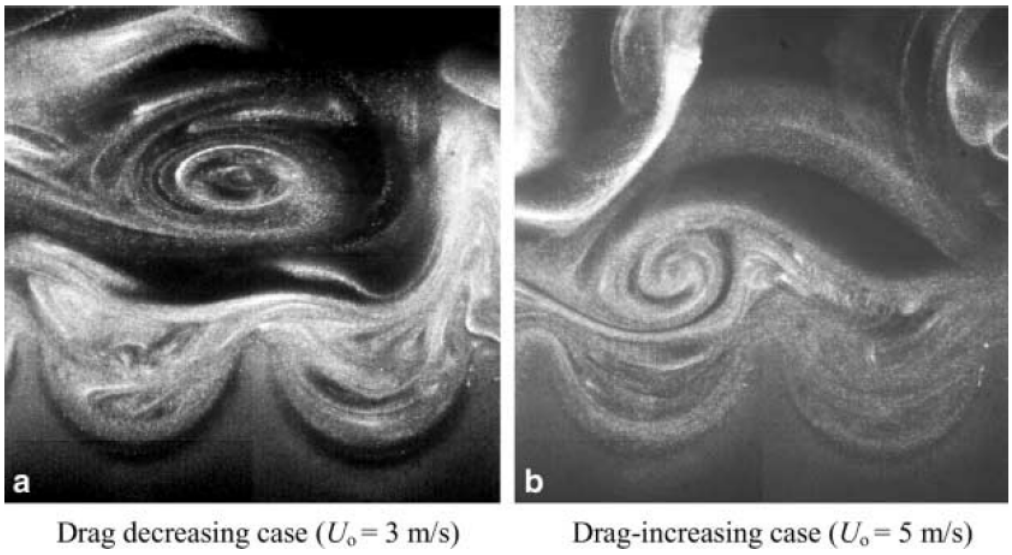

Figure 2.12: Flow visualization of riblet interaction with flow [Lee and Lee, 2001]

The second group argues that as the spacing and therefore the Karman number increases, the riblet spacing becomes larger than the scale of the vortices. One well cited work in favour of this view is from Lee and Lee [2001]. By visualizing the flow with smoke coherent structures near the riblets can be identified. Fig. 2.12 shows their results for drag decrease around s^+=25.2 and for the drag increase s^+=40.6. In the first case streamwise vortices are observed floating above the riblets while the flow inside the riblet valleys seems nearly undisturbed by the turbulent activity. As s^+ becomes larger however similar vortices can be seen inside the riblets valleys which are assumed to increase the skin friction and indeed shown by studies Garcia-Mayoral and Jimenez [2011].

2.2.4 Industrial and other application of riblets

Though riblets are known as a drag reducing tool, no commercial application has yet been made. This is explained in Bechert et al. [1997], Hage et al. [2001] and more recently Nugroho et al. [2013]. One universal problem so far is that riblets can only be optimalised for one velocity in the mean flow, which reduces their usefulness for systems with varying velocity. Secondly for practical reason, no system like ships or airplanes can be covered completely by riblets. The latter example was explained by Boomsma and Sotiropoulos [2015] where the Airbus construction was referenced. Another problem occurring during these tests was that, although a skin drag reduction of 3% was achieved, the riblets worn down too fast to be economical feasible.

Fortunately, riblets are not only investigated for their drag reducing properties. Strand and Goldstein [2011] discuss how riblets are able to constrain the growth of turbulence for low Reynolds number. This causes the boundary layer to remain laminar for higher Reynolds number reducing drag. Another use is proposed by Nugroho [2015], using riblets as vortex generators for example on aircraft wings. Finally Dean and Bhushan [2010] mention a modification to riblets based on shark-skin where mucus creates a hydrophobic surface between the wall and flow, which can be beneficial to certain chemical processes.

2.2.5 Riblets in turbulent boundary flow

Riblet research discussed so far has been for developed flow conditions. This is related to the current modeling of DC, where riblets perform optimal for a specific τ_{wall}. Because this value varies along the streamwise coordinate for the TBL, see eq. 2.4, riblets of fixed spacing can never be optimized around $s^+ = 17$.
Works that study riblets for TBL conditions work around this problem by measuring riblets only at downstream positions, where the change of τ_{wall} is small. Examples of these works are Walsh [1982], Pulles et al. [1989] and Nugroho et al. [2013]. The latter also mentions the importance of side wall effects, which can affect the flow and performance of riblets. All works show that similar results to Bechert et al. [1997] can be obtained and the varying of τ_{wall} is negible on DC.
A TBL property that can significantly affect DC is the presence of a pressure gradient. This happens once the displacement of fluid by the TBL starts to affect the flow. Boomsma and Sotiropoulos [2015] numerically investigated the effect of adverse pressure gradients on riblet performance. They found that for low gradient values, no significant effect was noticeable. For mild strength, they noticed an enhancement of riblet performance of O(2%).

2.3 Recent developments

This last section gives an overview of riblet research based on new interests. These mainly originate from the introduction of herringbone riblets, which are a bio-inspired of form of shark skin.

2.3.1 Bio-inspired and Herringbone riblets

Dean and Bhushan [2010] give an overview of riblets that are based on shark-skin textures that were already noted in the early 70's. Due to manufacturing difficulties however, these textures were not further investigated for some time. One of the earliest papers that studied riblets based on shark skin was the work by Koeltzsch et al. [2002]. In this work, turbulent pipe flow was studied in which riblets were placed in a converging-diverging herringbone formation, see figures 2.13 and 2.14. The results from this paper showed that above the converging riblets mean velocity decreases, while the turbulent streamwise intensity decreases. The reverse was observed for the diverging riblets.
Very recently, Nugroho [2015] produced his thesis in which he further investigates the research of Koeltzsch et al. [2002]. By means of hot-wire measurements and higher turbulent statistics he was able to confirm the Koeltzsch hypothesis, which states herringbone riblets generate large scale counter-rotating vortices.

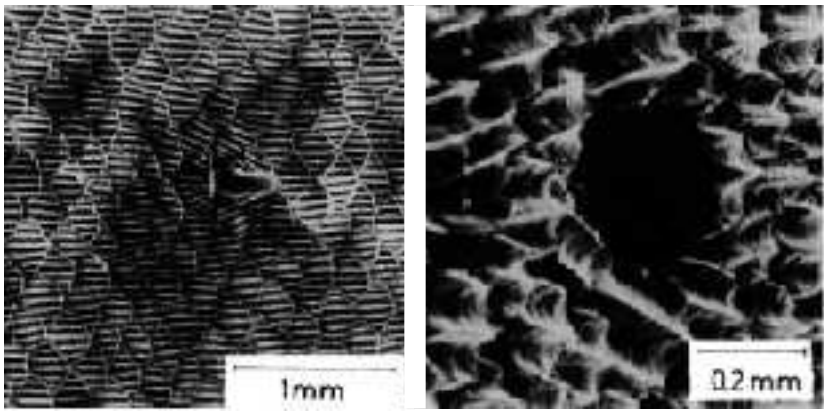

Figure 2.13: Left : Converging riblet patters[Koeltzsch et al., 2002]
Right: Diverging riblet patterns[Koeltzsch et al., 2002]

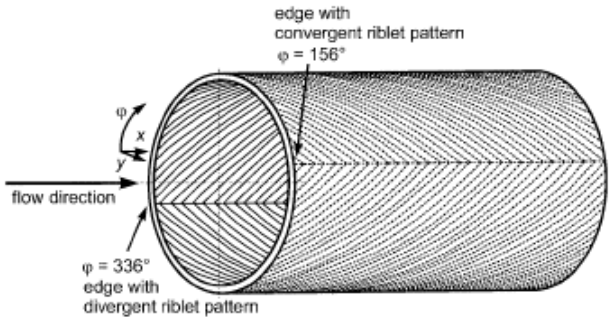

Figure 2.14: Test section from Koeltzsch et al. [2002]

The reason why herringbone riblets might be interesting for commercial use originate from the results by Chen et al. [2014]. By performing drag measurements for turbulent pipe flow, covered with bio-inspired herringbone riblets they obtain drag reductions of order 21 %, which is higher than found in Bechert's results. Sasamori et al. [2014] achieved 14 % drag reduction using sinusoidal varying riblets for turbulent pipe flow. They also reported similar flow behaviour to Koeltzsch et al. [2002] and Nugroho [2015].

2.3.2 FIK identity

A very important development in studying drag, and riblets in particular, is the derivation of the FIK identity by Fukagata et al. [2002]. By decomposing the drag into several components the contribution of various flow aspects can be studied and compared between different coatings. For a TBL with no pressure gradient it is given by:

$$C_f = \underbrace{\frac{4(1-\delta_d)}{Re_\delta}}_{\text{Laminar}} + \underbrace{2\int_0^1 2(1-y)(-\overline{u'v'})\mathrm{d}y}_{\text{turbulent}} \\ -2\int_0^1 (1-y)^2 \left(\underbrace{\overline{I_x}}_{\text{Inhomogeneous}} + \underbrace{\frac{\partial \overline{u}}{\partial t}}_{\text{Transient}} \right) \mathrm{d}y \tag{2.11}$$

where C_f is the skin friction which is a sum of a laminar, turbulent, inhomogeneity and transition contribution. Assuming homogeneity and steady flow, C_f is a sum of the first two terms, of which the turbulence is the largest.
This term also shows that not only the Reynolds shear stress $\overline{u'v'}$, but also its position with respect to the wall determines C_f. The most important insight from eq. 2.11 is that in order to reduce the drag by means of reducing the turbulence, the near wall region should be targeted. This corresponds well to qualitative comments that were made by Orlandi and Jimenez [1994], Kim [2011] and Garcia-Mayoral and Jimenez [2011] that riblets reduce drag by targeting the near wall flow, see sections 2.2.2 and 2.2.3.

Chapter 3

Setup Analysis

This chapter describes and analyses the cavitation tunnel. This experimental setup was used to evaluate the drag reducing properties of several coatings. To analyse and understand the quality of these measurements, the chapter comprises of two parts.

The first part gives a description of the setup, measuring sensors and their corresponding calibration. Next, the measuring routine is given, which was applied for all coatings. The first part ends with the data processing of the sensor signal output.

The second part analyses the error of the measurements, by decomposing it into a random, reading and systematical part. The first two are analysed with the propagation of uncertainty, which shows that the random error can be reduced such that only the reading error is significant. Also various systematical influences are analysed. The chapter concludes by evaluating the combined effect of all errors.

3.1 Experimental setup

The schematic representation of the cavitation tunnel located at Ship Hydromechanics group of the TU Delft is given in fig. 3.1. It was originally build as a closed loop to study cavitation on propellers and hydrofoils, see for more details Foeth [2008], Zverkhovskyi [2014] and Pennings [2016].

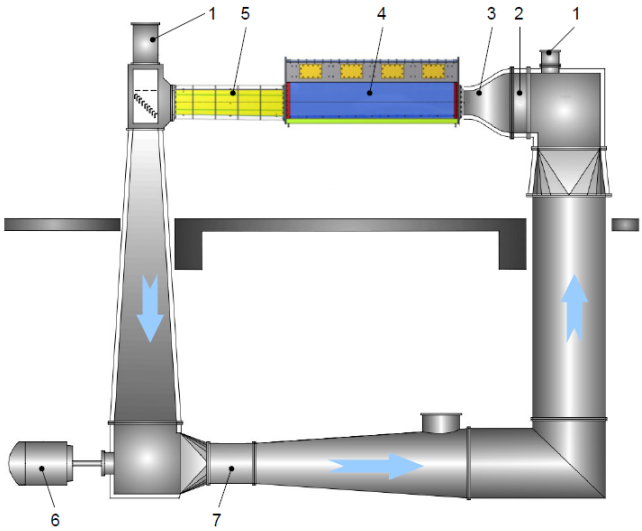

Figure 3.1: Schematics of the cavitation tunnel with main components: de-aeration tower (1), honeycomb (2), converger (3), test section (4), diffuser (5), electrical motor (6), propeller position (7). [Zverkhovskyi, 2014]

The flow inside the loop is driven by a propeller (7) operated by a frequency controlled electrical motor (6). Following the loop flow-wise, it passes through a honeycomb (2) and converger (3) to generate a uniform flow. The converger also houses a differential pressure sensor by which the velocity is recorded. From there the flow enters the test section (4) where the measurements take place. Finally the flow passes through a diffuser (5) and a second de-aeration tower (1) to close the loop. The water temperature is recorded by a PT-100 sensor in the second tower.

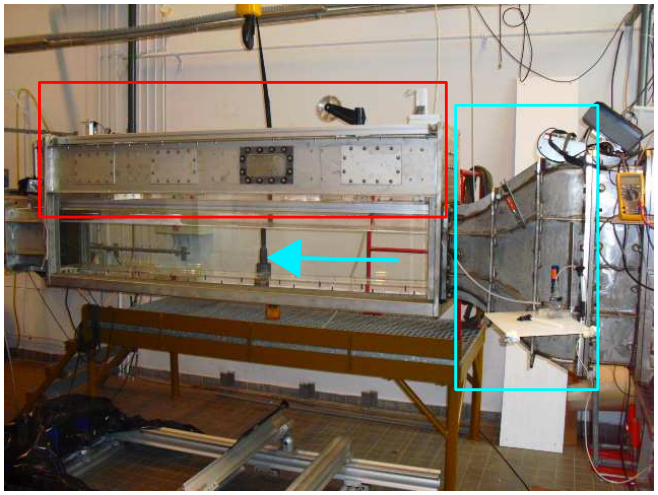

Figure 3.2: Test section in cavitation tunnel with location where drag force and velocity are measured

Fig. 3.2 shows the test section, which is 2 m long and has a cross section sized 300×30 mm^2 . The freestream velocity that can be generated in the section is up to 4 $\frac{m}{s}$. Beyond this velocity, air is entrained into the setup which has a deteriorating effect on both force and velocity measurements.

3.1.1 Drag force measurement

Fig. 3.3 shows the schematics of the drag force measurements. The coated plate (7), with dimensions 1998x298 mm^2, is attached to a moving frame (6). The drag force acting on the plate causes a displacement in the frame that is guided by brass leaf springs (2). The displacement of the moving frame is coupled to a load cell (1), which transforms the displacement into a force.
The load cell is calibrated with the calibration device (3). Allignment screws (8) allow precise positioning of the test plate, such that the angle of attack to the flow is within O(0.01°). A zigzag tripwire, with thickness 1.98 mm (9), at the entrance ensures the flow over the entire test plate is turbulent.

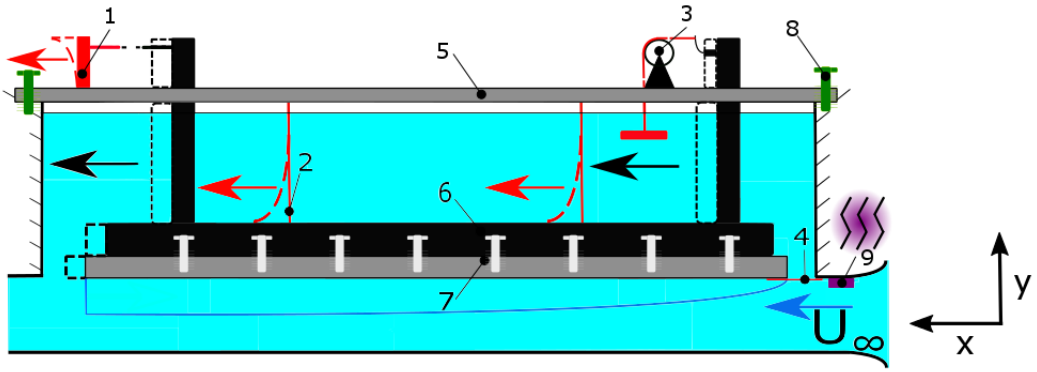

Figure 3.3: Schematics of drag force measurement with main components: force sensor (1), leaf spring (2), calibration device (3), entrance flow guide (4), fixed frame (5), moving frame (6), test plate (7), allignment screws (8) and trip wire (9)

To register the drag force, the plate must move freely and nowhere touch the fixed frame (5). Therefore small gaps are present between the plate and test section walls, see fig. 3.4. A flexible, thin plastic strip (4) is placed between the plate and the end of the converger to ensure the flow attaches to the plate.

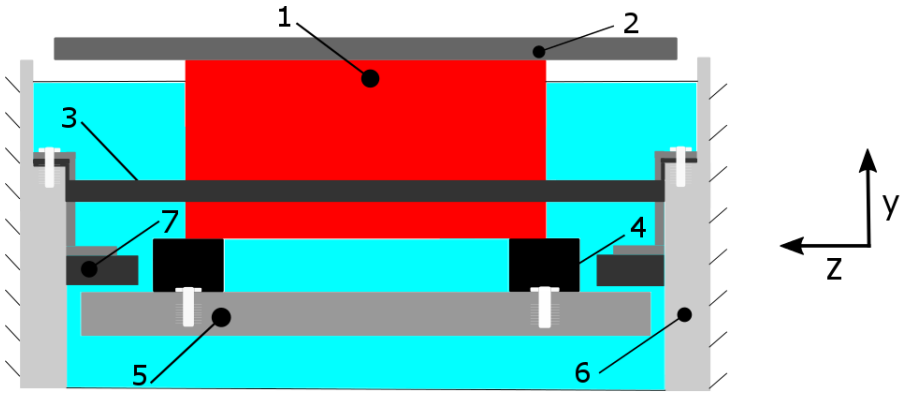

Figure 3.4: Schematics of setup cross section: leaf spring (1), fixed frame (2), wall holding beam (3), moving beam (4), test plate (5), setup walls (6), flow shields (7)

Fig. 3.4 shows the cross section of the setup, displaying the fixing of the moving frame by the leaf springs to the fixed frame. It also displays the wall holding beam (3), which was not drawn in fig. 3.3 for clarity. It was placed to arrest the expansion of the tunnel, caused by the hydrostatic water pressure, which unwantedly enlarged the gap between the test plate (5) and the fixed frame (6). To hamper flow through these gaps, flow shields (7) were installed.

3.1.2 Velocity measurement

Fig. 3.5 shows a close up of the contraction, which was also displayed in fig. 3.2. It shows the schematics of both the contraction and the pressure sensor. The latter is connected to the flow by two tubes which are respectively connected to the entrance and exit of the converger.
Assuming that friction inside the tubes and sensor is very small, Bernoulli can be used to convert both entrance and exit velocity into a static pressure:

$$P = \frac{1}{2}\rho U^2 \tag{3.1}$$

When a flow is present, the difference between entrance and exit pressure will deform the membrane inside the sensor, see fig. 3.5. Calibration prior to measurements ensures the motion is correctly transformed into the differential pressure over the contraction.

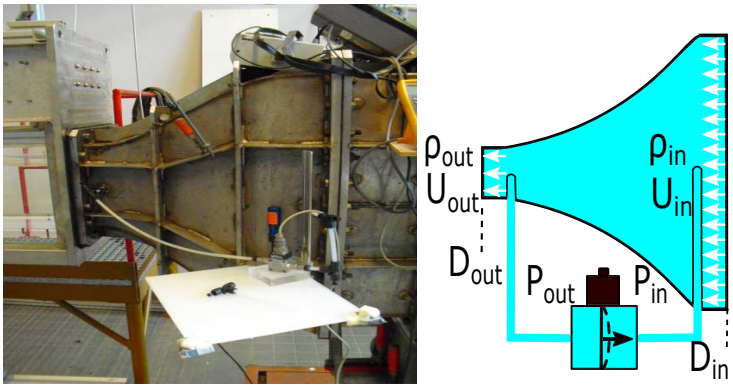

Figure 3.5: Left : Velocity measurement over contraction
Right: Schematics of pressure sensor

For subsonic flow conditions, the conservation of mass is given by:

$$\begin{aligned} \rho_{in} &= \rho_{out} \\ \Longrightarrow U_{in} D_{in}^2 &= U_{out} D_{out}^2 \end{aligned} \tag{3.2}$$

where ρ is the fluid density and D is the size of the square cross section. It shows that the velocity change is given by the ratio of areas. Assuming that Bernoulli also holds in the contraction, the velocity change is a function of the measured differential pressure:

$$\triangle P = \frac{1}{2}\rho \left(U_{out}^2 - U_{in}^2 \right) \tag{3.3}$$

Using eq. 3.2 to write U_{out} as function U_{in}, and inserting it into eq. 3.3 then yields the equation by which the pressure signal is transformed into the test section velocity:

$$\begin{aligned} \triangle P &= \frac{1}{2}\rho \left(U_{out}^2 - U_{out}^2 \left[\frac{D_{out}}{D_{in}} \right]^4 \right) \\ \Longrightarrow U_\infty = U_{out} &= \sqrt{\frac{2 \triangle P}{\rho \left(1 - \left[\frac{D_{out}}{D_{in}} \right]^4 \right)}} \end{aligned} \tag{3.4}$$

which is the velocity U_∞ that enters the test section. For the remainder of the thesis, this symbol will be used to describe the contraction speed.

3.1.3 Zig-zag strip

To ensure the flow is turbulent over the entire test plate, a zigzag strip is placed before the entrance of the test section. The designs of the strip dimensions and location, see fig. 3.3, are based on the work of Elsinga and Westerweel [2012].
Using estimations of upstream flow conditions a strip of thickness 1.98 mm was used. This strip was placed 10 cm before the test plate to minimize transition effects occurring over the test plate, although Elsinga and Westerweel [2012] mentioned these cannot be completely eliminated.

Figure 3.6: Left : Contraction with zigzag strips
Right: (up) Close up of zigzag strip (bt) photograph of zigzag strip

3.1.4 Temperature measurement

The temperature is recorded in the second de-aeration tower with a PT-100 class temperature sensor, see fig. 3.1. Prior to recording the entire loop is flushed for 2 minutes to mix out any temperature fluctuations. For more details on the PT-100 sensor, see its technical sheet Baumerprocess [2016] and the work of Foeth [2008].

3.2 Calibration

Calibration of both the load cell and the pressure sensor is required to obtain correct measurements. It also gives insight into the precision of the measuring sensors, which is essential for analysing the uncertainty. To compare with former calibrations, the procedure given by Zverkhovskyi [2014] will be used.

This procedure assumes a series of i measurements is repeated n times for a number of j applied loads to the sensor. One single measurement is then given by X_{ij}, which is the sensor output in Volts. The relative repeatability error for a specific load j, is then given by:

$$\begin{aligned} \epsilon_{rep} =& \frac{max\{X_{1j}, ..., X_{nj}\} - min\{X_{1j}, ..., X_{nj}\}}{\overline{X_j}} \\ \overline{X_j} =& \frac{\sum_{i=1}^{n} X_{ij}}{n} \end{aligned} \tag{3.5}$$

where the numerator substracts the minimum from the maximum sensor output for n instances the same load is measured. The denominator is the mean of all measurements for the same load. Multiplying ϵ_{rep} with the applied load gives the reading error:

$$\epsilon_{read} = \epsilon_{rep} Load \tag{3.6}$$

The mean sensor output which is given in Volts, has to be converted to the units of the physical load it represents. Both the load cell and pressure sensor are described by the manufacturer as linear response system, as motions for both sensors are very small.

This conversion is done by a Labview program for all sensors. The drag force signal is used directly, while the pressure signal is used to calculate the velocity at the contractions end by eq. 3.4. The temperature is used to determine the density and viscosity. Assuming linearity holds, the conversion is given by:

$$X_{pol} = aLoad + b \tag{3.7}$$

where X_{pol} is the linear polynomial which has the unit of the physical Load that is measured. It is determined by the slope $a[\frac{\text{Load}}{\text{V}}]$ and the offset b[V]. To see how well this linear polynom holds for the measured values the interpolation error is calculated:

$$\epsilon_{int} = \frac{\overline{X_j} - X_{pol}(X_j)}{X_{pol}(X_j)} \tag{3.8}$$

which quantifies how well X_{pol} is able to convert the voltage to the applied load.

3.2.1 Drag force

Fig. 3.7 gives the calibration procedure for the force sensor. It is removed from it's position in fig. 3.3 and directly loaded with known weights with mass 0.2, 0.5, 0.7, 0.9 kg. The latter one corresponds to 60% of the maximum drag force during the measurements, which was recommended by the technical sheet[TDB, 2006] of the force sensor. Table 3.1 gives the results from applying these weights:

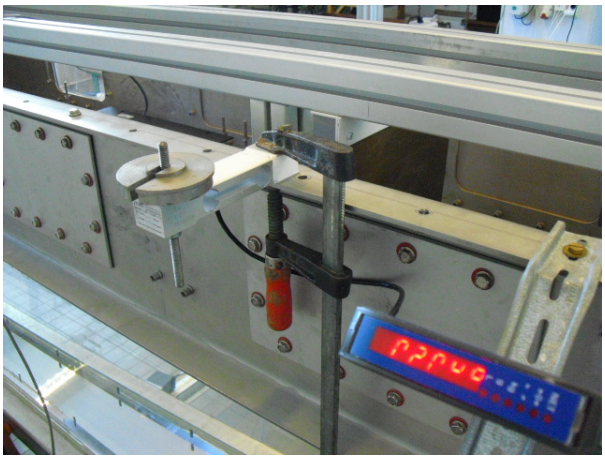

Figure 3.7: Calibration drag force

Table 3.1: Drag force calibration results

Load[N]	X_1[V]	X_2[V]	X_3[V]	X_4[V]
0.00	0.0371	0.027	0.0349	0.034
1.96	0.942	0.942	0.945	0.937
4.91	2.305	2.306	2.303	2.307
6.87	3.21	3.214	3.213	3.216
8.83	4.121	4.124	4.125	4.127

Applying equations 3.5 and 3.8 to this data gives the results of fig. 3.8. The left figure show the mean and polynomial voltage, including its coefficients. It shows that the response of the load cell is clearly linear.
This is also shown in the right figure where ϵ_{int} and ϵ_{rep} for the data of table 3.1 and Zverkhovskyi [2014] are displayed. Both show that the interpolation error is very small, meaning the conversion of the polynomial is accurate. Also the repeatability is very good, although for very low load values it tends to be slightly worse. This is expected behaviour, as these low values are not within the optimum measuring range of the load cell.

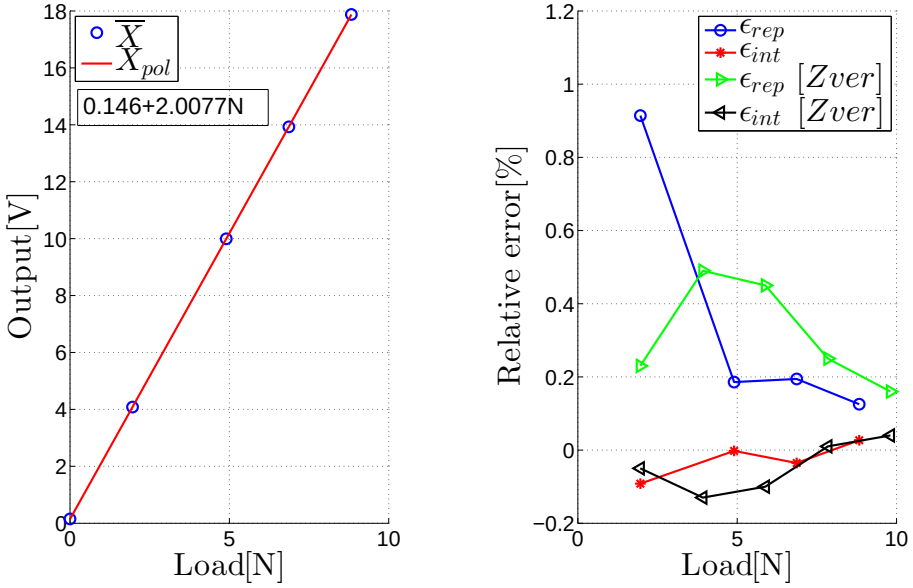

Figure 3.8: Left : $\overline{X}$ and X_{pol}
Right: Repeatibility and interpolation error

3.2.2 Pressure

The calibration of the pressure sensor is given in fig. 3.9, which displays the pressure sensor connected to a water column. In one tube, the water is held at reference height, while can be varied in the second. This difference in water height, $\triangle h$ causes a hydrostatic pressure difference which is given by:

$$P_{hy} = \rho \triangle hg \tag{3.9}$$

where g is the gravitation constant. With maximum velocity operating at U_∞= 4 $\frac{m}{s}$ the upper limit for $\triangle P$ is 8 kPa, using eq. 3.1. Table 3.2 shows the applied water column heights that correspond to the interval U_∞ 0-4 $\frac{\text{m}}{\text{s}}$ with steps of 0.5.

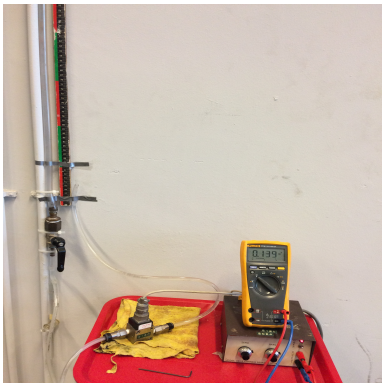

Figure 3.9: Calibration velocity

Table 3.2: Calibration results pressure

h[cm]	P_{hy}[kPa]	X_1[V]	X_2[V]	X_3[V]	X_4[V]
0	0.000	0.016	0.014	0.022	0.022
1.3	0.126	0.187	0.199	0.193	0.195
5.1	0.494	0.756	0.744	0.740	0.745
11.5	1.115	1.571	0.1584	1.570	1.579
20.4	1.978	2.755	2.759	2.749	2.747
31.9	3.093	4.173	4.204	4.182	4.187
45.9	4.449	5.900	5.890	5.890	5.910
62.4	6.049	7.840	7.850	7.860	7.870
81.5	7.901	10.000	10.030	10.030	10.010

Using the same procedure as for the load cell, fig. 3.10 shows the results for ϵ_{int} and ϵ_{rep}. Starting with ϵ_{rep}, a similar trend for the force sensor can be seen. Repeatability is very good for the interval except for the lower measuring range. No data of Zverkhovskyi [2014] is given, because he did not report the calibration for the pressure sensor.
In contrast to the load cell, ϵ_{int} is not negligible. This means that the polynomial is not perfect at converging the voltage to pressure. Consequences of this non-linear behaviour will be discussed in the error analysis section.

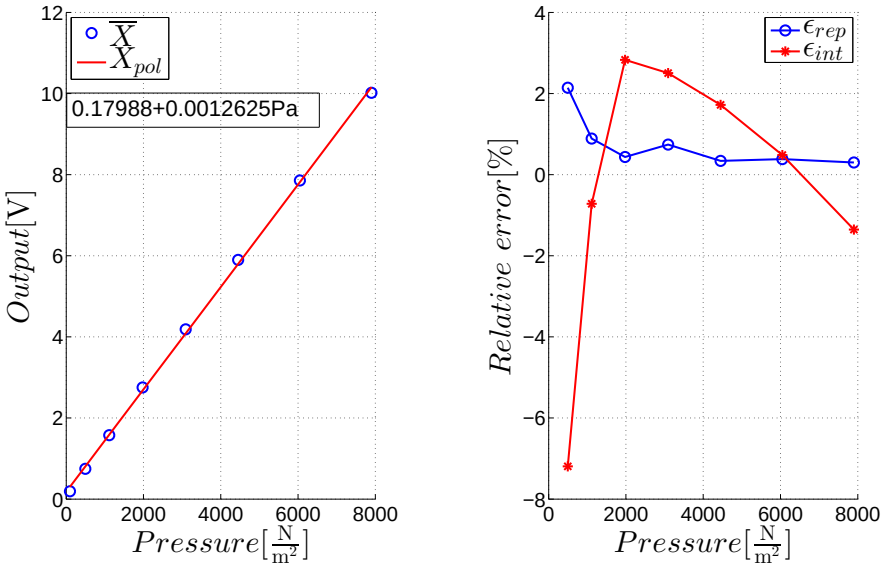

Figure 3.10: Left : $\overline{X}$ and X_{pol}
Right: Repeatability and interpolation error

3.3 Data acquisition

This section describes the measurement procedure which was used to measure the coatings. Tunnel operations are visually explained, displaying preparations prior to measuring. The signal recording for temperature, velocity and drag force is treated, including the general statistics to analyse these signals. The section concludes with introducing the key parameters that are used to quantify the drag performance of the coatings.

3.3.1 Measurement procedure

An overview of the procedure is given in fig. 3.11. Firstly, the various components described in fig. 3.3 have to be mounted to the plate(1). The entire constructed is the hoisted into the tunnel(2). After checking the plate can move freely, it is aligned to the flow by use of an analog and digital level(3). After placing the wall holding beams and flow shield the force sensor can be calibrated(4). The final step is the flushing of the setup to remove air from both plate(5) and flow loop. This also ensures the water temperature is uniform during measurements.

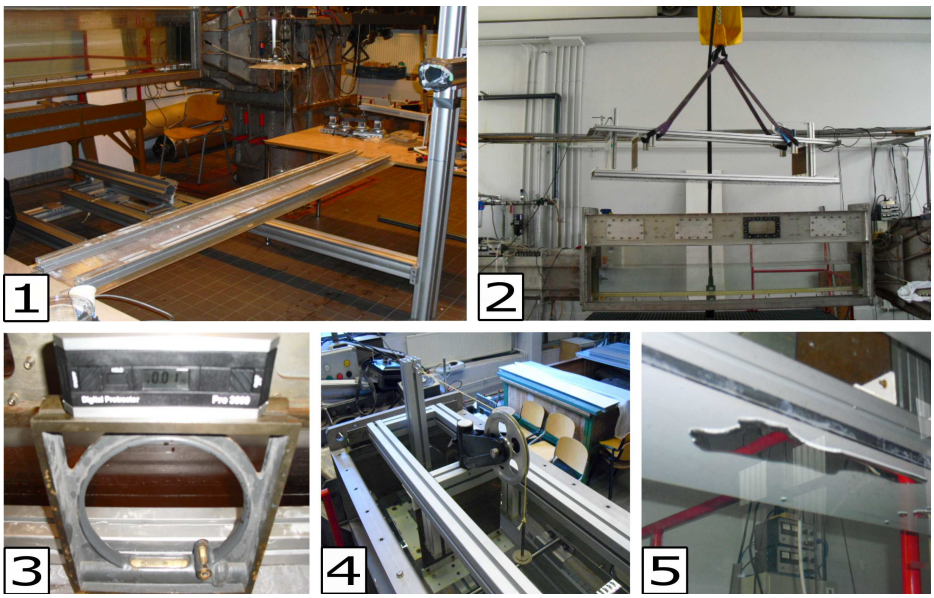

Figure 3.11: Measurement routine
1. Test plate before mounting 2. Placement in section by crane
3. Alignment to flow direction 4. Calibration of force sensor
5. Entrapped air on test plate, removed by flushing the tunnel

During measurements, the freestream velocity in the test section is set by the operator. An PD controller integrated with the recording LabVIEW system regulates U_∞. It registers the pressure value in the contraction and converts it to U_∞ by eq. 3.4. Simultaneously, it uses a feedback loop to control the pump power, ensuring the set velocity value remains within 2% bounds.

Independent measurements

After flushing the tunnel, independent measurements can be performed. This is done by starting at the lowest velocity of $U_\infty = 0.4\frac{\mathrm{m}}{\mathrm{s}}$ up to $4\frac{\mathrm{m}}{\mathrm{s}}$ with interval steps of $0.2\frac{\mathrm{m}}{\mathrm{s}}$. The pump and controller are then switched off, after which the water returns to quiescent state after 15 minutes. The calibration of the force sensor is then redone to remove any hysterisis, after which another cycle can be started.
The mounting is not redone between these cycles, implying the alignment remains constant. This was done because mounting is quite tedious and can take up well beyond an hour. The significance of keeping the mounting constant will be discussed in the reproducibility section, at the end of the chapter. Tests for different mountings prove alignment only affects the low velocities.

3.3.2 Signal recording

The LabVIEW program also registers the force, temperature and pressure signals. Fig. 3.12 shows samples of these signals for which the sampling frequency, f_{sample} is 1000 Hz. The signals are analysed by calculating the sample mean and variance[Lee and Wang, 2003], which are respectively given by:

$$\overline{X_s} = \frac{\sum_{i=1}^{n} X_i}{n} \tag{3.10}$$

$$\sigma^2_{X_s} = \frac{1}{1-n}\sum_{i=1}^{n}\left(X_i - \overline{X}\right)^2 \tag{3.11}$$

where X_i is a time series of measurements for n sampling points. Because f_{sample} is very large, this means both sample mean and variance are reliable estimates of the real mean and variance.

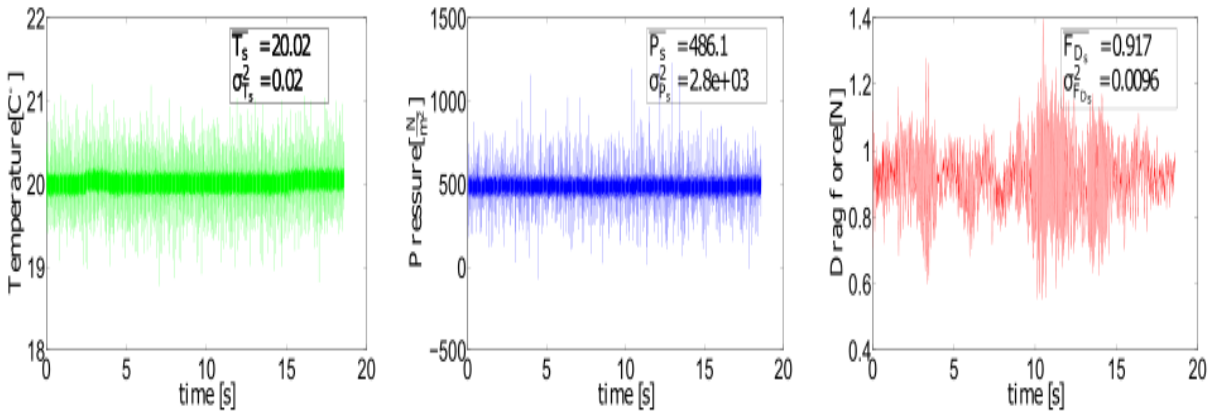

Figure 3.12: Signal samples of T,P and F_D

3.3.3 Data processing

The signals from fig. 3.12 are stored as data vectors by the LabVIEW program. Post measurements, they can be used to construct the Reynolds number and drag coefficient, given respectively by:

$$\overline{Re_L} = \frac{\overline{U_\infty} L}{\overline{\nu}} \tag{3.12}$$

$$\overline{C_D} = \frac{2\overline{F_D}}{\overline{\rho}\,\overline{U_\infty}^2 A} \tag{3.13}$$

where $\overline{U_\infty}$ is the contraction exit velocity, calculated by inserting $\overline{P}$ into eq. 3.4. $\overline{F_D}$ is the mean drag force on the whole plate. A is the plate surface, which is a product of its width W and length L. Finally $\overline{\rho}$ and $\overline{\mu}$ are the water density and kinematic viscosity respectively. For atmospheric conditions, ρ[Engineeringtoolbox] and μ[Al-Shemmeri, 2012] are both solely determined by temperature:

$$\overline{\rho} = \frac{\rho_0}{1 + \alpha(\overline{T} - T_0)} \tag{3.14}$$

$$\begin{aligned} \overline{\mu} =& C_1 \times 10^{\frac{C_2}{\overline{T}+C_3}} \\ & C_1 = 2.414 \times 10^{-5} \text{ [Pa.s]} \\ & C_2 = 247.8 \text{ [°C]} \\ & C_3 = 133 \quad \text{[°C]} \end{aligned} \tag{3.15}$$

Where ρ_0, α and T_0 are respectively the density, volumetric expansion coefficient and temperature at reference case. T is the measured temperature in degrees °C. The average temperature at which measurements where performed usually varied between $22 \leq T \leq 24$ °C. Thus the reference values where taken at 23 °C for which $\alpha = 0.000207 \ \frac{\mathrm{m}^3}{\mathrm{m}^3\mathrm{C}^\circ}$ and $\rho_0 = 998.2 \ \frac{\mathrm{kg}}{\mathrm{m}^3}$. The kinematic viscosity ν is then given by the ratio:

$$\overline{\nu} = \frac{\overline{\mu}}{\overline{\rho}} \tag{3.16}$$

The drag change can be constructed by dividing the drag coefficient of two different coatings:

$$DC = \frac{\overline{C_D^{coating}}}{\overline{C_D^{reference}}} - 1 \tag{3.17}$$

Where DC compares the C_D between a coating and a reference flat plate, at same Re_L. To compensate for slight variations in Re_L, due to temperature changes, this operation is applied to interpolated data. To include the riblet effect in the comparison this quantity is plotted against s^+, which is the non-dimensionalized form of the riblet spacing s.

$$s^+ = \frac{s\overline{u_\tau}}{\overline{\nu}} \tag{3.18}$$

Similar to the wall unit y^+ it rescales s by means of the viscosity ν and mean wall shear velocity $\overline{u_\tau}$, which is given by:

$$\overline{u_\tau} = \sqrt{\frac{\overline{\tau_{wall}}}{\overline{\rho}}} \tag{3.19}$$

Where τ_{wall} is the wall shear stress of the reference plate, which is determined on average by:

$$\overline{\tau_{wall}} = \frac{\overline{F_D}}{A} \tag{3.20}$$

Because the real wall shear stress varies along the streamwise direction of the plate, this average does not hold perfectly. It will underestimate u_τ at the plate leading edge and overestimate it the plate's end. Since T, F_D and P are always averaged from the measured signals, the overlines are dropped for the remainder of the thesis for clarity.

3.4 Error analysis

When performing experimental measurements, results are affected by errors. This section starts by decomposing the error into a random, reading and systematic part.
The random error is related to the natural variance and sample size, which were both discussed in the former section. The reading error is a property of the measuring sensors and can be obtained from the calibration in section 3.2. Assuming both are independent quantities, summation gives the measurements uncertainty. This quantity indicates how well independent measurements are repeatable. For sufficient measuring time, it reduces to the reading error.
Because C_D and DC are functions of multiple measured variables, the propagation of uncertainty is used. This method gives the contribution of every variable to the uncertainty of the drag coefficient and drag change.
The section continues with an investigation into the systematic error. This error is composed of several non-Gaussian influences from the system, which affect the results. The chapter concludes by analysing the reproducibility. This is most important, as this treats how well results in this thesis can be reproduced for slightly varying measuring conditions, which cannot be removed.

3.4.1 Error decomposition

When a variable f is measured, its value is bounded by a certain error[Taylor, 1997]:

$$\begin{aligned} f &\pm \epsilon^f \\ \left(\epsilon^f\right)^2 &= \left(\epsilon^f_{rep}\right)^2 + \left(\epsilon^f_{read}\right)^2 + \left(\epsilon^f_{sys}\right)^2 \end{aligned} \tag{3.21}$$

where ϵ^f is a sum of a repeatability, reading and systematical error. The repeatability error is a property of f, and caused by unknown and unpredictable 'random' changes. Assuming Gaussian behaviour, it can be computed by:

$$\begin{aligned} \epsilon^f_{rep} &= \frac{\sigma_f}{\sqrt{n_{ind}}} \\ n_{ind} &= \frac{t_m}{t_f} \end{aligned} \tag{3.22}$$

where σ_f is the standard deviation of f and n_{ind} is the number of independent measurements. It is defined as the ratio of the measuring time t_m, and the timescale of the variable f t_f.
The reading error is determined by measuring sensor and can be obtained from the calibration, see eq. 3.6. It represents the smallest change of f the sensor can accurately measure. When it is assumed to behave independent to ϵ_{rep}, both can be quadratically summed, which gives the uncertainty:

$$\mu_f^2 = \left(\epsilon^f_{rep}\right)^2 + \left(\epsilon^f_{read}\right)^2 \tag{3.23}$$

which is used to define the confidence interval, which encompasses 68% of all measurements. For large t_m, the denominator in eq. 3.22 causes ϵ^f_{rand} to become very small giving the limit case:

$$\lim_{t_m \to \infty} \mu_f = \epsilon^f_{read} \tag{3.24}$$

In contrast to ϵ_{rep} and ϵ_{read}, the systematic error is not a Gaussian behaving property. It represents the sum of systematic influences that distort the measurement. Examples are wrong calibration, unexpected flow phenomenae that disturb the TBL and resonance. The sources of these errors are generally hard to determine and to quantify, meaning correction is not always possible.

3.4.2 Propagation of uncertainty

Since expected DC is O(5%), the uncertainty must lie within 1% bounds. To achieve this, the propagation of error is used to make an a priori estimate of the uncertainty of both C_D and DC, which is given by [Lee and Wang, 2003]:

$$\mu_f^2 = \sum_{i=1}^{n} \left(\frac{\partial f}{\partial x_i} \right)^2 \mu_{x_i}^2 + 2 \sum_{i=1}^{n} \sum_{j \neq i}^{n} \frac{\partial f}{\partial x_i} \frac{\partial f}{\partial x_j} \rho_{ij} \mu_{x_i} \mu_{x_j} \tag{3.25}$$

Where $f(x_i)$ is a function of several variables, and μ_f and μ_x are the uncertainties of f and it's variables respectively. ρ_{ij} is the Pearson correlation coefficient given by:

$$\rho_{ij} = \frac{\sigma_{x_i x_j}}{\sigma_{x_i} \sigma_{x_j}} \tag{3.26}$$

where $\sigma_{x_i x_j}$ is the covariance between the variables x_i and x_j. Writing the these variables as vectors x and y for clarity gives their covariance by:

$$\sigma_{xy} = \frac{1}{n-1} \sum_{i=1}^{n} (x_i - \overline{x})(y_i - \overline{y}) \tag{3.27}$$

This approach includes both the uncertainty of the variables and the correlation between the variables. Analysis of the signals showed that only a significant correlation exists between U_∞ and F_D, see next subsection. When applying eq. 3.25 to equations 3.13 and 3.17, this yields:

$$\begin{aligned} \mu_{C_D}^2 = &\left(\frac{2}{\rho U_\infty^2 A} \right)^2 \mu_{F_D}^2 + \left(\frac{2F_D}{U_\infty^2 A} \right)^2 \left[\frac{-1}{\rho^2} \right]^2 \mu_\rho^2 + \left(\frac{2F_D}{\rho A} \right)^2 \left[\frac{-2}{U_\infty^3} \right]^2 \mu_{U_\infty}^2 \\ &+ \left(\frac{2F_D}{\rho U_\infty^2} \right)^2 \left[\frac{-1}{A^2} \right]^2 \mu_A^2 + \left(\frac{2}{\rho U_\infty^2 A} \right) \left(\frac{-4F_D}{\rho U_\infty^3 A} \right) \rho_{FDU_\infty} \mu_{F_D} \mu_{U_\infty} \end{aligned} \tag{3.28}$$

$$\mu_{DC}^2 = \left(\frac{1}{C_D^{reference}} \right)^2 \mu_{C_D^{coating}}^2 + \left(- \frac{C_D^{coating}}{\left(C_D^{reference} \right)^2} \right)^2 \mu_{C_D^{reference}}^2 \tag{3.29}$$

Note that the effect of the U_∞ is amplified by a factor 2, due to it's quadratic relation with C_D. All contributions are positive, with exception of the correlation term. This implies the correlation either enlarges or reduces the total uncertainty, depending on its sign.

3.4.3 Uncertainty analysis

To calculate μ_{C_D} and μ_{DC} analysis for the entire measuring interval $0.4 \leq U_\infty \leq 4 \ \frac{\mathrm{m}}{\mathrm{s}}$ representative signals are required. Therefore 5 independent measurement cycles, as described in section 3.3.1, were performed. Using equations 3.11 and 3.27, the standard deviation and Pierson correlation coefficient are computed for every measurement. Averaging these gives the result in fig. 3.13. Knowing f_s is 1000 Hz, it is assumed this data gives a good representation of the setup variance.
Starting left, it can be seen that the variance for the temperature remains constant as expected, since temperature changes are negligible and fluid motion around the sensor is minimal. Both F_D and U_∞ show an increase in variance for increasing velocity, which is a result of the PD controller that tries to keep U_∞ between 2% bounds.
A peak of high variance can be seen around $U_\infty = 2.8 \frac{\mathrm{m}}{\mathrm{s}}$, which is caused by resonance in the entire test section. This resonance can be audible identified as a 'tingling' sound that increases in frequency as the velocity increases.
The right hand plot of fig.3.13 shows the correlation coefficients between the T, F_D and U_∞ signals. As expected, temperature displays no significant correlation with the other variables for reasons just explained. The correlation between velocity and drag force is significant and will be discussed in detail further on.

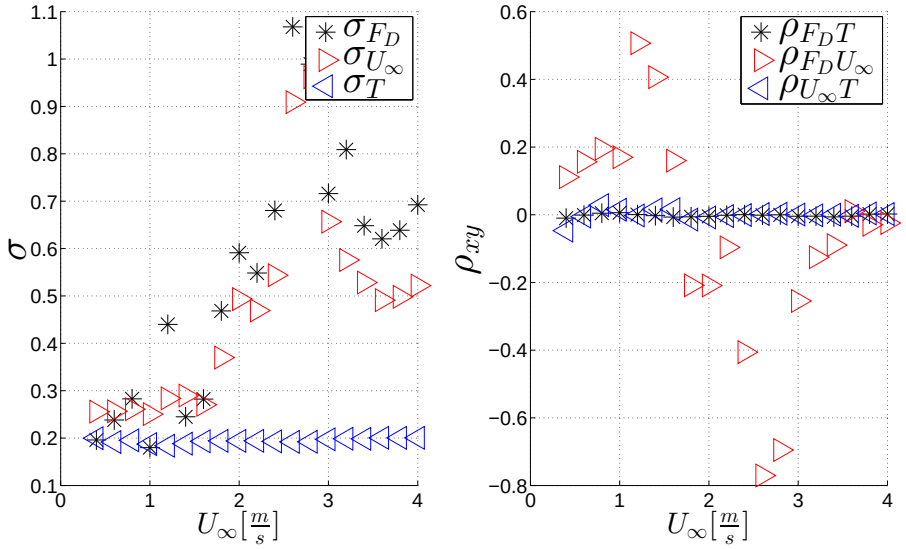

Figure 3.13: Left : Sample standard deviations for F_D, T and U_∞
Right: Pearson correlation coefficient between F_D, T and U_∞

Surface area

Starting with the geometry, it is known that A is the product of the length L and width W of the plate. Both are measured with a measuring tape which has uncertainty 0.5 mm. Using eq. 3.25 then yields:

$$\mu_A = \sqrt{B^2\mu_L^2 + L^2\mu_B^2} = 1 \text{ mm}^2 \tag{3.30}$$

Temperature

In contrast to the surface area, the water temperature is not a constant property, see fig. 3.12. Starting with properties of the recording PT-100 sensor, ϵ_{read}^t is given by its technical sheet[Baumerprocess, 2016]:

$$\epsilon_{read}^T(^\circ C) = 0,15 + 0,002|T| \tag{3.31}$$

As operating temperatures are within $22 \leq T \leq 24$ °C the temperature has a slight influence on ϵ_{read}^T.

Although the sensor is not directly placed inside the flow loop, it is still slightly affected by the freestream magnitude which can be seen in fig. 3.14. This is most likely caused by the small fluid motion around the sensor.
To compute μ_T by eq. 3.22, the number of independent measurements must be obtained. Consulting the technical sheet gives that the timescale, t_T of the PT-100 sensor is 8 s. This represents the diffusion time of the sensor. n_{ind} can then be computed by:

$$n_{ind} = \frac{t_m}{t_T} \tag{3.32}$$

Fig. 3.14 displays the uncertainty of the temperature for various measuring times. It can be seen that once $t_m \geq 2$ min, μ_T becomes of order ϵ_{read}^T. This means that measuring beyond this time does no longer decrease μ_T. It can therefore be concluded that for $t_m \geq 2$ min, the temperature uncertainty is determined by the PT-100 sensor reading error which is O(0.15°C).

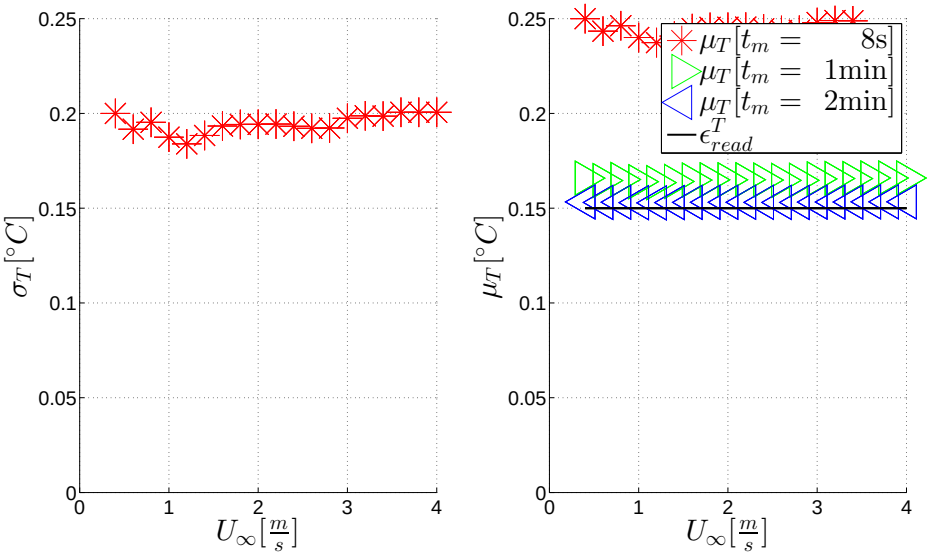

Figure 3.14: Left : Standard deviation of T
Right: Uncertainty of T for several t_m

Using this result, the uncertainties for both ρ and ν can be determined by applying eq. 3.25 to equations 3.14 and 3.15 yielding:

$$\begin{aligned} \mu_\rho^2 &= \left(\frac{-\alpha\rho_0}{1+(T-T_0)^2} \right)^2 \mu_T^2 \\ \mu_\mu^2 &= \left(\frac{-C_1 C_2 log(10) 10^{\frac{B}{T-C_3}}}{(T-C_3)^2} \right)^2 \mu_T^2 \end{aligned} \tag{3.33}$$

which gives for T=23 $°C$, μ_{rho}=0.03 $\frac{\text{kg}}{\text{m}^3}$ and μ_μ=3.3×10^{-6} $\frac{\text{m}^2}{\text{s}}$, which corresponds to a O(0.003%) and O(0.3%) uncertainty respectively. This means the μ_ν is of similar order to μ_μ, namely O(0.3%), which is within the desired 1% uncertainty bound.

Drag force

The reading error of the load cell is given by it's ability to reproduce static loads, which was treated in the calibration section. In contrast to the temperature sensor, θ_{F_D} it is determined by the applied force:

$$\epsilon_{read}^{F_D} = \epsilon_{rep} F_D \tag{3.34}$$

where F_D is taken from the data used to construct fig. 3.13, which varies between $0.5 \leq F_D \leq 16$ N.

Fig. 3.17 shows σ_{F_D}, which is the variance of the force signal. It can be seen that it increases with the freestream magnitude, which means the drag measurement is sensitive to fluid motions. Especially around 3 $\frac{\text{m}}{\text{s}}$ large variance can be observed, which is caused by resonance in the leaf-spring system.
To obtain n_{ind} and therefore the μ_{F_D} the timescale of the force signal is estimated by modelling the measurement in fig. 3.3 as a linear mass-spring system. This is valid as both test plate and leaf springs are subject to very small motions. The model is then given by:

$$\begin{aligned} \delta = \frac{2F_D l^3}{3EI} = 2kF_D \qquad &, where\ k = \frac{l^3}{3EI} \\ &and\ I = \frac{wt^3}{12} \end{aligned} \tag{3.35}$$

Here δ is the test plate displacement.l is the length, E the Young modulus and I the second area moment of the leafspring, based on its thickness, t and width w. Note the factor $2k$, because of the parallel leaf springs. Neglecting water friction, the dynamic model is given by:

$$m\ddot{\delta} + 2k\delta = F_D \tag{3.36}$$

Where m is the systems mass and ω is the system's impedance. t_{F_D} can be computed by taking its inverse:

$$\omega = \sqrt{\frac{8h^3}{mEwt^3}} \Longrightarrow t_{F_D} = \sqrt{\frac{mEwt^3}{8h^3}} \tag{3.37}$$

This leaves only the mass to be determined. Observing the test plate's dimensions and properties from fig. 3.15, m is the sum of described in table 3.3 equalling 37.1 kg. Inserting this into eq. 3.37, with E for brass being 100 MPa yields:

$$\omega \approx 0.16\text{Hz} \Longrightarrow t_{F_D} \approx 6.4\text{s} \tag{3.38}$$

Table 3.3: Test section components and corresponding mass

Nr	Component	Amount	l×w×t[mm]	Density $[\frac{\text{kg}}{\text{m}^3}]$	Mass [Kg]
1	Plexiglass plate	1	1998×298×10	1190	7.09
2	Aluminium horizontal beams	2	1998×40×40	2700	17.3
3	Brass leafsprings	2	30×30×2	8500	0.03
4	Steel plates	2	260×260×10	7500	10.1
5	Aluminium vertical beams	2	300×40×40	2700	2.6

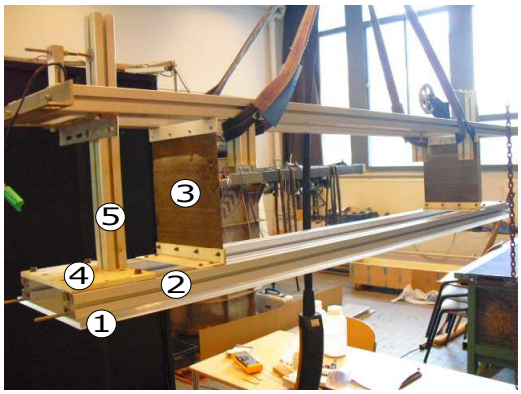

Figure 3.15: Test section

To validate these calculations a spectral analysis is made of the force sensor's response at $U_\infty = 0.4$ and 4 $\frac{\text{m}}{\text{s}}$. Computing the autocorrelation[ACF] of F_D over 30 seconds displays a clear sinusoidal response in fig. 3.16. Applying Wiener-Khinchin theorem[Papoulis, 1977] the power spectral density[PSD] can be computed to find the characteristic frequencies.
For both velocities the first significant frequency is originated around 0.3 Hz, which corresponds to the lowest varying oscillation in the ACF. Comparing it to the theoretical value in eq. 3.38 shows that both values are of the same order.

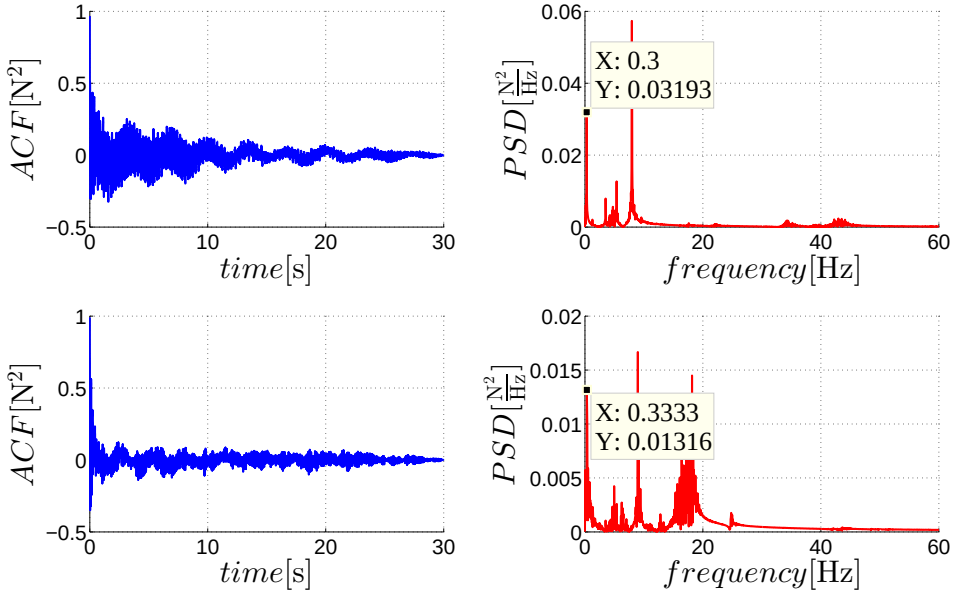

Figure 3.16: Up : ACF and PSD for U=0.4 $\frac{\text{m}}{\text{s}}$
Down: ACF and PSD for U=4.0 $\frac{\text{m}}{\text{s}}$

Using the theoretical t_{F_D} as a conservative estimate, μ_{F_D} can be obtained using eq. 3.22. When constant measuring times are used this gives the result in fig. 3.17. It can be seen that for $t_m \geq 30$ min, the uncertainty is reduced to tolerance level, except for the resonance region.
Although this seems to suggest long measurements are necessary at high velocities to obtain good accuracy; next section will show good repeatibility can be obtained for much lower t_m.

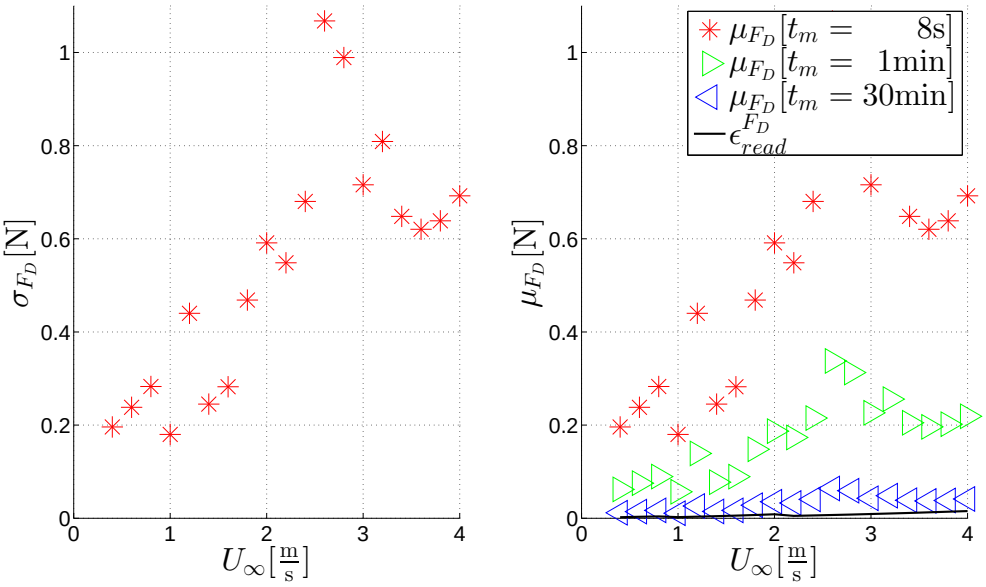

Figure 3.17: Left : Standard deviation of F_D
Right: Uncertainty of F_D for several t_m

Velocity

Similar to the load cell, the reading error of the pressure sensor is given by:

$$\epsilon_{read}^{U_\infty} = \epsilon_{rep} U_\infty \tag{3.39}$$

Because the pressure is measured and subsequently converted, eq. 3.39 can be rewritten by inserting the pressure-to-Velocity calculation eq. 3.4, yielding:

$$\epsilon_{read}^{U_\infty} = \sqrt{\frac{2\epsilon_{rep} P}{\rho\left(1 - \left[\frac{D_{out}}{D_{in}}\right]^4\right)}} \tag{3.40}$$

Since the pressure sensor is located in the contraction, it is subject to the flow timescales present there. These differ from the flow in the test section, which means the spectral analysis of the P signal cannot be used to determine t_{U_∞}. Instead an outer flow timescale, based on the mean advection is defined:

$$t_{U_\infty} = \frac{L}{U_\infty} \tag{3.41}$$

Which represents the time to refresh the freestream flow over the test plate. A direct consequence of this approach is that measuring at lower velocities takes longer to obtain the same n_{ind}.

Fig. 3.18 shows the variance and tolerance for the pressure sensor. The right plot shows the converted data, which for the uncertainty is given by:

$$\mu_{U_\infty}^2 = \left[\frac{1}{\rho\left(1 - \left[\frac{D_{out}}{D_{in}}\right]^4\right)}\right]^2 \mu_P^2 \tag{3.42}$$

Because $\epsilon_{read}^{U_\infty}$ depends on both U_∞ and μ_{U_∞}, the shape of the uncertainty curves is different between the two plots. Both figures show that for $t_m \geq$30 min the uncertainty of both, P and U_∞ approaches $\epsilon_{read}^{U_\infty}$. Similar to F_D, next section will explain why such long measuring times are not required to obtain accurate measurements.

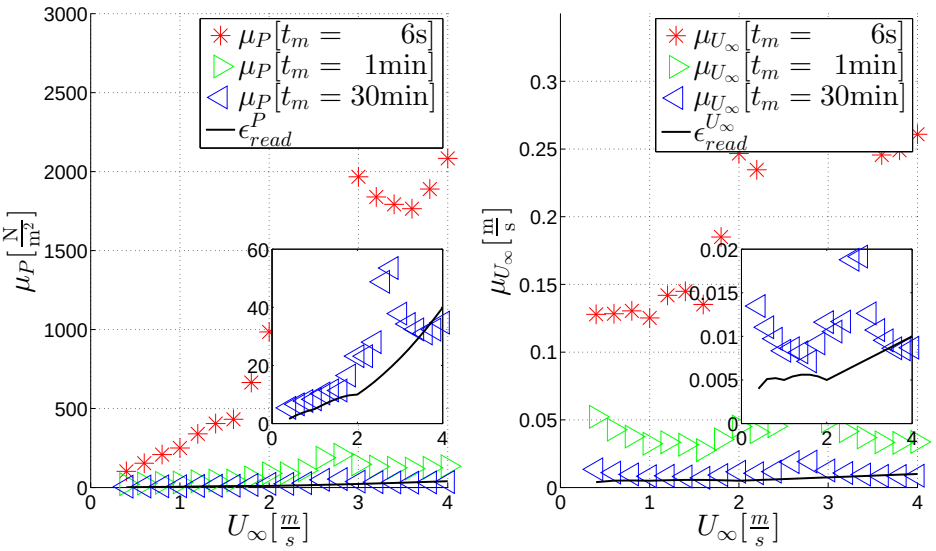

Figure 3.18: Left : Uncertainty of P for several t_m
Right: Uncertainty of U_∞ for several t_m

Correlation

The monotonous relation between U_∞ and F_D, given in eq. 2.4 suggests:

$$\rho_{F_D U_\infty} = 1 \tag{3.43}$$

for the entire velocity regime. This behaviour is not seen in the right plot of fig. 3.13. Although a significant correlation exists between F_D and U_∞, it is much smaller than the theoretic value from eq. 3.43.
The different timescales for the drag force and freestream velocity are suspected to cause this weaker correlation. Due to this difference, the response of the force to velocity changes is not simultaneous. As a result, the correlation is smaller and for some velocities even out of phase, as displayed by the negative value.

3.4.4 Measurement time and confidence intervals

With all terms in eq. 3.28 known, μ_{C_D} can be constructed. Fig. 3.19 shows the uncertainty intervals for t_m of 2 min for every measuring point. The C_D curve is from the theory introduced in the literature:

$$C_D = \frac{0.031}{Re_L^{\frac{1}{7}}} \tag{2.7}$$

The left fig. also shows the uncertainty bars for infinite t_m, which means that the uncertainty equals $\epsilon_{read}^{C_D}$. This fig. also shows the $\frac{\mu_{C_D}}{C_D} = 1\%$ intervals to give an indication of the interval size.
A decreasing trend of μ_{C_D} for increasing Re_L can be observed. This is consistent with $\epsilon_{read}^{F_D}$ and $\epsilon_{read}^{U_\infty}$ results, which showed higher values for low U_∞, which can also be seen in the right hand fig. This fig. also shows the resonance region for $U_\infty = 2.8\frac{\mathrm{m}}{\mathrm{s}}$ or $Re_L = 5.6 \times 10^6$.
The right fig. shows the decomposition of the uncertainty according to eq. 3.28 for t_m equals 2 min. The contributions of μ_T and μ_A are insignificant compared to the velocity and drag force. The correlation has a slight effect, reducing μ_{C_D} for low velocities and increasing it for high values.

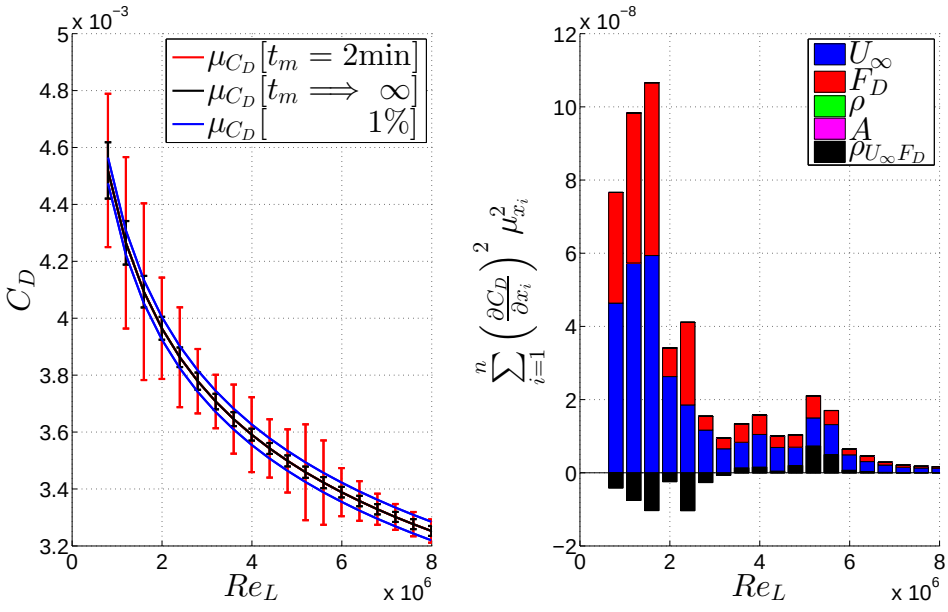

Figure 3.19: Left : μ_{C_D} for t_m=2 min and unlimited measuring time
Right: contribution of individual terms to $\mu_{C_D}^2$ for t_m=2 min

The main conclusion to be drawn from fig. 3.19 is that longer measuring times are needed to reduce the measuring uncertainty. To compute t_m needed to reduce μ_{C_D} to 1% or the $\epsilon_{read}^{C_D}$ limit, eq. 3.28 is rewritten into relative form by dividing every term by C_D^2:

$$\left(\frac{\mu_{C_D}}{C_D}\right)^2 = \left(\frac{\mu_{F_D}}{F_D}\right)^2 + \left(\frac{\mu_\rho}{\rho}\right)^2 + \left(\frac{2\mu_{U_\infty}}{U_\infty}\right)^2 + \left(\frac{\mu_A}{A}\right)^2 - \frac{\mu_{F_D}}{F_D}\frac{2\mu_{U_\infty}}{U_\infty}\rho_{F_D U_\infty} \tag{3.44}$$

By moving the approximately constant contributions of ρ and A to the left side and applying eq. 3.22, the following function for t_m can be defined:

$$\begin{aligned}\left(\frac{\mu_{C_D}}{C_D}\right)^2 - \left(\frac{\mu_\rho}{\rho}\right)^2 - \left(\frac{\mu_A}{A}\right)^2 = \frac{1}{t_m}\Bigg[&\left(\frac{\sigma_{F_D} t_{F_D}^{\frac{1}{2}}}{F_D}\right)^2 + \left(\frac{2\sigma_{U_\infty} t_{U_\infty}^{\frac{1}{2}}}{U_\infty}\right)^2 \\ &- \left(\frac{\sigma_{F_D} t_{F_D}^{\frac{1}{2}}}{F_D}\right)\left(\frac{2\sigma_{U_\infty} t_{U_\infty}^{\frac{1}{2}}}{U_\infty}\right)\rho_{F_D U_\infty}\Bigg]\end{aligned} \tag{3.45}$$

which is closed by defining the ratio of μ_{C_D} over C_D. Fig. 3.20 shows the solution of eq. 3.45 for the instance the uncertainty reduces to the reading error. It also shows the t_m required for the uncertainty to collapse on the 1% curves in fig. 3.19.
Comparing these two curves it can be seen that for $U_\infty \geq 1\frac{\text{m}}{\text{s}}$ the reading error curve becomes smaller than the 1% curve. This means that for low velocities, uncertainties valued $\frac{u_{C_D}}{C_D} = 1\%$ cannot be obtained. The is caused by the ϵ_{rep} behaviour for F_D and P, explained in section 3.2.

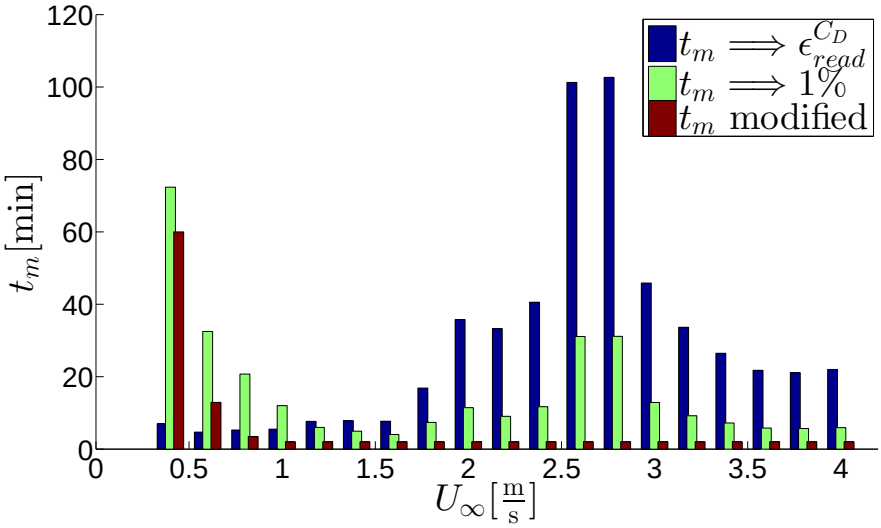

Figure 3.20: Measuring time required to reach $\epsilon_{read}^{C_D}$ or 1% uncertainty. The modified timescale is the used t_m for the remainder of the chapter

Assuming 1% intervals of μ_{C_D} can be reached, fig. 3.20 shows that large t_m are required. This behaviour can also been seen around $U_\infty = 2.8\frac{\text{m}}{\text{s}}$, which corresponds to the resonance region. Because this region was included in the analysis, high values of t_m seem necessary. Next section will however show this resonance does not affect the behaviour of C_D and much smaller t_m result in the required uncertainty. This time is also displayed in fig. 3.20 by t_m modified. Next subsection will analyse the practical implication of using this timescale.

Application of the uncertainty analysis

The result from fig. 3.20 gives an indication how long the measurement time should be to obtain accurate measurements. To validate the analysis, 4 independent series of measurements were performed for the analysed interval of U_∞. Because running the pump for high velocities can overload the system, a modified t_m was used, see fig. 3.20.
This t_m is based on the 1% curve with smaller magnitude, especially at the resonance region. This is based on the assumption the resonance does not affect the measuring time, which will be proven to hold. For $U_\infty \leq 1 \frac{\mathrm{m}}{\mathrm{s}}$ the large difference between the 1% and $\epsilon_{read}^{C_D}$ curve is caused by the limitations of the F_D and P sensors. To ensure μ_{C_D} is obtained, the modified t_m is chosen larger than required by $\epsilon_{read}^{C_D}$.

Fig. 3.21 shows the results for the 4 independent measurements. The left plot displays the raw data points for the 4 series. The right plot shows the mean of the interpolated data and the uncertainty according to eq. 3.23.

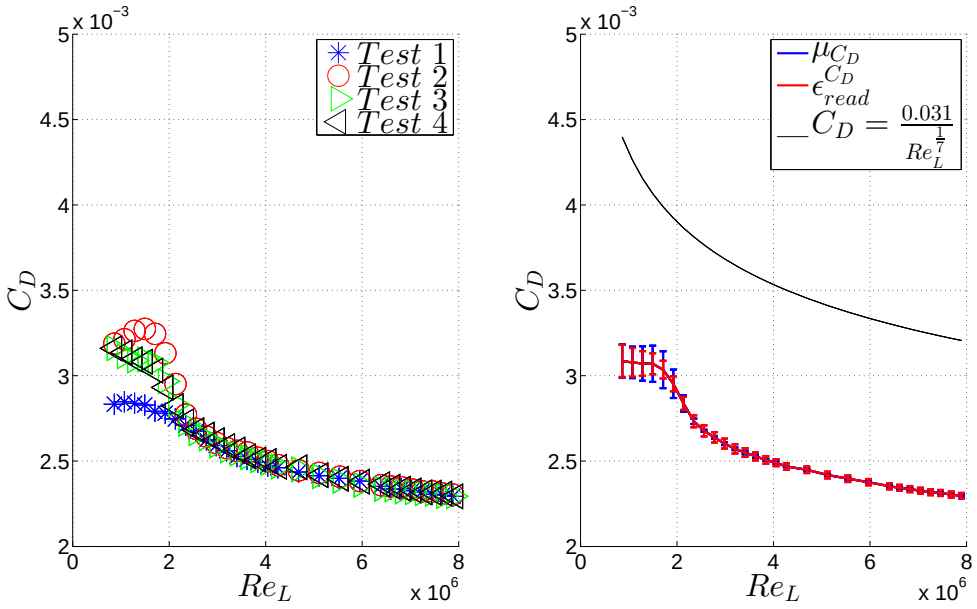

Figure 3.21: Left : C_D for the 4 measurements
Right: $\overline{C_D}$, μ_{C_D} compared to theory

Both plots display good repeatability for the interval $Re_L \geq 2 \times 10^6$. For this regime, μ_{C_D} is also of comparable order of $\epsilon_{read}^{C_D}$. It can be concluded that using t_m=2 min produces good repeatable data. The overestimation of t_m in fig. 3.20 is caused by resonance, especially at $Re_L = 5.6 \times 10^6$.
For the lower regime the analysis seems to hold less well. The large spread in the data from the left plot causes the drag curve to flatten. This behaviour does not compare to the theoretical curve and indicates the measurements are affected by systematic influences. Another indication that systematic biases are present is the large difference in magnitude with the theoretical curve. This will be analysed in the next section.

3.4.5 Systematic bias

Fig. 3.21 showed that the measurements are affected by systematic effects. This section qualitatively analyses several systematic sources by measuring them separately. This gives insight into the significance of the bias effect. The sections main conclusion is to explain the theoretical TBL flow from literature cannot be realised in the setup.
First the freestream velocity is analysed with Pitot tubes. Next, corner flow effects due to the gaps and the wall are measured with flow shields and a flush-mounted plate respectively. The section ends with analysing the bias of the leaf-spring system, which registers the plate motion.

Velocity error

The significance of the interpolation error of the pressure sensor displayed its liability to systematic errors. Furthermore the velocity calculation by means of Bernoulli in eq. 3.3 does not include friction and fluid displacement effects in the contraction. To obtain an independent reference for U_∞, Pitot tube measurements were proposed.
Fig. 3.22 displays the used pitot tubes and measuring positions. The mean flow, entering the perpendicular placed tube hole, stagnates to a pressure build up. This build up pressure can be converted to the measured freesteam velocity by eq. 3.1.

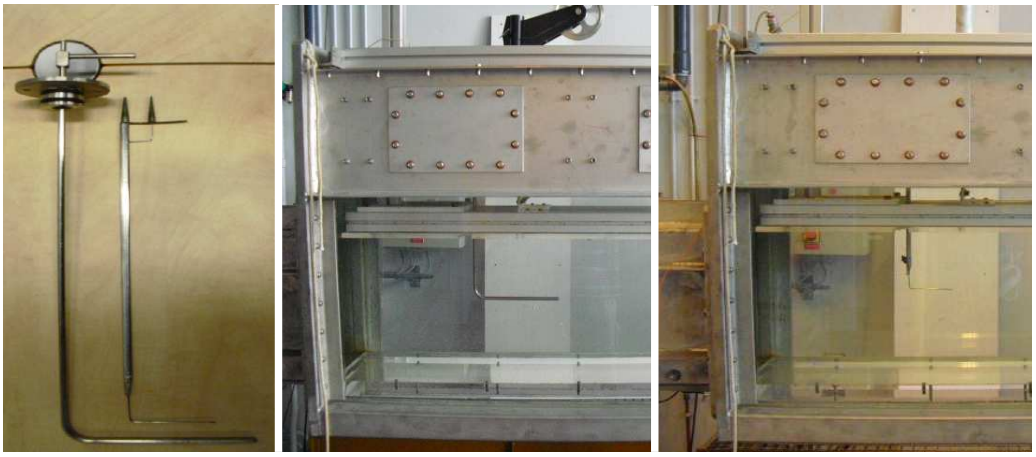

Figure 3.22: Left : Used Pitot tubes
Middle: Large Pitot tube measuring U_∞
Right : Small Pitot tube measuring U_∞

Unfortunately, both tubes gave results of different magnitude, which can be found in Appendix A. Both tubes however, displayed a trend that the velocity calculated at the converger overestimates the real velocity in the test section. Based on these findings, measurement of U_∞ was repeated by means of PIV measurements, which will be discussed in the next chapter.

Flow shields

The flow shields from fig. 3.4 were designed to hamper the fluid motion observed in fig. 3.23, which enters via small gaps. This fluid causes a recirculative flow above the test plate, which becomes more volatile with increasing U_∞. For more design details regarding the flow shields, see appendix C.
The influence of this recirculative flow on C_D was investigated by performing 5 independent series of tests. These were measured without the presence of the flow shields, and compared to the data of fig. 3.21. Because the recirculative flow was only noticed for $U_\infty \geq 1\frac{\mathrm{m}}{\mathrm{s}}$, measurements were performed starting at this velocity.

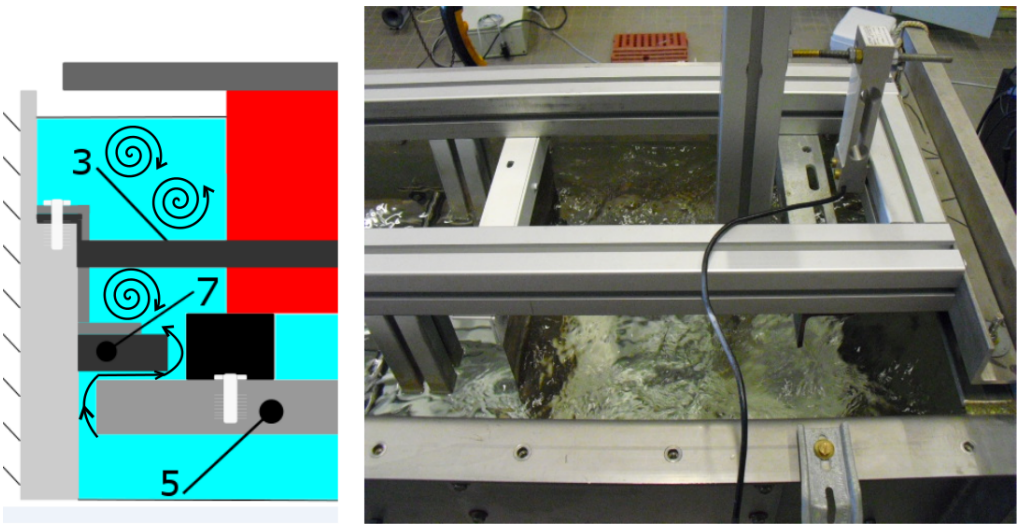

Figure 3.23: Left : Zoom of fig. 3.4, with flows shields(7)
Right: Fluid motion due to absence of shields

Fig. 3.24 shows the results for these measurements and the comparison with the data from fig. 3.21. It can be seen that the presence of the shields increases the drag of the plate, as the recirculative flow is hampered. Therefore the motion of the leaf springs is less obstructed, resulting in higher F_D.
Secondly the uncertainty of the measurements increases, which can be explained by the same phenomena. By placing the flow shields, an external forcing term is removed, which stabilizes the plate movement. The main conclusion is that the flow shields are vital for measuring only the drag over the plate, as the drag reducing recirculation in fig. 3.23 is removed.

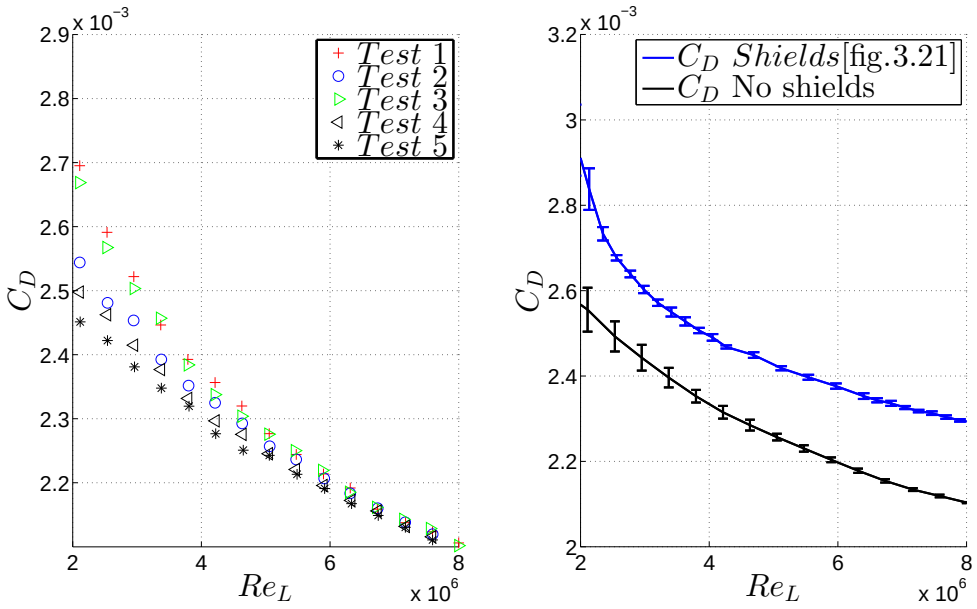

Figure 3.24: Left : C_D without shields for 5 measurements
Right: Averaged C_D with and without shiels

Side wall effects

The boundary layer that develops over the test plate in fig. 3.3 also develops for the side wall, generating 3-dimensional effects. Referenced TBL research mentioned in the literature study[Pulles et al., 1989][Nugroho, 2015][Walsh, 1982], work around this effect by coating only a small area around the centerline of the plate. The properties are then measured locally using either Laser Dopler Anemometry or hot-wires. Because of the test sections limitations, replicating this procedure is not entirely possible. To still obtain an estimate of the side wall effects, a flush mount plate, see fig. 3.25 was designed. This flush plate has a lower width than the original plate, meaning it only registers the drag force for the center flow.

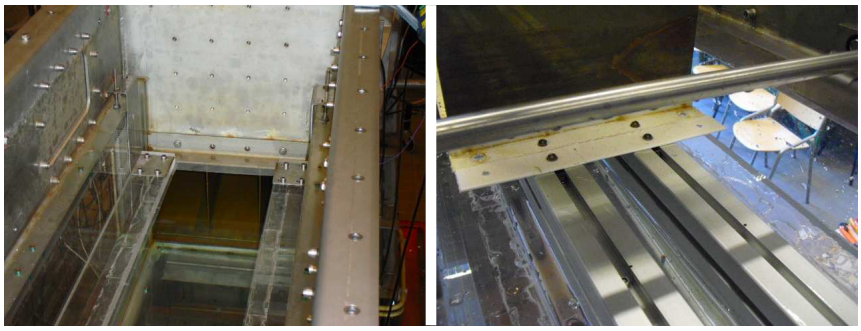

Figure 3.25: Left : Fixed wall parts before mounting the flush plate
Right: Flush plate mounted to the moving frame

The width of the flush mount is 21.98 cm, which is based on the TBL thickness at the end of the section for U_∞ 1 $\frac{\text{m}}{\text{s}}$ using eq. 2.3, which for the given conditions is approximately 4 cm. This velocity was chosen as starting point, because for lower U_∞ the resulting flush mount plate became too small to mount. Fig. 3.26 shows C_D for the flush mount plate based on 5 independent measurements. When comparing it to full-sized original plate in the right figure, it can be observed the flush mount plate registers less drag. This indicates that the 3-dimensional effects cause drag increase for the full mounted plate.
These results should however be tested again, as the curve is not continuous and exhibits jumps at Re_L 2.8×10^6 and 4.0×10^6. Although an exact reason for this behaviour is not known, a possible explanation is the adhesion of flush mount plate to the flow guidance strips which are attached to the fixed wall parts in the left plot of fig. 3.25. This was however not observed when the plate was mounted.

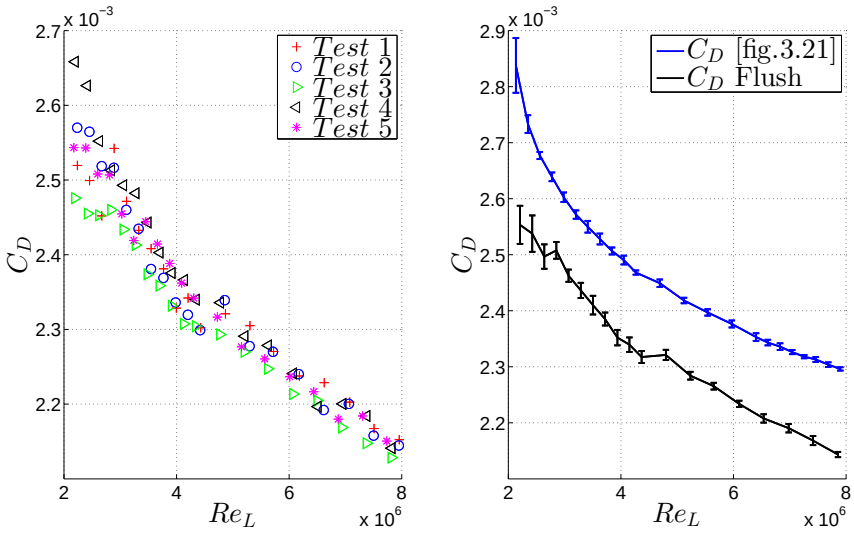

Figure 3.26: Left : C_D flush mount plate for five measurements
Right: AveragedC_D for the flush mount and original plate

Force calibration

The calibration of the load cell in section 3.2.1. showed that its systematical error is very small. During measurements however, it is coupled via the leaf-springs system to the moving plate, see fig. 3.3.
To see if linearity also holds for this coupled system, the calibration of section 3.2.1. is repeated. First the load cell is directly calibrated as done in this section after which it is coupled to the moving frame. The loading is repeated for the coupled system.

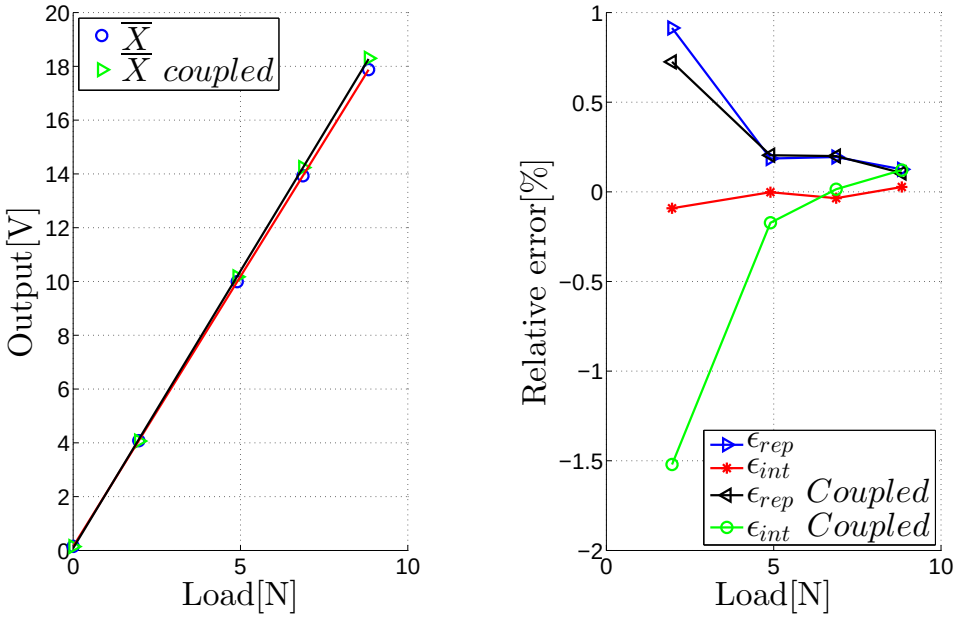

Figure 3.27: Left : Voltage output for directly loaded cell and the coupled system
Right: ϵ_{int} and ϵ_{rep} for directly loaded cell and the coupled systeme

Fig. 3.27 shows the sensor results for these tests. It can be seen that the response is clearly linear, although with a slightly steeper slope. This means coupling gives a lower stiffness of the system, i.e. causes more movement of the load cell.
Analysing the error shows that repeatability is nearly the same for both loading types. The interpolation error however is amplified, meaning that the coupled system starts behaving non-linear for low loads. This means that for low U_∞ the measurements are prone to misreading, which gives one explanation for the flattening of the C_D curve in fig. 3.21.

3.4.6 Reproducibility

If a measurement is reproducible, it can be replicated by another researcher for comparable measuring conditions. The results of fig. 3.21 were obtained for independent measuring conditions, described in section 3.3.1. During these tests the allignment angle remains constant, the operator is the same person, temperature variations of water are negligible and experiments are performed on the same day.
To investigate the change of operator and slightly varying conditions which are in effect when measuring over several weeks, 4 measurement series were performed by Florian Charruault, a PhD student at the FM group. These measurements used a comparable measuring time t_m as defined in section 3.4.4. The main differences between these measurements and the data from fig. 3.21 are listed below:

1. Change of operator
2. Measurements performed over several months
3. Mean temperature varied between $18 \leq T \leq 23\ ^\circ C$

4. The membrane of the pressure sensor was removed from its housing and replaced, yielding a new slope for its conversion curve

5. The force sensor was replaced between measurements by a similar model

6. The mounting of section 3.3.1 is redone for every test, yielding a non-constant but O(0.03°) allignment angle

Fig. 3.28 shows the 4 measurements by Charruault. The left plot shows the raw data, from which Test 1 stands out. Although exact circumstances for this measurement are not known, it is assumed a mistake was made and it is not included in the second plot.

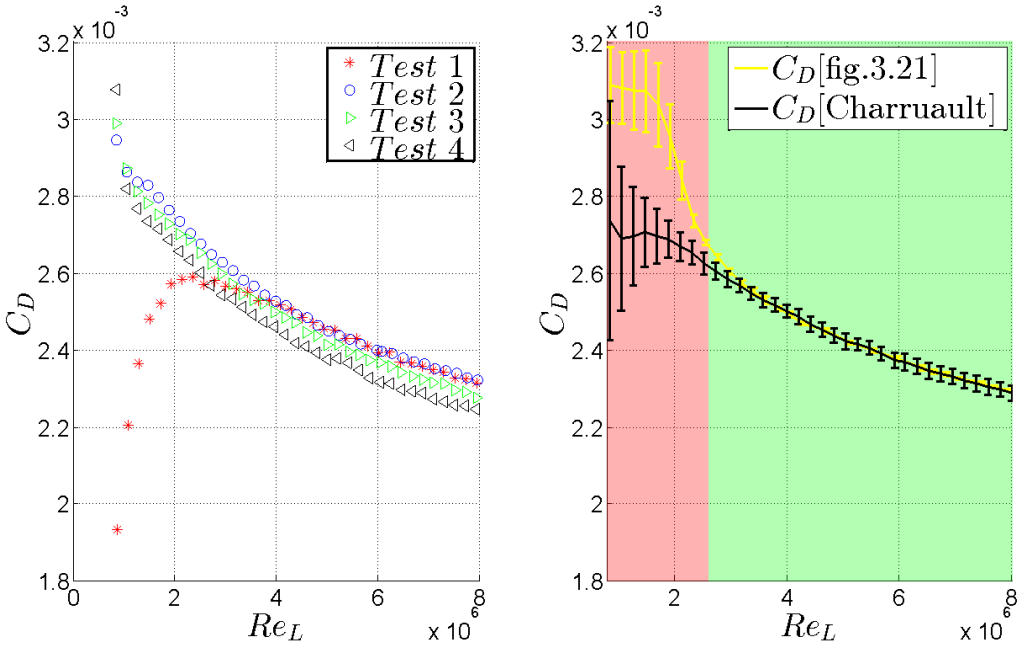

Figure 3.28: Left : Measurements performed by Charruault [2016]
Right: Reproducibility of C_D with reproducible regime in green and non reproducible in red

The right plot displays the mean, minus test 4, for the tests and the corresponding uncertainty. It also shows the curve from fig. 3.21 for comparison. For $Re_L \geq 3 \times 10^6$ measurements are very reproducible, as both C_D and μ_{C_D} nearly collapse on the same curve. This area is shaded green. The uncertainty for Charruault [2016] is however larger, which is presumably caused by the varying of the allignment angle. The measurements for lower Re_L don't show this reproducibility, as the curves strongly diverge for $Re_L \leq 2.4 \times 10^6$, which is shaded red. Causes for this behaviour are the interpolation error of both pressure and force sensor, which are higher for lower values. Also the varying allignment angle of the test plate is assumed to disturb the force measurements for very low values. Another reason not yet discussed is the non-repeatability of the TBL for low velocities, which will be discussed in the next chapter.

The main conclusion from fig. 3.28 is that measurements for $Re_L \leq 2.4 \times 10^6$ are not well reproducible and should not be used for analysis. The intermediate regime of $2.4 \leq Re_L \leq 3 \times 10^6$ is still considered reproducible, because μ_{C_D} still overlaps in this region. Thus measurements are repeatable and reproducible for $Re_L \geq 2.4 \times 10^6$.

3.4.7 Conclusion on error analysis

This section was devoted to analyse error of the setup. This was necessary to accomplish research objective 1, which states

1. Develop an accurate drag plate measurement procedure that allows 1% precise drag reduction studies at the TU Delft cavitation tunnel

Using the procedure from section 3.3.1 and the derived measuring time from section 3.3.4, it was found drag results are well repeatable for $U_\infty \geq 2.2\frac{\mathrm{m}}{\mathrm{s}}$. This behaviour was also reproduced for change of operator, small variation of allignment angle and performing measurements over several months.
Uncertainty analysis showed that the velocity and force contribute the most to the overall uncertainty of C_D. Using the propagation of uncertainty, a measuring time scheme was derived which ensured 1% accuracy, although resonance causes overestimation of t_m.
Several bias effects influence the measured results. Flow between test plate and side walls, as well 3-dimensional effects caused by the side wall cause an overall reduction in measured drag. Both effects are inherent to the cavitation tunnel and cannot be eliminated, although flow shields reduce the flow between the test plate and the gaps.
The coupling of the force sensor to the leaf-spring system causes a slight bias, although this only affects the very low velocities outside the accurate region. The pressure sensor which determines the sections freestream velocity however, showed significant bias when compared to Pitot tube measurements in the test section. Due to inconsistent results between the two used tubes, this effect could not be quantified. PIV in chapter 4 was used to quantify this effect.

The following list summarizes the main finding from this chapter:

- Measurements are well repeatable and reproducible for $Re_L \geq 2.4 \times 10^6$ which corresponds to $U_\infty \geq 2.2\ \frac{\mathrm{m}}{\mathrm{s}}$
- The velocity, drag force and their respective correlation, contribute the most to μ_{C_D}
- The propagation of uncertainty is a reliable tool for estimating the measuring time to reduce the uncertainty, although signal analysis into the resonance could improve its estimation
- The gaps between the side walls and the test plate cause a recirculative flow above the plate, which reduces the overall C_D. Using flow shields above these gaps reduces this effect
- The TBL measured in the test section is subject to 3-dimensional effects of the side walls. Flush mount tests indicate these elevate the measured C_D, although more tests are needed to confirm this behaviour
- The leaf-spring system introduces a slight bias for very small values of F_D, which does not effect C_D for accurate measurements
- The contraction exit velocity U_∞ measured by the pressure sensor is not the velocity present in the test section. The actual value of the freestream velocity could not be determined for 2 independent Pitot tube measurements, although both measure a lower velocity than U_∞

Chapter 4

PIV Measurements

Particle imaging velocimetry [PIV] measurements are a tool that allow accurate study of the TBL. The need for studying the flow was already discussed in the former chapter. Pitot tube measurements showed a difference between the freestream velocity in the contraction and test section existed.

Using the PIV measured velocity in the test section, a correction is made to the freestream velocity. By measuring U at several positions, the pressure gradient is analysed. This is important, as mild pressure gradients can significantly change riblet performance.
The TBL is studied by estimating the displacement and momentum thickness from the near wall velocity profile. Using the first, a least-square fit is made to determine the TBL origin. This data is then used to validate the performance of the zigzag strip.
Next the logarithmic layer is analysed for both mean flow and the Reynolds shear stress. Using the law of the wall, the measured profile is compared to the theory. Finally the Reynolds shear stress is used to make an estimation of the local riblet performance, using the FIK identity.

4.1 Principle

PIV is a measurement technique that allows instantaneous measurement of velocity fields. This is done by seeding the investigated flow with tracer particles, which are sufficiently small to track the flow movement. These particles are then illuminated by a laser sheet from which snap shots are taken by a camera, see fig. 4.1.

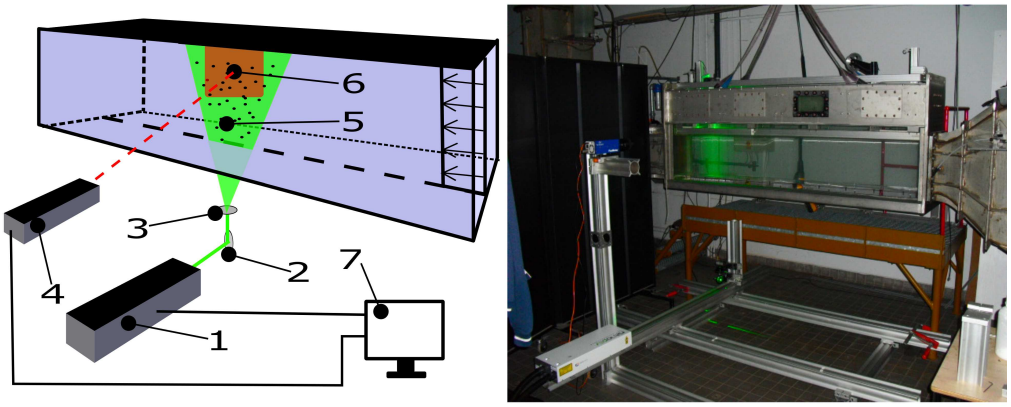

Figure 4.1: Left : Schematics of setup with main components: Litron laser class L:50-50 (1), mirror(2), cylindrical lens (3), CCD camera (4), laser sheet with tracer particles (5), image plane (6) and DAVIS integrated system (7)
Right: PIV setup

An impression of these raw snap shots is given in fig. 4.2. To reconstruct the instantaneous velocity field in the right plot, two consecutive dot patters like the left plot are taken, shortly after another. The particle patterns are then correlated between the two figures, yielding the velocity field in fig .4.2

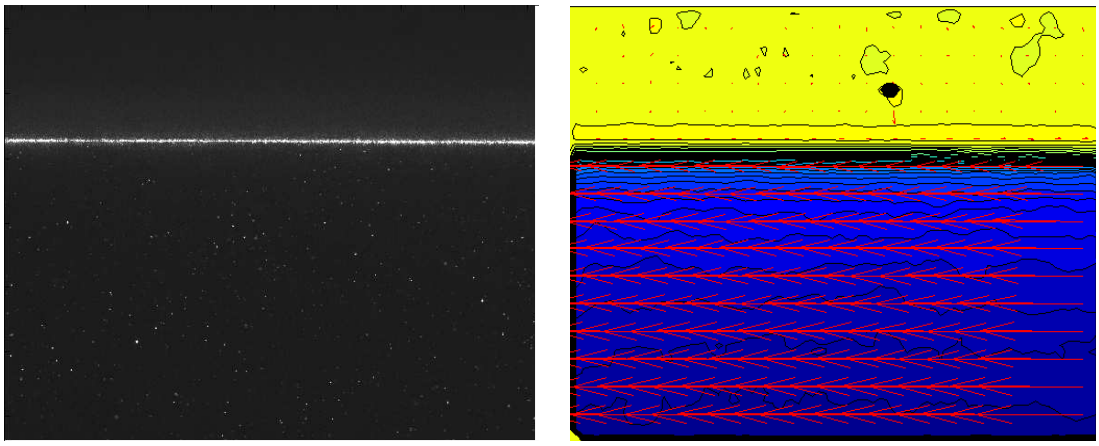

Figure 4.2: Left : Dot pattern imaged by camera
Right: Velocity field

4.2 General design

4.2.1 Field of view

Though many different forms of PIV, such as tomographic and stereoscopic exist and are available, this work focus is on 2-dimensional planar PIV. Fig. 4.3 displays the field of views [FOV] that were used at three positions along the centerline to minimize side wall effects.
Table 4.1 shows the dimensions of the FOV and the distance of the positions to the leading edge of the test plate. Using these frames and positions, several aspects of the flow were investigated.

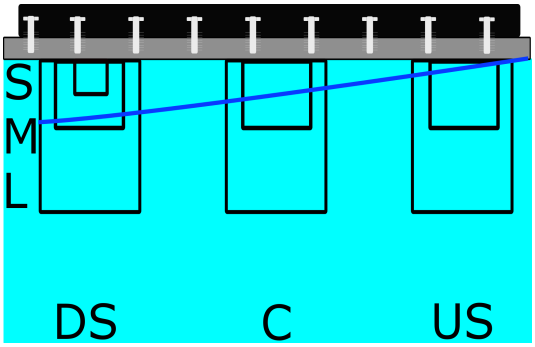

Figure 4.3: FOV and positions

Table 4.1: Codation PIV

A: FOV

FOV name	Code	Dimensions[cm]
Large	L	13×12
Medium	M	6×5.5
Small	S	1.25×1

B: Positions

Position	Code	Distance[m]
Upstream	US	0.27
Centre	C	1.00
Downstream	DS	1.73

The large frame was used to study the magnitude and shape of the freestream velocity. As indicated by the Pitot tube measurements, see section 3.4.5 and Appendix A, a mismatch between the velocity in the section and the one measured in the contraction exists. Also any velocity and pressure gradient effects can be analysed.
The medium frame allows the study of the boundary layer thickness and origin. Using this frame at the 3 positions, a least-square fit based on the one-seventh powerlaw can be made to determine the TBL origin.
Finally the small frame was used to study the flow inside the log region. Firstly the mean flow was studied and compared to the law of the wall. Secondly the Reynolds stress was computed, although results remain inconclusive due to large uncertainty.

4.2.2 Measuring parameters

This section treats the main design parameters of the PIV system and corresponding FOV properties. All design rules presented in this part were taken from Adrian and Westerweel [2011].

Magnification factor

Based on the FOV, the magnification factor can be determined by:

$$M = \frac{camera\ chip\ size}{FOV\ size} \tag{4.1}$$

With the chip size equalling the dimensions of the small FOV, this yields the factors presented in table 4.2 at the end of the section.

particle size

The particles used in all experiments are hollow sphericell with diameter ,d_p 10 μm, and density, ρ_p O(10^3) $\frac{\text{kg}}{\text{m}^3}$. This then gives particle response time:

$$t_p = d_p^2 \frac{\rho_p}{18\mu} \Longrightarrow 5.6\mu\text{s} \tag{4.2}$$

Which shows that t_p is much smaller than the defined mean flow timescale t_f in the former chapter for the outer flow. Because the mean flow timescale is in the order of seconds, it holds that the particle stokes number:

$$St_p = \frac{t_p}{t_f} \tag{4.3}$$

will be smaller than 0.1, meaning the particles are well able to trace the mean flow.

Interrogation window size and timescales

All interrogation windows where chosen 16×16 pixel. Knowing the pixel dimensions of the chip to be 1280×1024, the vector spacing with 50% overlap of windows becomes:

$$dx = 8\frac{\text{pixel diameter}}{M} \tag{4.4}$$

with pixel diameter being 11 μm. Table gives the spacings for the FOV. Using these dimensions for the interrogation window, the number of vectors becomes 160×128.

To obtain correct measurements two timescales must be defined, namely the interrogation and difference time. The first is the time between two constitutive snapshots from which one velocity snapshot is reconstructed. An upper bound is given by the one-quarter rule, which states the particle displacement between 2 consecutive frames must be less then a quarter of the interrogation window size. It is given by:

$$t_{int} = \frac{1}{4}\frac{X_{frame}}{U_{pos}^{FOV}} \tag{4.5}$$

where X_{frame} is the FOV width and U_{pos}^{FOV} is the recorded velocity for the used FOV at the named position. This definition works well for the outer flow which is uniform, except for the near wall region. For the medium and small frame where the TBL velocity profile varies this offers some challenge. Fortunately experiments showed that choosing a value based on the weighed average of the profile displacement works well.

To garuantee the two snapshots are independently taken from the next pair the difference time must be

sufficiently large. The difference time t_{diff} is the time between two pairs of consecutive snap shots. A lower bound is given by:

$$t_{diff} = \frac{X_{frame}}{U_{pos}^{FOV}} \tag{4.6}$$

which represent the time before the fluid in the FOV is refreshed. Multiplying t_{diff} with the number of taken snapshots N_{PIV} gives the measurement time t_{PIV}:

$$t_{PIV} = (N_{PIV} - 1)\, t_{diff} \tag{4.7}$$

To obtain good repeatability, while not overloading the PIV system, N_{PIV} is chosen at 500.

Uncertainty

The uncertainty of the PIV system is determined by the particle displacement and the interrogation time:

$$\mu_{U_{pos}^{FOV}} = \frac{1}{t_{int}} \sqrt{(U_{pos}^{FOV} \mu_{t_{int}})^2 + (\mu_{dx})^2} \tag{4.8}$$

The Davis system evaluates this value at $\mathrm{O}(\frac{1}{2})$ $\frac{\text{pixel}}{\text{s}}$ between two consecutive shots. When the $\frac{1}{4}$-rule is applied, the relative error is given by:

$$\frac{\mu_{U_{pos}^{FOV}}}{U_{pos}^{FOV}} = \frac{0.5}{4} = 12.5\% \tag{4.9}$$

for one velocity frame. Since 500 independent velocity frames are constructed this means the final uncertainty of the PIV system is:

$$\mu_{U_{pos}^{FOV}} = \frac{12.5}{\sqrt{500}} \approx 0.5\% \tag{4.10}$$

Table 4.2: Magnification factor and vector spacing of the FOV

FOV	M	dx[mm]
L	15	14.3
M	5	3.4
S	1	0.1

4.2.3 Used equipment and safety

Besides the equipment mentioned in fig. 4.1 the setup was supported by a fixed frame which can also be seen in the same fig. To guard the operators from harmful laser light, the entire measurement was shielded and safety goggles were worn. To protect by-passers from scattered light, the facility was locked during operation and any windows shielded by thick curtains.
These were all part of the safety regulations according to the TU report no. 5-02 and no.1-94 which are based on IAVM report no.12:"Richtlijnen laserveiligheid, voor research en onderwijs". Details of the specific safety report and used laser can be found in Appendix D.

4.3 Outer Flow

Using the large frame, the freestream velocity was compared to the contraction exit velocity U_∞. This was done by performing measurements of 500 consecutive paired shots at the 3 positions for the velocities, see table 4.3. These were then averaged to return a single velocity field with the properties mentioned in the former section. Due to time restrictions, these measurements were only performed once, assuming the repeatability error is small.

4.3.1 Velocity correction

Fig. 4.4 shows the averaged velocity contour fields for U_∞=1 $\frac{\mathrm{m}}{\mathrm{s}}$ at the 3 positions. The colorbar right to every plot displays the streamwise velocity magnitude in the figures. From the colour intensity it can be seen that the contraction exit velocity U_∞ is not measured in the test section.
Every subplot also displays the contour of the velocity profile at the center of each frame. Note that this velocity curve is not drawn to scale. It can be seen that beyond the boundary layer, the freestream velocity is uniform.
Using this uniform region, the average velocity $\overline{U_{pos}^{FOV}}$ is measured. This average is computed from all the velocity data in the drawn rectangle, which is also displayed in the legend of fig. 4.4. The results of $\overline{U_{pos}^{FOV}}$ for several values of U_∞ are given in table 4.3.

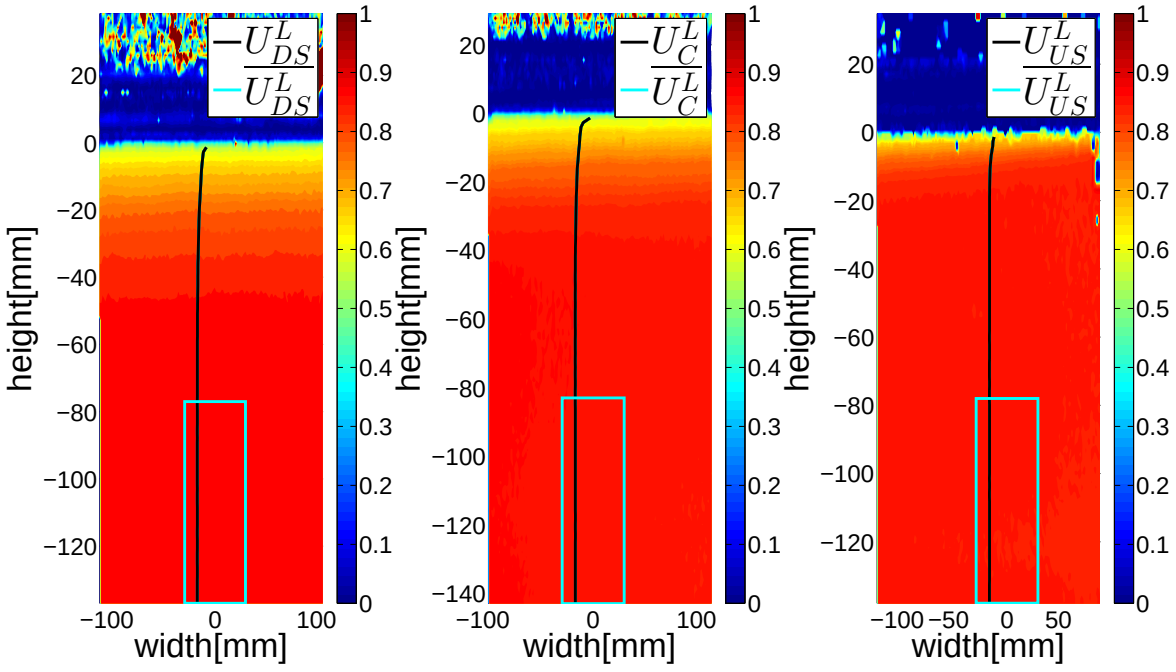

Figure 4.4: PIV results U_∞=[1$\frac{\mathrm{m}}{\mathrm{s}}$] for the large FOV

This table shows the measured freestream velocities for the 3 measuring positions against U_∞. It shows that this value is not measured in the section. To evaluate this difference, table 4.3 also displays the ratio of the measured velocity by the PIV system and U_∞.
These ratios are also plotted in fig. 4.5. On average, the velocity difference is O(86.5%), although this value approximately decreases with U_∞. The decreasing trend can be explained by re-analysing the velocity computation in fig. 3.5.
Its resulting pressure to velocity conversion, eq. 3.4 is based on the assumption no friction is present in the contraction. This is however incorrect as the TBL in the contraction is subject to a pressure gradient. This causes fluid displacement, meaning the overall fluid flux is lower.

Table 4.3: Freestream velocities for the large FOV

$U_\infty[\frac{m}{s}]$	$U^L_{US}[\frac{\mathrm{m}}{\mathrm{s}}]$	$\frac{U^L_{US}}{U_\infty}[\%]$	$U^L_C[\frac{\mathrm{m}}{\mathrm{s}}]$	$\frac{U^L_C}{U_\infty}[\%]$	$U^L_{DS}[\frac{\mathrm{m}}{\mathrm{s}}]$	$\frac{U^L_{DS}}{U_\infty}[\%]$
0.4	0.33	83.4	0.34	86.8	0.35	87.1
0.6	0.51	85.0	0.52	86.5	0.52	87.3
0.8	0.68	85.2	0.69	86.4	0.70	87.4
1.0	0.85	85.4	0.86	86.1	0.87	87.4
1.2	1.02	85.6	1.03	85.9	1.04	87.4
1.4	1.19	85.6	1.21	86.1	1.22	87.2
1.6	1.37	85.6	1.38	86.0	1.40	87.2
1.8	1.54	85.7	1.55	85.9	1.57	87.2
2.0	1.71	85.7	1.72	86.1	1.74	87.2
3.0	2.58	86.1	2.59	86.2	2.62	87.4
4.0	3.49	86.3	3.48	86.9	3.52	88.1

Fig. 4.5 also shows that a significant difference in freestream velocity between the frame exists, indicating the flow is subject to a favorable pressure gradient. This holds especially for the trends between the US and DS frame, which show very similar behaviour. This will be analysed in section 4.3.2.

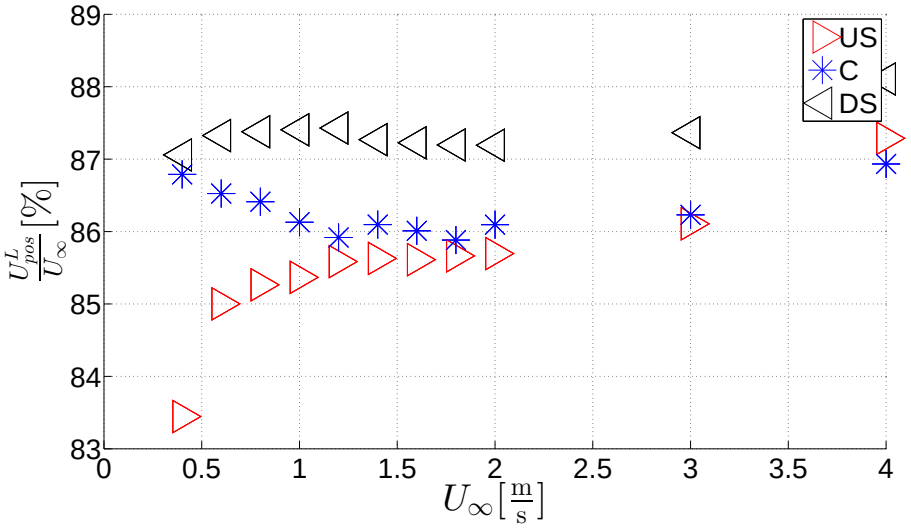

Figure 4.5: Velocity difference

Using the data from table 4.3 a corrected velocity $\overline{U}$ is defined:

$$\overline{U} = \frac{U^L_{US} + U^L_C + U^L_{DS}}{3} \tag{4.11}$$

which is the weighed average from the results of table 4.3.

Rather than re-plot all figures from chapter 3, the effects of correcting U_∞ by $\overline{U}$, can be explained by redrawing fig. 3.28, which is shown below.

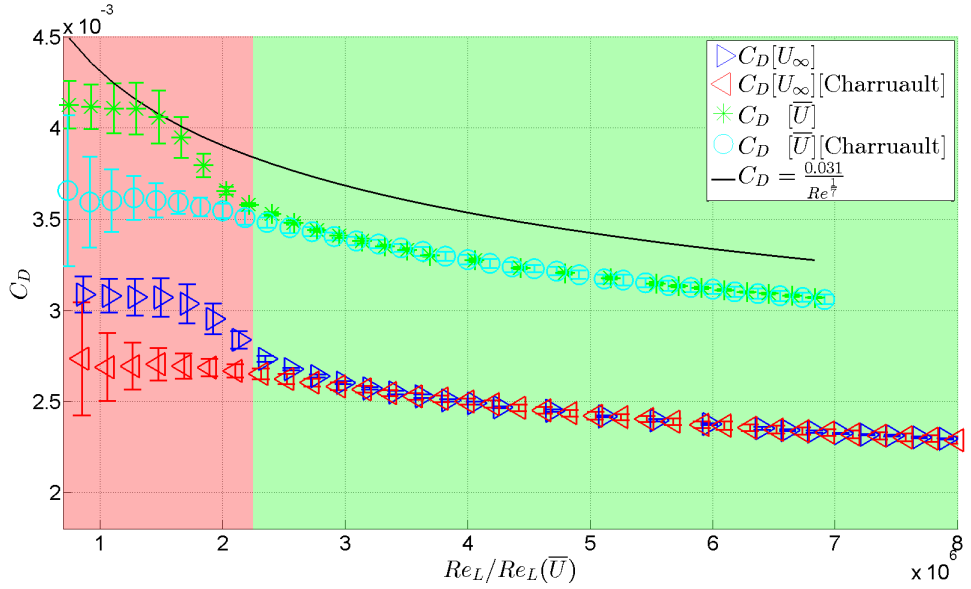

Figure 4.6: C_D corrected for $\overline{U}$

This fig. shows the original data for U_∞ and the corrected data for $\overline{U}$, against their corresponding Reynolds number. The main effect that is observed is the large shift upwards of C_D, because of its quadratic inverse relation to the freestream velocity. Another effect is the horizontal shift of the curve due to the change of the Reynolds number.
This has two implications. Firstly, the measuring regime $0.4 \leq U_\infty \leq 4$ rescales to $0.33 \leq \overline{U} \leq 3.5\frac{\text{m}}{\text{s}}$. Secondly the range of Re_L for which drag is considered reproducible shifts sligtly. This reproducible regime thus becomes $Re_L(U_\infty) \geq 2.2 \times 10^6$ which corresponds to $\overline{U}$=1.1$\frac{\text{m}}{\text{s}}$.

Although the corrected C_D approaches theory much better due to the velocity correction, it is still significantly less. This is partly caused by the bias effects discussed in chapter 3. Another reason is the origin of the TBL, which up till now has been assumed to be at the leading edge of the plate. This assumption will be analysed in the next section.

4.3.2 Pressure gradient

From fig. 4.5 it can be concluded that the mean flow is subject to a favorable pressure gradient. Boomsma and Sotiropoulos [2015] showed that an adverse pressure gradient can increase the performance of the riblets, although the magnitude must be significant. Although a favorable gradient is not researched in this work, it shows that significant values of $\frac{dP}{dx}$ affect DC, which is undesired. The strength of $\frac{dP}{dx}$ is evaluated by the Clauser parameter:

$$\beta = \frac{\delta^*}{\tau_{wall}} \frac{dP}{dx} \tag{4.12}$$

where δ^* is the displacement thickness, τ_{wall} the wall shear stress and $\frac{dP}{dx}$ the pressure gradient. To obtain an estimate of the latter, it is assumed Bernoulli can be applied to the outer flow, where friction is negligible:

$$-\frac{dP}{dx} \approx \frac{1}{2}\rho \frac{\left(U_{DS}^L\right)^2 - \left(U_{US}^L\right)^2}{L} \tag{4.13}$$

for which the results are given in table. 4.4. This table also contains the displacement thickness at the dowstream position, which is taken from next section. To close eq. 4.13, τ_{wall} is determined by:

$$\overline{\tau_{wall}} = \frac{1}{2} C_D \rho \overline{U}^2 \tag{4.14}$$

where the drag coefficient is taken from fig. 4.6 for $\overline{U}$. To obtain the highest estimate of β; $\overline{U}$, $\frac{dP}{dx}$ and δ^* are taken from U^M_{DS}. The pressure gradient is based on the velocity difference for this frame compared to the US FOV.

Table 4.4: Clauser parameter

$\overline{U}[\frac{\mathrm{m}}{\mathrm{s}}]$	δ^*[mm]	$\overline{\tau_{wall}}[\frac{\mathrm{N}}{\mathrm{m}^2}]$	$\frac{dP}{dx}[\frac{\mathrm{N}}{\mathrm{m}^3}]$	$\beta[10^{-2}]$
0.35	6.1	0.25	3.3	7.9
0.52	6.0	0.55	4.8	5.2
0.70	6.1	1.00	7.8	4.7
0.87	5.9	1.55	11.7	4.5
1.04	4.8	2.19	15.3	3.4
1.22	5.2	2.93	18.5	3.3
1.74	4.2	5.41	34.4	2.7
2.62	4.4	11.58	65.3	2.5
3.52	4.4	19.48	76.4	1.7

Table. 4.4 shows that the Clauser parameter is very small and decreases monotonously as the freestream velocity increases. This indicates the pressure gradient has a weak effect on the flow and this effect becomes less with increased velocity magnitude. According to Boomsma and Sotiropoulos [2015] this also means riblet performance is not affected by gradient effects, as $\beta = 0.5$ is not exceeded.

4.4 Boundary layer flow

The medium FOV is used to study the TBL, see fig. 4.7. It shows the TBL at the 3 measuring positions for $U_\infty = 1$. Note this is the measured value in the contraction and the actual velocity magnitude is lower.
This is again shown in table 4.5, which displays the measured freestream velocities for both large and medium frame. Comparing velocities for both frames show good repeatability, as both values were recorded for separate flow cycles described in section 3.3.1. The repeatability of the mean flow can also be seen from fig. 4.7. It displays the velocity contour for the large and medium frame which show good overlap, except for the near wall region.

Table 4.5: Freestream velocities for the medium FOV

$U_\infty[\frac{m}{s}]$	$U^M_{US}[\frac{\mathrm{m}}{\mathrm{s}}]$	$U^L_{US}[\frac{\mathrm{m}}{\mathrm{s}}]$	$U^M_C[\frac{\mathrm{m}}{\mathrm{s}}]$	$U^L_C[\frac{\mathrm{m}}{\mathrm{s}}]$	$U^M_{US}[\frac{\mathrm{m}}{\mathrm{s}}]$	$U^L_{US}[\frac{\mathrm{m}}{\mathrm{s}}]$
0.4	0.34	0.33	0.34	0.34	0.35	0.35
0.6	0.52	0.51	0.52	0.52	0.52	0.52
0.8	0.69	0.68	0.69	0.69	0.70	0.70
1.0	0.86	0.85	0.87	0.86	0.87	0.87
1.2	1.04	1.02	1.04	1.03	1.05	1.04
1.4	1.21	1.19	1.21	1.21	1.22	1.22
2.0	1.74	1.71	1.73	1.72	1.73	1.74
3.0	2.61	2.58	2.60	2.59	2.60	2.62
4.0	3.52	3.49	3.49	3.48	3.50	3.52

The main focus of this section is to investigate the TBL properties. By analysing the velocity profiles for the given velocities in table 4.5 it can be verified the flow is turbulent. Also the origin of the TBL is investigated, which up to this point has been assumed to originate at the leading edge of the plate.

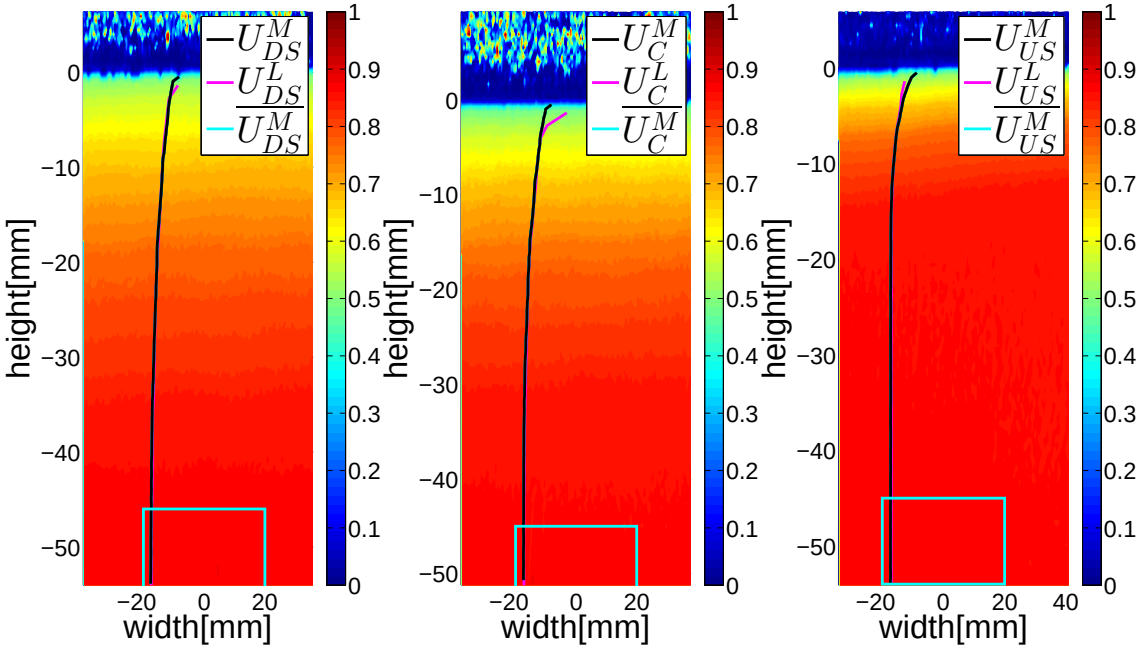

Figure 4.7: PIV results U_∞=1$\frac{\text{m}}{\text{s}}$ for the medium FOV

4.4.1 Thickness and origin TBL

The main purpose of the medium frame is to determine the TBL thickness and thereby its origin. This was done by evaluating the following parameters:

$$\delta^* = \int_0^\infty \left(1 - \frac{U}{\overline{U}}\right) \text{dy} \tag{4.15}$$

$$\theta = \int_0^\infty \frac{U}{\overline{U}} \left(1 - \frac{U}{\overline{U}}\right) \text{dy} \tag{4.16}$$

Which are the displacement and momentum thickness respectively. Both are determined by integrating the velocity profile from the wall until the freestream value, U_∞ is reached.
In contrast to the boundary layer thickness δ, δ^* uses information from the entire velocity profile and is generally considered to be a more reliable parameter. It also allows the study of the shape factor, which is given by:

$$H = \frac{\delta^*}{\theta} \tag{4.17}$$

According to White [1999] a shape factor for a TBL with no adverse pressure gradient corresponds to the value 1.3, while its laminar counterpart corresponds to $H = 2.6$.

Displacement, momentum thickness and shape factor

Table. 4.6 shows the results for δ^*, θ and H. Based on the latter, it can be seen that the TBL is turbulent for all positions. The values of H$\geq$ 1.3 indicates a small pressure gradient is present, which corresponds to the results of the former section.
According to White [1999] and Nieuwstadt [1992], both δ^* and θ should decrease as U_∞ increases. Although this decreasing trend can be seen, it is not monotonous. This is caused by the relative large vector spacing, which limits the precision. Especially at the US frame the decrease of δ^* is 0.6 mm, which corresponds to 2 times the vector spading dx. Also the assumption that the initial conditions for the TBL in the contraction remain identical as U_∞ increases, does likely not hold.

Table 4.6: Shape factor, momentum and displacement thickness TBL

$U_\infty[\frac{m}{s}]$	$\delta^*_{US}[mm]$	$\theta_{US}[mm]$	H_{US}	$\delta^*_C[mm]$	$\theta_{C[mm]}$	H_C	$\delta^*_{DS}[mm]$	$\theta_{DS}[mm]$	H_{DS}
0.4	2.5	1.8	1.32	5.8	4.3	1.37	6.1	4.5	1.34
0.6	2.2	1.7	1.34	5.3	3.9	1.37	6.0	4.5	1.33
0.8	2.4	1.7	1.37	5.4	3.8	1.41	6.1	4.6	1.34
1.0	2.4	1.7	1.41	5.5	3.8	1.47	5.9	4.4	1.34
1.2	2.3	1.6	1.38	5.3	3.6	1.44	4.8	3.7	1.32
1.4	2.0	1.5	1.31	4.4	3.3	1.34	5.2	3.9	1.29
2.0	1.8	1.5	1.24	3.8	2.8	1.32	4.3	3.3	1.29
2.5	1.7	1.4	1.22	3.7	2.9	1.31	4.3	3.3	1.28
3.0	1.8	1.5	1.22	3.9	3.0	1.31	4.2	3.3	1.28
3.5	1.8	1.5	1.21	3.8	2.9	1.30	4.4	3.4	1.28
4.0	1.9	1.5	1.23	3.9	3.0	1.31	4.4	3.5	1.28

Boundary layer thickness

For a boundary layer growing with a one-seventh powerlaw the thickness is given by:

$$\delta_x = 0.16\frac{x}{Re_x^{\frac{1}{7}}} \tag{2.3}$$

which assumes the TBL originates at the leading edge of the drag plate. This value is given as a reference in table 4.7. This table also contains δ^{99}, which is the height where the measured velocity$\geq$ 99% $\overline{U}$. It also shows the thickness based on the displacement thickness, taken from[White, 1999]:

$$\delta \approx 8\delta^* \tag{4.18}$$

where δ^* is taken from table 4.6. Table 4.7 gives the results of these measurements and the theoretical value corresponding to velocity magnitude and position. Both methods for determining δ give a higher value than the theory indicates. This means the origin of the TBL lies before the leading edge of the plate, which will be analysed next.

Table 4.7: TBL thickness for δ^{99}, $8\delta^*$ and theoretic reference[White, 1999]

$\overline{U}[\frac{m}{s}]$	$\delta^{99}_{US}[mm]$	$8\delta^*_{US}[mm]$	$\delta_{US}[mm]$	$\delta^{99}_C[mm]$	$8\delta^*_{C[mm]}$	$\delta_C[mm]$	$\delta^{99}_{DS}[mm]$	$8\delta^*_{DS}[mm]$	δ_{DS}
0.34	20.2	19.6	8.3	38.4	46.8	25.9	41.1	48.7	41.5
0.52	17.4	18.1	7.8	36.0	42.8	24.4	41.1	48.3	39.1
0.69	17.4	19.2	7.5	35.5	43.2	23.4	42.0	48.9	37.5
0.87	17.4	19.1	7.3	35.5	44.3	22.7	41.1	47.1	36.4
1.04	16.9	18.0	7.1	35.1	42.1	22.1	38.3	38.8	35.4
1.21	16.4	15.9	6.9	34.1	35.0	21.6	40.2	41.4	34.7
1.73	16.0	14.5	6.6	33.6	30.1	20.6	40.6	34.3	33.0
2.18	16.0	14.0	6.4	36.5	29.5	19.9	40.2	34.1	31.9
2.61	16.4	14.6	6.2	38.9	30.9	19.4	37.3	33.2	31.1
3.05	17.4	14.4	6.1	37.4	30.2	19.0	41.6	35.1	30.4
3.49	19.3	14.6	5.9	37.9	31.3	18.6	39.7	35.6	29.9

Comparing both methods, it can be seen the displacement thickness gives a more monotonous decreasing trend of the TBL growth with increasing $\overline{U}$. This is because δ^* uses information from the entire boundary layer profile in contrast to δ^{99}, which is based on finding a single point. The latter is also limited by the vector spacing, which was explained in the former section.

Determining TBL origin

By least-square fitting eq. 2.3 to the data of table 4.7 an estimate of the origin of the TBL can made. Because δ based on δ^* is of better quality, this data will be used. Fig. 4.8 shows this fitting method for four characteristic velocities.

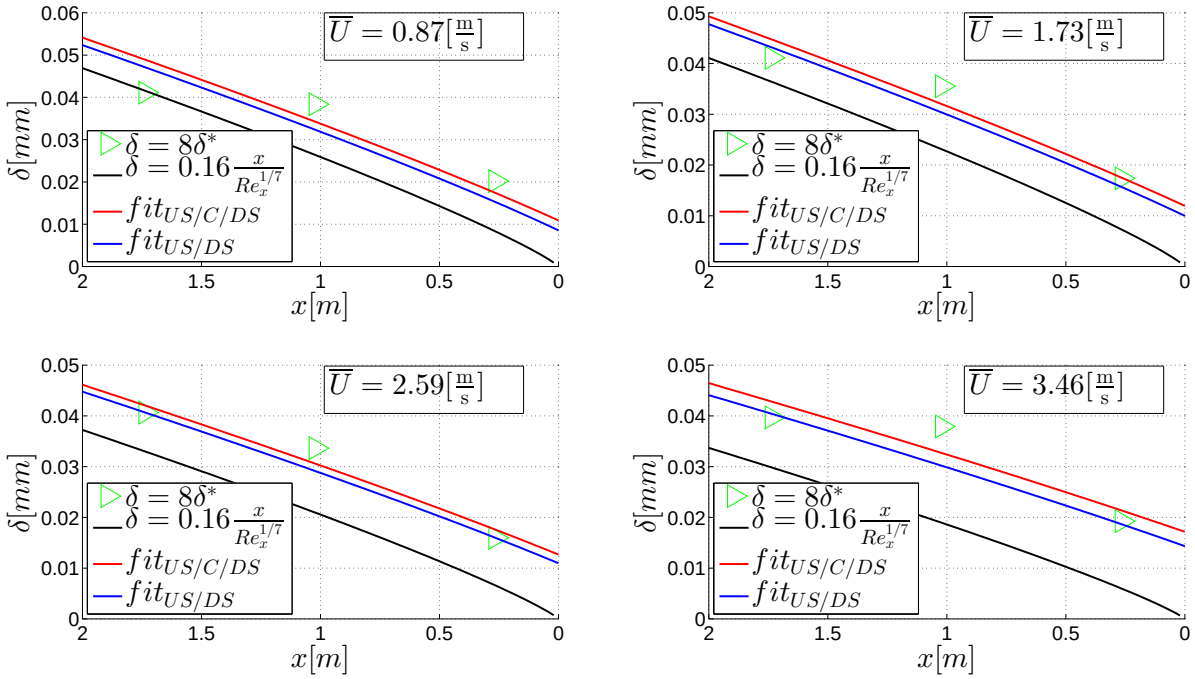

Figure 4.8: Fit of the one-seventh powerlaw to δ for several $\overline{U}$

Fig. 4.8 shows the measured thickness and the theoretical value based on eq. 2.3. It also displays two data fits; $Fit_{US/C/DS}$ which uses all frames and $Fit_{US/DS}$, which only uses the US and DS FOV.
For all situations it can be seen that the TBL is thicker compared to the theory, meaning the origin of the TBL lies before the leading edge of the plate. The plots from fig. 4.8 also show that the estimations of the center frame do not collapse on the fitted $\frac{1}{7}$ curves. Reasons for this are not clear and due to a lack of other positions where δ was determined, a strict conclusion on the TBL growth cannot be made. All data however shows that the TBL originates before the plate.
Table 4.8 shows the virtual origins of the TBL, according to the powerlaw for both fits. Both estimate the origin of the TBL before the leading edge of the drag plate. This origin shifts upstream as the magnitude of the freestream velocity increases, meaning the boundary layer transitions earlier to turbulence.

Table 4.8: Virtual origins TBL before leading edge test plate

$\overline{U}[\frac{m}{s}]$	$-\ x_{or}\ Fit_{US/DS}$ [cm]	$-\ x_{or}\ Fit_{US/C/DS}$[cm]
0.34	27.4	36.4
0.52	28.2	36.7
0.69	35.9	43.7
0.87	38.3	47.3
1.04	34.0	45.0
1.21	53.5	68.6
2.61	49.7	72.9
3.05	69.3	85.3
3.49	73.7	91.0

The data from table 4.8 can be used to calculate a corrected value of C_D, which includes the varying origin of the TBL. This correction is given by:

$$C_D^{cor} = C_D(Re_{(L+x_{or})}) - C_D(Re_{x_{or}})\frac{x_{or}}{L} \tag{4.19}$$

for which the results are shown in in fig. 4.9 which shows the data from fig. 4.6. Besides the theoretic curve from eq. 3.3 it also show the corrected values of C_D based on the varying origin of the two fits. The correction shows that the measured C_D and the theoretic value of C_D again mismatch, where the latter now has the smaller magnitude. This difference might be a result of the side wall effects that were measured with the flush mount plate in section 3.4.5. This section showed the overall C_D is increased due to these flow effects.

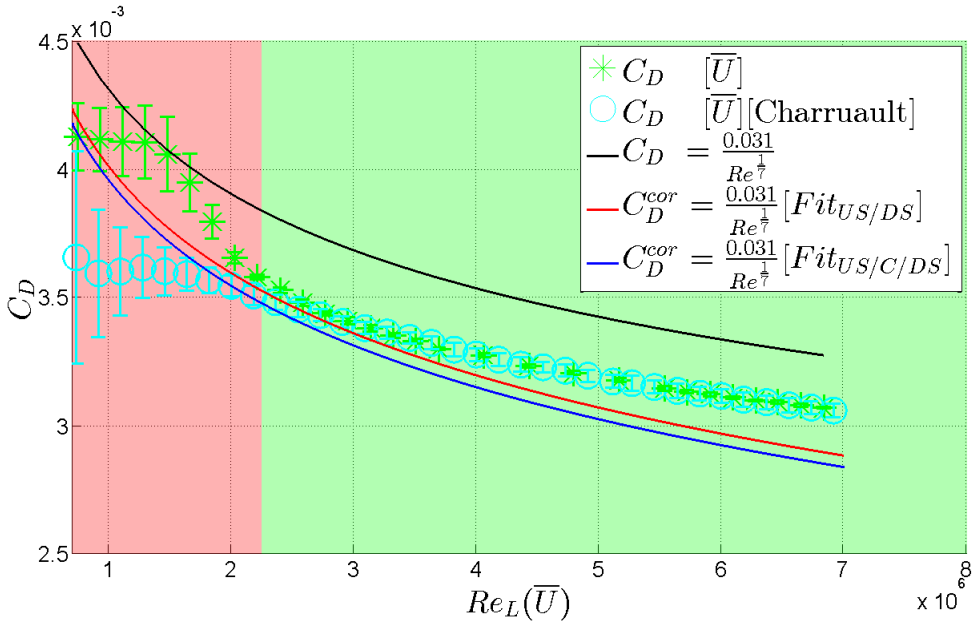

Figure 4.9: Effect of varying origin TBL on C_D

4.4.2 TBL repeatability

Fig. 4.7 and table 4.5 already showed that results for the outer flow are well repeatable, meaning the freestream velocity in the test section is nearly identical for a restart of the setup. To check if this also holds for the boundary layer itself, the tests for the DS FOV were repeated 4 times. Fig. 4.10 displays 4 velocity profiles similar to fig. 4.7 at the DS FOV. Between these measurements, the entire tunnel was stopped, after which the flow was restarted.
Due to some challenges with alligning the test plate and the camera, these velocity profiles were taken for a slightly different FOV compared to the DS frame in fig. 4.7. Firstly, only 4 [cm] of the flow could be visualized. Secondly, reflections caused problems measuring at the DS position, therefore the entire FOV was translated 10 cm downstream. Because variation of TBL properties are very weak downstream, it is assumed a comparison with the data from section 4.4.1. is still valid.

Table 4.9: Repeatability of TBL properties

U_∞	$\overline{U} + \mu_{\overline{U}}$	$U^M_{DS}[table4.6]$	$\delta^* + \mu_{\delta^*}$	$\delta^*_{DS}[table4.6]$	$\theta + \mu_\theta$	$\theta_{DS}[table4.6]$
0.5	0.41+0.002	-	5.8+0.1	-	4.4+0.1	-
1.0	0.83+0.018	0.87	6.0+0.3	6.0	4.4+0.1	4.4
1.5	1.29+0.001	-	5.2+0.1	-	4.0+0.1	-
2.0	1.72+0.013	1.73	4.9+0.1	4.3	3.8+0.1	3.3
2.5	2.16+0.007	-	4.8+0.1	-	3.8+0.1	-
3.0	2.61+0.005	2.60	4.5+0.1	4.2	3.6+0.5	3.3
3.5	3.04+0.016	-	3.9+0.7	-	3.1+0.2	-
4.0	3.53+0.006	3.50	4.5+0.2	4.4	3.5+0.1	3.5

Table 4.9 shows the average results for measured velocities and their uncertainty, which were calculated by eq. 3.22. It also shows the results from table 4.6, except for U_∞ [0.5 1.5 2.5 3.5], which were not measured in section 4.4.1. For the velocities that can be compared good repeatability of the mean flow can be seen, which is consistent with earlier findings.
The δ^* and θ are somewhat larger compared to the original data. This slight increase is because the measurements are somewhat further downstream. The data itself shows good repeatability, except for U_∞ 1 and 3 $\frac{\text{m}}{\text{s}}$. A clear cause for this behaviour cannot be identified. Especially test 1 for $\overline{U} = 1.73\frac{\text{m}}{\text{s}}$ deviates greatly from the other tests, although an offset in the pressure sensors voltage is presumed to be the culprit for this specific case.

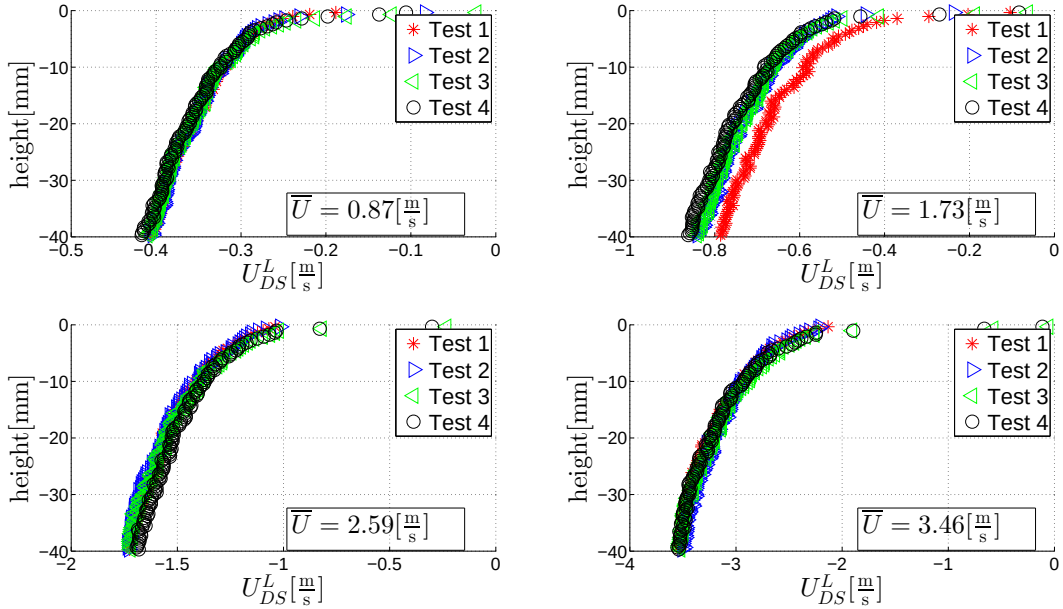

Figure 4.10: Velocity profiles for several tests at DS FOV

4.5 Log layer

Using the small FOV, the log layer was studied. Due to time limits, it was chosen to only perform measurements for $\overline{U}$=1.0 $\frac{\text{m}}{\text{s}}$ at the DS position. To estimate the physical dimension of the log layer, eq. 2.1 is rewritten:

$$\delta_v = \frac{\nu}{u_\tau} \longrightarrow \frac{\nu\rho^{\frac{1}{2}}}{\tau_{wall}^{\frac{1}{2}}} \tag{4.20}$$

which gives the wall unit δ_ν, which represents the physical size of $y^+ = 1$. Using eq. 2.4 to obtain an estimation for τ_{wall} gives that δ_ν=23.5 μm. Using fig. 4.11 which shows the small FOV it can be seen that the height of the visualised flow is approximately 4.5 mm. This means the number of wall units visualised is:

$$\frac{4500}{\delta_\nu} = 200 \tag{4.21}$$

hich is the region where the streamwise velocity can be normalized by the theory described in section 2.2.1.

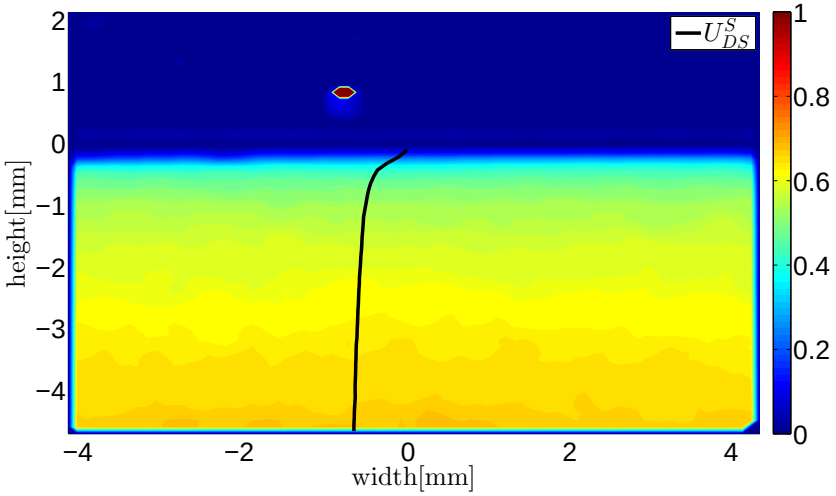

Figure 4.11: Velocity profile log layer

4.5.1 Mean flow

Streamwise velocity

Using the FOV of fig. 4.11 5 independent measurements were performed as showed in the left plot of fig. 4.12. The normalizing wall shear is determined by taking C_D from 4.5 and inserting into 4.14, which gives u^+. The right plot shows the mean and uncertainty of for these 5 measurements. This fig. also shows the u^+ according to the logarithmic law of eq. 2.1.

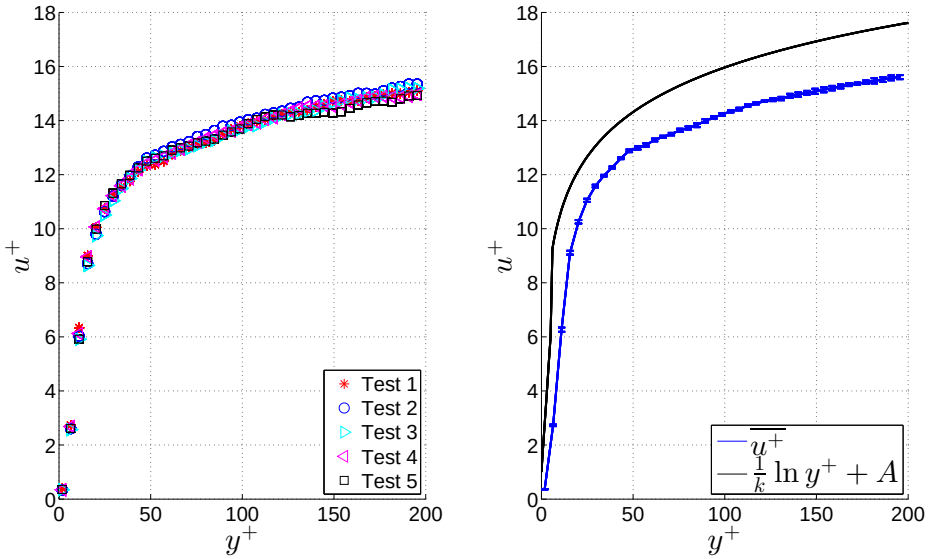

Figure 4.12: Left : u^+ for several tests
Right: $\overline{u^+}$ and the law of the wall

The results shown are well repeatable and display the logarithmic behaviour. The average wall shear stress determination gives an overestimation of the local wall shear stress, which explains why the curve is smaller compared to the logarithmic law.

Wall normal velocity

The data from which fig. 4.12 was calculated can also be used to construct the mean wall normal velocity. The results for the 5 independent test are given in the left plot of fig. 4.13, for which the same scaling of u^+ is used.

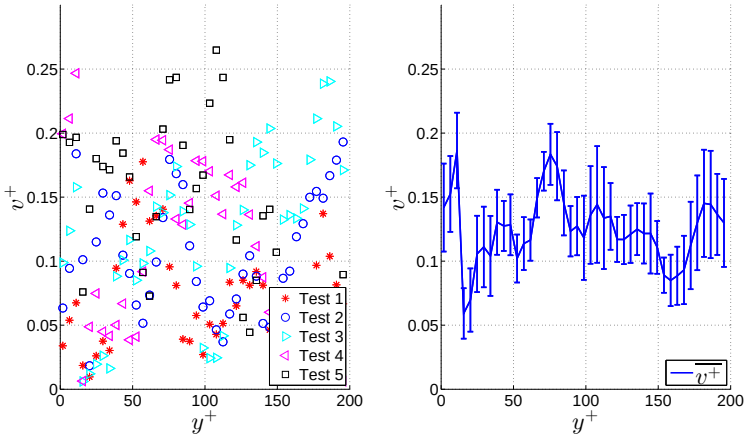

Figure 4.13: Left : v^+ for several tests
Right: $\overline{v^+}$

Analysing the results in the right plot shows that the uncertainty for v^+ is significantly larger compared to u^+. This is an inherent feature of the PIV system which is optimized for particle displacement in the streamwise direction. Because wall normal displacement is much less, the correlations between dot patterns becomes more difficult for the Davis system, resulting in larger uncertainty.

4.5.2 Reynolds stress

The FIK identity discussed in chapter 1 can be used to study the drag reducing performance of the riblets. The major contribution is made by the reynolds shear stress $\overline{u'v'}$, which can be computed by:

$$\overline{u'v'} = \overline{(u - \overline{u})\,(v - \overline{v})} \tag{4.22}$$

which uses both instanteneous and average values of the streamwise an wall normal velocity. When this value is computed for all 5 independent tests and averaged, it gives the result in fig. 4.14. It shows the reynolds shear stress cannot be determined from this data. Because v^+ has not yet converged, see fig .4.13, this is expected behaviour and more measurements N_{PIV} are needed. This was unfortunately not possible in the scope of the project due to time restrictions.

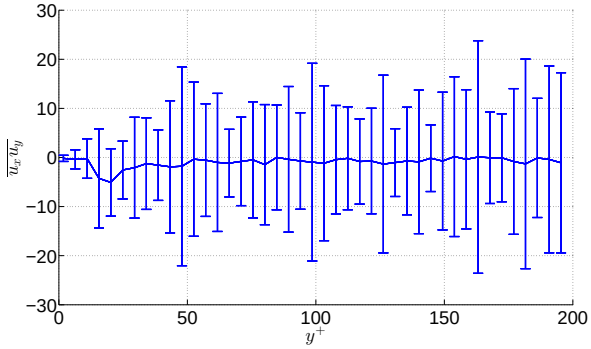

Figure 4.14: Reynolds shear stress

4.6 Conclusions on PIV measurements

While research objective 1 was achieved in the former chapter, some questions regarding the flow remained open. The most significant of these was the actual value of the freestream velocity magnitude. Using PIV, Measurements of the freestream velocity confirmed the bias of the pressure sensor, which was also measured by the Pitot tubes. On average the velocity in the test section is 86.5% less than measured in the contraction. Measuring at several positions downstream also showed a small pressure gradients exist over the test section, although its effect on riblet performance is neglible according to Boomsma and Sotiropoulos [2015].
In addition to the freestream, a medium sized FOV was used to study the TBL. Calculation of the shape factor showed the boundary layer is indeed turbulent over the entire test plate, which is important since riblets only reduce drag for turbulent flow. Fitting the displacement thickness to theory showed the boundary layer origin shifts upstream with increasing velocity. Although this gives an explanation why the measured C_D is smaller compared to literature, more measurements are needed to make corrections for this effect.
Using a small sized FOV the near wall velocity was measured. The streamwise component is well repeatable and scales logarithmically, although estimates of the local wall shear stress are required to match the theory. The wall-normal component displays larger uncertainty, which is inherent to the PIV systems design. This also affects the Reynolds shear stress measurement, which requires a larger number of frames to statistically converge.

Similar to chapter 4, the most important findings are listed below. This is done according to the used FOV.
Freestream velocity

- The freestream velocity in the test section is on average 13.5% smaller than the contraction velocity
- A small pressure gradient exists in the test section. Evaluating it with Clausers parameter showed it's very small and should not affect riblet performance according to Boomsma and Sotiropoulos [2015]

Boundary layer flow

- Comparing the freestream velocity profile and magnitude for the medium and large frame shows that the freestream is well repeatable
- Determination of the shape factor shows the flow is turbulent over the entire test plate
- Least square fitting the displacement thickness to theory show the TBL originates before the plate's leading edge

Log layer

- The wall streamwise velocity scales logarithmically and is well repeatable
- The reynolds shear stress cannot be determined because of large uncertainties. This is caused by the unconverged data for the wall normal velocity, which can be solved by taking more consecutive snapshots

Chapter 5

Drag Measurements

This chapter describes the results of the 3 different coatings that were measured. These were supplied by Océ and Fraunhofer IFAM. This chapter comprises of two sections, treating the coatings by supplier. The coating delivered by Océ is an elevated printed riblet with spacing O(400μm), based on Becherts design. The Fraunhofer IFAM coatings consists of two classes, stiff and intersleek riblets. Both are geometrically similar to OCE, albeit with smaller spacing O(100μm). The intersleek class additionally possesses compliant and hydrophobic characteristics, meaning it deforms with the fluid motion and is water repellent. Each section consists of a description of the measured coatings, followed by the results and discussion, which are summarized in the conclusion.

5.1 OCE

5.1.1 Description of the coatings

The elevated printed coating manufactured by Océ was printed on a smooth bicoating plate. Fig. 5.1 shows the printed riblet plate and the white bicoating plate, which was used as a smooth reference plate.. Due to being classified, the scanning electron microscope [SEM] pictures are not presented in this chapter, but in Appendix F.
These show flow alligned riblets with spacing 400μm, with cross section most closely corresponding to the trapezoidal riblets of Bechert et al. [1997], see fig. 2.5. Another important feature are the rounded riblet tips, which are caused by the printing method. According to Bechert et al. [1997], this has a deteriorating effect on the performance.
Knowing the optimum of these riblets is for $s^+ = 17$, equations 3.20 and 3.18 can be used to determine the expected optimum velocity. First the wall shear stress is integrated over the entire test plate:

$$\overline{\tau_{wall}} = \frac{1}{L}\int_0^L 0.0135 * (\rho\nu)^{\frac{1}{7}} \rho^{\frac{6}{7}} \overline{U}^{\frac{13}{7}} x^{-\frac{1}{7}} \mathrm{dx} \tag{5.1}$$

which gives an average approximation. Using this value, the wall shear velocity can be calculated, which is used to calculate s^+. For $s = 400\mu m$, the optimal performance of the riblets is around $\overline{U} = 1\frac{\mathrm{m}}{\mathrm{s}}$.

Figure 5.1: Riblet and bicoating plate OCE

5.1.2 Results and discussion

Fig. 5.2 shows the result for the smooth bicoating and riblet coating of fig. 5.1. For both plates, 5 independent measurements were performed resulting in the two upper figures. These raw data plots are then interpolated and averaged, resulting in the lower two figs. These shows that μ_{C_D} for both plates is very good and remains within the drawn 1% interval for $Re_L(\overline{U}) \geq 2 \times 10^6$. For lower $Re_L(\overline{U})$, μ_{C_D} becomes larger which was also analysed in chapter 3 for the smooth plate.

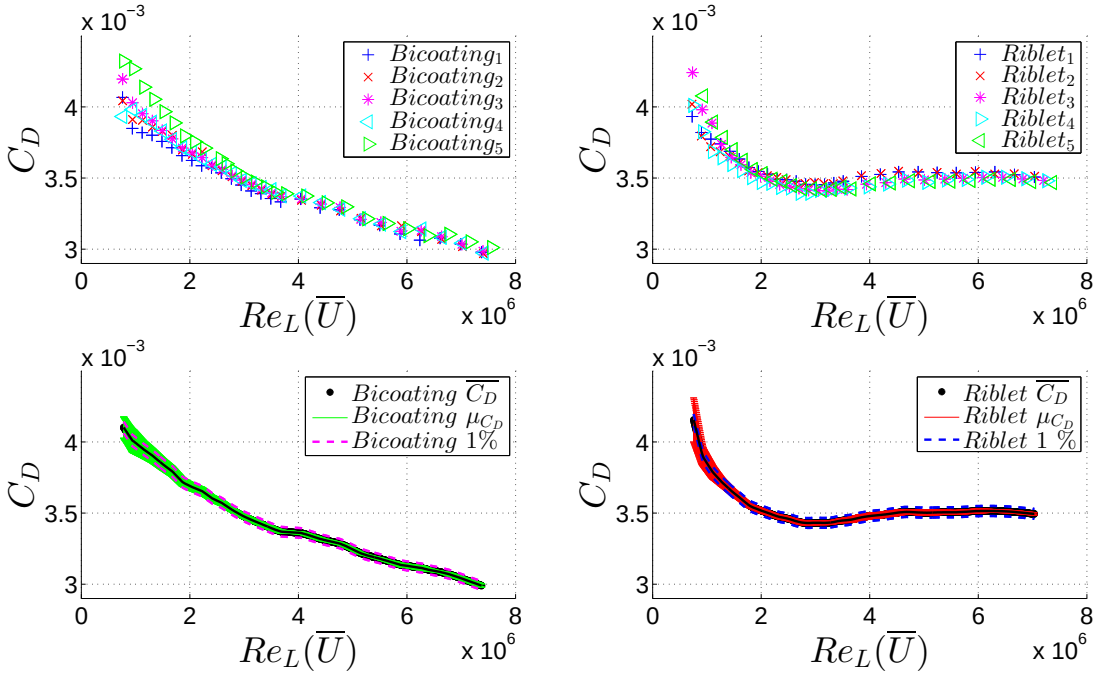

Figure 5.2: Top : Measurement results for the smooth and riblet plate OCE
Bottom: C_D and μ_{C_D} for both plates based on the interpolated data

Plotting the bottom results of fig. 5.2 together in fig. 5.3 shows that C_D for the riblet plate is lower for certain $Re_L(\overline{U})$, meaning it reduced the drag. This figure also shows the reproducibility regime in green, which was taken from fig. 3.28. Using equations 3.18 and 3.17, the data from the left plot is converted to s^+, and DC respectively in the right plot. It can be seen that the coating reduces the drag for max 5%. This compares well to Bechert et al. [1997], from which data for two comparable riblet coatings have been plotted,

Firstly the shape of the DC curve matches well, showing an optimum around $s^+ = 17$. Unfortunately this optimum lies within the region where reproducibility is less, although the smooth bicoating plate should be analysed for reproducibility as was done in section 3.4.6. Although further analysis on the bicoating plate is required, its C_D seems better reproducible as it does display a monotonous decrease with $Re_L(\overline{U})$ which was not found for the smooth plate, see fig. 3.28.
Secondly the order of DC is comparable, albeit 2% lower than Bechert et al. [1997]. This difference is the presumed result of the rounded riblet tips, see appendix F.

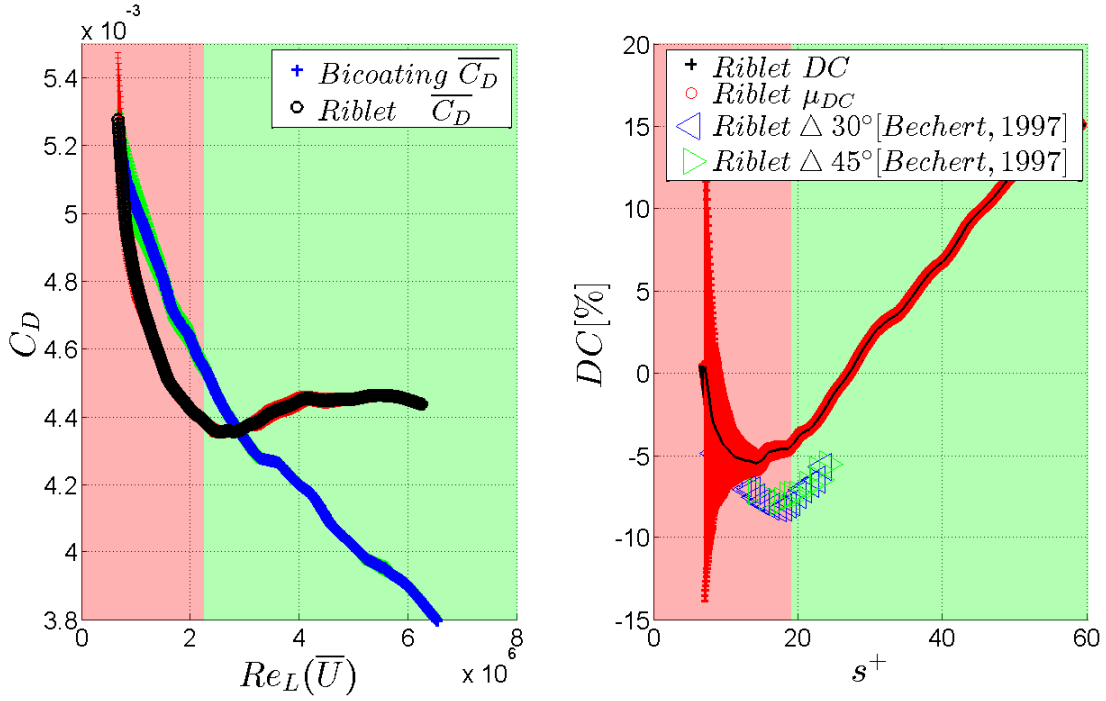

Figure 5.3: Left : C_D for smooth and riblet plate Océ
Right: DC for riblet plate Océ compared to smooth

5.1.3 Conclusions on Océ riblets

- Repeatability and accuracy compare well for both bicoating and riblet plate with results from chapter 3
- Océ riblets compare well to literature and are able to reduce the drag up to 5%
- The O(2%) less performance is presumably caused by the inkjet production effects on the riblet tips, such as the rounding of the riblet tips and the sharpness of the riblet contours

5.2 Fraunhofer IFAM

5.2.1 Description of the coatings

The coatings provided by Fraunhofer IFAM are also based on the Bechert design but with smaller spacing, $s = 100\mu m$. The 4 test plates can be divided into 2 classes: stiff and intersleek [IS].
The stiff class consists of two plates which are constructed using a moulding technique. By means of a negative mould, see fig. 5.4 a riblet pattern with trapezoidal geometry is pressed. These riblets are then cured with ultraviolet [UV] light. For more details, see the work of Boyer et al. [2011]. Both stiff plates are expected to have similar drag reducing property.

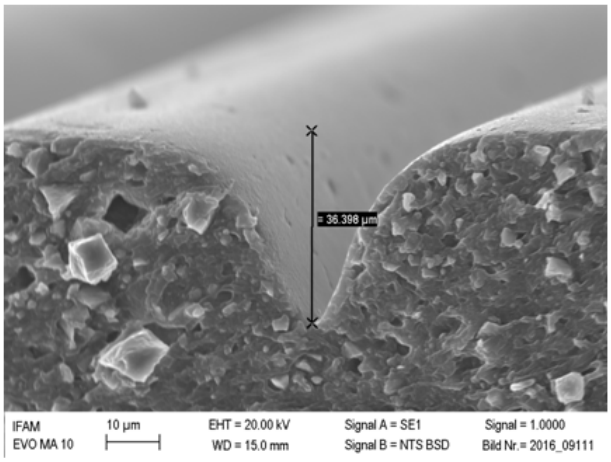

Figure 5.4: Negative cast of the manufactured coating [Fraunhofer]

The IS class consists of two plates treated with a three-pack chemically cured paint, which is used for spraying. Due to difficulties with moulding, this mixture was modified and treated such that the resulting spray could be mould pressed. An impression of these riblets can be seen in fig. 5.5 , which shows an aerial and cross-sectional view.

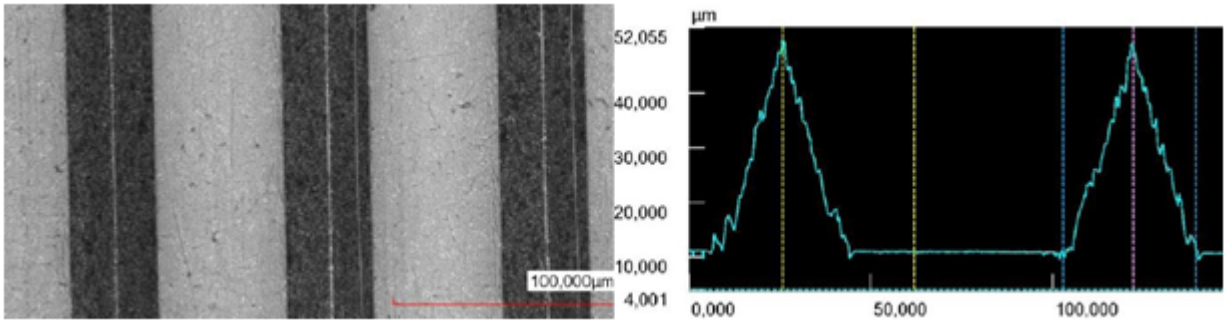

Figure 5.5: Left : Microscopic image of IS riblets displaying s
Right: Cross-section of IS riblets

From these pictures it can be seen that the sharpness of the riblets tips and the geometry are of good quality. This was also reported for the stiff riblet class. Applying the riblets to the test plates however, proved to be of some difficulty due to adhesion to the mould. For all tested plates, small visual defects are visible which can deteriorate the drag reducing properties.

5.2.2 Results and discussion

Using eq. 5.1 and the analysis from the former section, the optimum performance for the Fraunhofer riblets is expected at $\overline{U}$=4$\frac{\text{m}}{\text{s}}$. Because this velocity can not be obtained in the test section, it is expected the optimum of the DC curve will be hard to identify.
Higher velocities are limited by air bubble formation, which are entrained into the test section. During a private conversation with R. Delfos and A. Greidanus it was pointed out this could be circumvented using a vacuum pump. Using this device, operational velocity can be raised to $\overline{U}$=5.5$\frac{\text{m}}{\text{s}}$, allowing further study of the DC curve.
Because these tests were performed in a later stage, thorough analysis of the system including the vacuum pump could not be made. It is assumed that repeatability and reproducibility properties from the lower velocity regime are also valid for this system.

This section consists of two parts. The first treats the velocity measurements without the vacuum pump up to $\overline{U}$=3.7$\frac{\text{m}}{\text{s}}$. The second treats the measurements with the vacuum pump, which operates for $3.5 \leq \overline{U} \leq 5.5\frac{\text{m}}{\text{s}}$.

Low velocity

Fig. 5.6 shows the low velocity results for two Fraunhofer plates, where $Stiff^1$ and IS^1 corresponds to the first stiff and intersleek riblet coating respectively. These coatings were measured for 5 independent times for $2.0 \leq \overline{U} \leq 3.7\frac{\text{m}}{\text{s}}$, where the subscript corresponds to the measurement.
Interpolating gives the result of the bottom plots. It can be seen that uncertainty is small for both plates, and well within the 1% interval. The only measurement that stands out is $Stiff_1^1$, which deviates heavily from the other measurements. Although no clear explanation for this behaviour can be determined, it is assumed it is incorrect and not included in constructing the mean in the bottom fig.

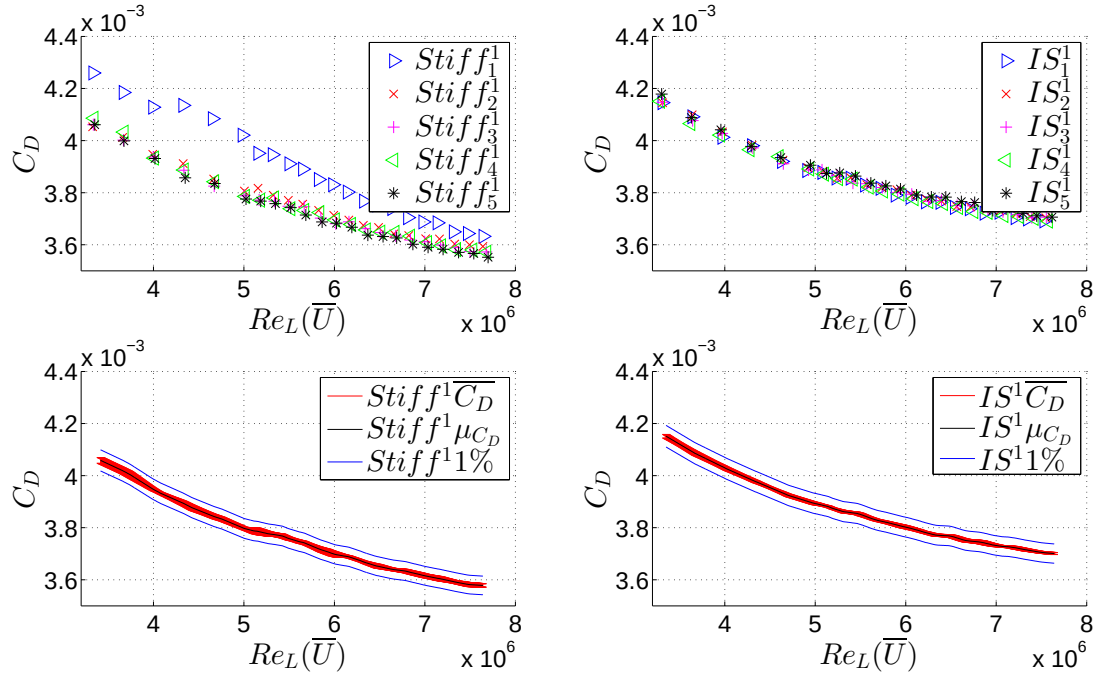

Figure 5.6: Top : Measurement results for the stiff and IS riblet plate Fraunhofer
Bottom: C_D and μ_{C_D} for both plates based on the interpolated data

Fig. 5.7 shows the interpolated data from fig. 5.6 and the smooth plate from chapter 3. Note that all data lies within the reproducible region $Re \geq 2.1 \times 10^6$. The right figure also show that both coatings reduce drag, although the IS coating significantly less.
This is quantified in the right plot, which gives the DC for the first stiff and intersleek riblet coating. It also shows that the expected optimum $s^+ = 17$ is not reached, in contrast to the estimate made by eq. 5.1. This estimate is based on the TBL originating at the plate's leading edge, which as shown in chapter 4 is not valid. The average wall shear stress and thus s^+ will be lower.

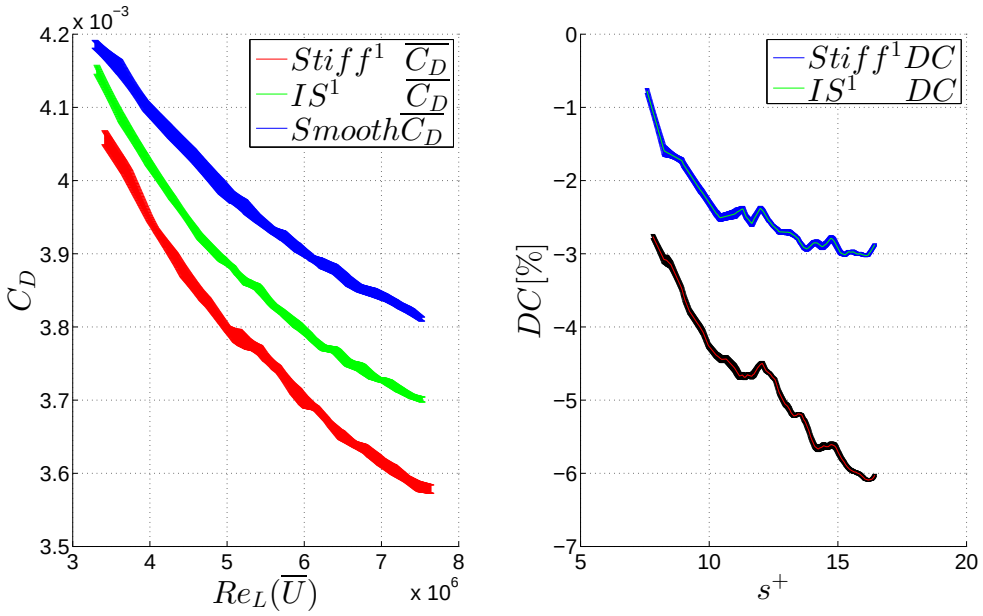

Figure 5.7: Top : Measurement results for the stiff and IS riblet plate
Bottom: C_D and μ_{C_D} for both plates based on the interpolated data

Tests at high velocities

Using the vacuum pump, the measuring regime was extended. First the original plate of the former measurements was remeasured for comparison. Because of the limited time left in this thesis project, the second plate of both classes was only measured once.
Fig. 5.8 shows the 3 independent measurements for the first plate and the measurement of the second plate for both classes. All data show good repeatability and reproducibility except $Stiff_1^1$. Again, no clear reason for this behaviour can be determined and it is assumed incorrect and not used to construct the average and uncertainty.
This remaining measurements of the stiff riblets vary heavily for $Re = 7 \times 10^6$, which is caused by heavy vibrations of the vacuum pump. These do no seem to affect the IS class as strongly. Both figures show that the second plate of both riblet classes performs slightly better, as their C_D is lower.

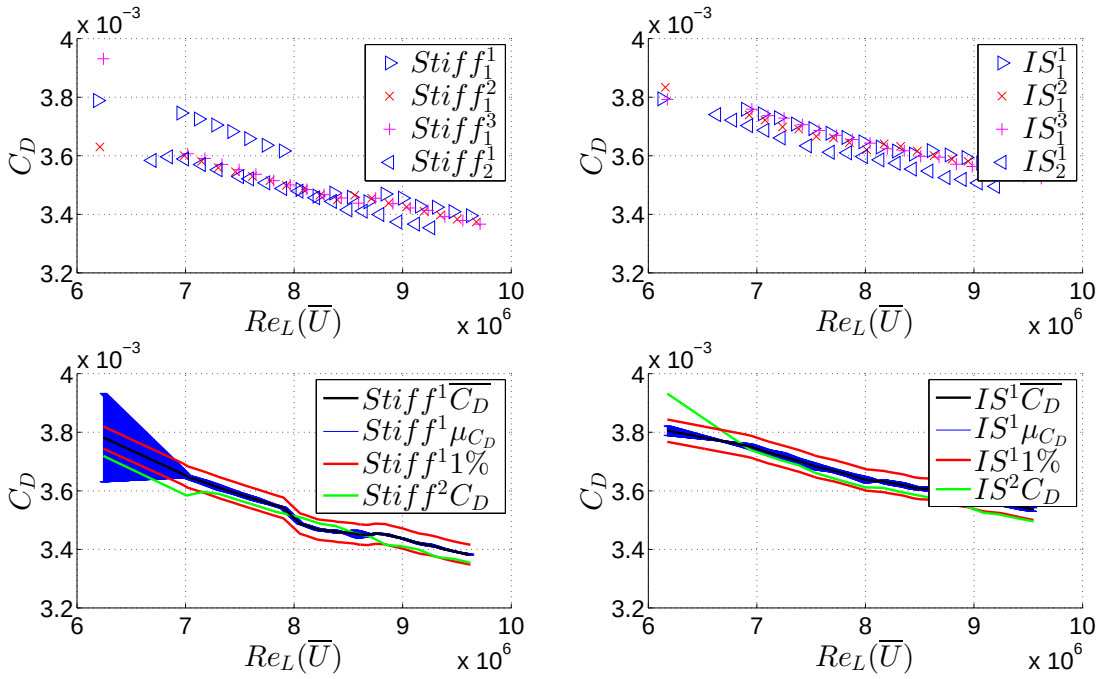

Figure 5.8: Top : Measurement results for the stiff and IS riblet plates Fraunhofer
Bottom: C_D and μ_{C_D} for the 4 plates based on the interpolated data

Plotting these results together in fig. 5.9 with the data from fig. 5.7 shows that the curves for the smooth, stiff and IS plates do not exactly overlap. Using the vacuum pump seems to affect the drag behaviour such that a steeper drop in C_D for all plates can be seen.

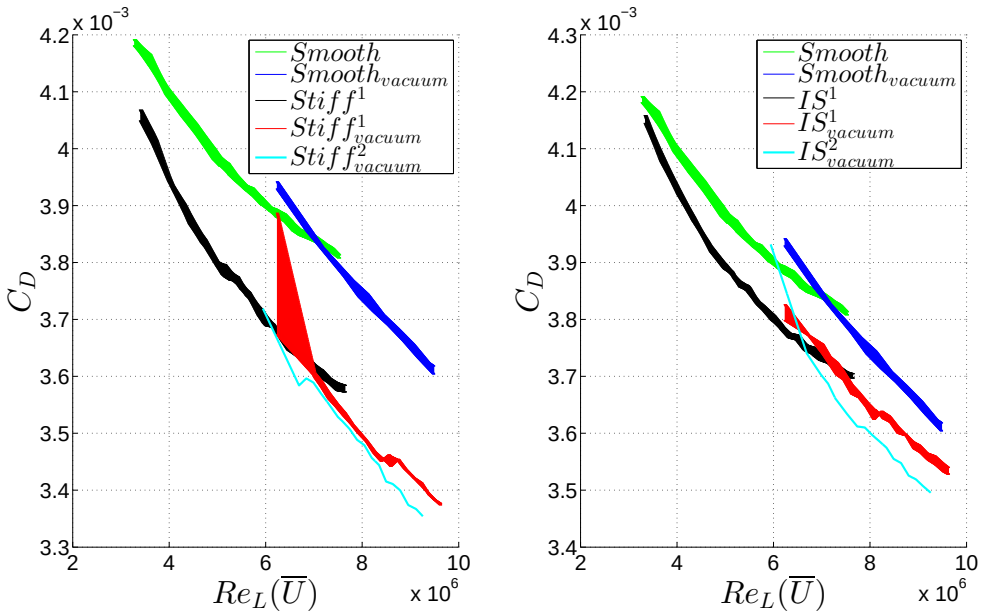

Figure 5.9: Left : C_D for stiff plate for low and high velocity tests
Right: C_D for the IS plate for low and high velocity tests

Computing s^+ and the corresponding DC for the new data in fig. 5.10 shows that the drag curves are less affected by this behaviour. For both the stiff and intersleek class the overlap is quite good. For the IS class the optimum is now more clearly visible around $s^+ = 17$. Both measurements show that the second plate gives a better performance than the first of their class, by DC O(2%). The visible defects and unknown production variation can be the cause for this, although more tests should be performed to confirm this.

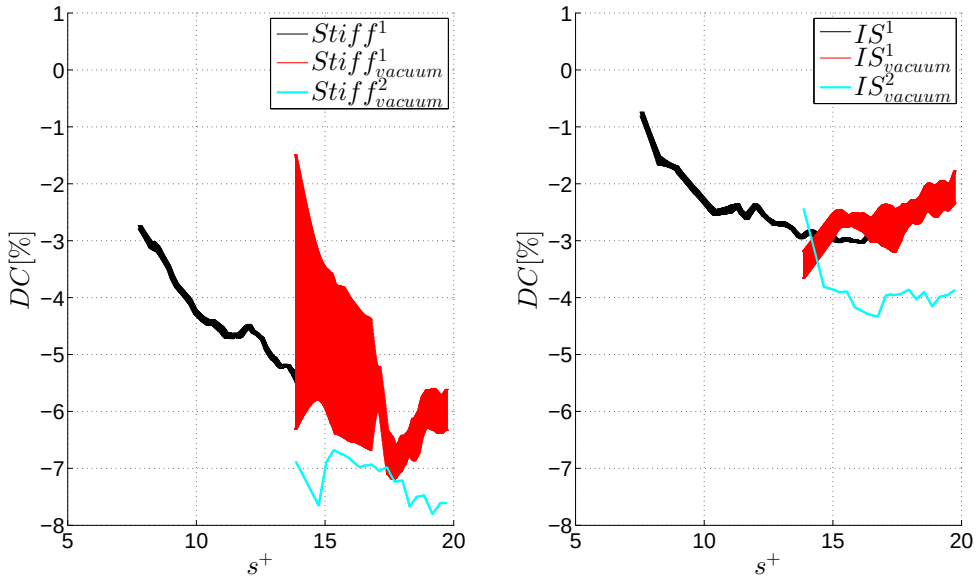

Figure 5.10: Left : DC for stiff plate for low and high velocity tests
Right: DC for the IS plate for low and high velocity tests

5.2.3 Conclusions on Fraunhofer IFAM riblets

Low velocity

- The measurements for the stiff and intersleek coating show good repeatability and accuracy within 1%
- The regular setup cannot visualize the optimum of $s^+ = 17$ because of velocity limitations
- The stiff riblets give comparable drag reduction compared to Becherts riblets
- The intersleek riblets are able to reduce drag, but significantly less compared to literature

High velocity

- Vacuum operating conditions change the shape of the drag curve
- The vacuum operated system allows the study of the optimum riblet performance at s^+=17, which is most clear for the intersleek riblets
- All 4 Fraunhofer IFAM plates are able to reduce drag. The stiff riblet class gives a significant better performance of 4-7 % compared to the intersleek class which remains at 3-4 %
- A single measurement of the second plate of both classes indicate both perform slightly better than the first plate

Chapter 6

Conclusions and recommendations

This chapter summarizes all conclusion from chapters 3-5 and connects them with the posed research questions from chapter 1. Rather than give a complete recap, the key findings which are most significant are highlighted.
The chapter ends with several recommendations, which can be categorized as either suggestions for improvement or new aspects for further research. Both categories are ordered by priority, which will be explained as well.

6.1 First objective

1. Develop an accurate drag plate measurement procedure that allows 1% precise drag reduction studie at the TU Delft cavitation tunnel

This objective was achieved using the propagation of uncertainty. Analysis of the temperature, drag force and pressure sensor showed the latter two require the longest measuring time to obtain statistically converged results of C_D. Application of a derived measuring time scheme produced results that are repeatable within O(1%) for freestream velocities greater than 1 $\frac{\mathrm{m}}{\mathrm{s}}$. These results were also reproduced by another experimenter for slightly varying measuring conditions, proving the robustness of the procedure. The measured value of C_D for a smooth reference surface is smaller compared to literature, which indicates the system is affected by several bias effects. Two significant effects that were investigated using PIV are the freestream velocity magnitude and the origin of the TBL.
Measurement of the former at 3 positions along the streamwise coordinate showed the freestream velocity is on average O(13.5%) smaller than the value measured by the pressure sensor. Determination of the boundary layer thickness at the same positions and fitting of a one-seventh powerlaw showed the TBL originates before the leading edge of the drag plate.

6.2 Second objective

2. Measure and analyse the drag reduction from the Fraunhofer IFAM and Océ plates, using the developed measurement procedure in this work

This objective was achieved using the procedure from objective 1. Drag reduction measurements show all plates from Fraunhofer IFAM and Océ are able to reduce drag. The maximum drag reduction for Fraunhofer was from the stiff riblet plate and is 7%. The maximum drag reduction measured for the Océ plate is 5%.
Both these optimums lie at the upper and lower limit respectively, where accurate drag reduction measurements are possible. For the Océ riblets at low velocity, this can be improved by using more accurate small range force and pressure sensors. Additional investigation into the reproducibility is also required, as this limits the reliability of the results.
For the Fraunhofer IFAM riblets higher values of the freestream velocity are needed to visualise the optimum. Although this is possible using a vacuum pump, using this device also changes the drag curve.

6.3 Recommendations

This section gives several recommendations, which can be used as a starting point for new studies. These are divided into 2 categories: (1)improvements for the current work and (2) suggestions for further research. Both are numbered, which indicates the priority for (1) and the effort required for (2).

Improvement to current work

1. The high velocity measurements from section 5.3.2. need further study, as the C_D curves do not match with the low velocity measurements. Repeating outer flow and TBL measurements with PIV from chapter 4 is necessary for comparison. Additional analysis of the vacuum system is necessary as well.

2. Perform additional measurements for the second plate of both Fraunhofer IFAM classes, to validate the difference between both plates

3. Improving the repeatability and reproducibility for low Re_L can help visualize the optimal performance of the Océ riblets. This can be done by using small range force and pressure sensor and analysing the plate alligning influences on F_D

4. The flush mount plate from 3.4.5 needs to be measured again, with extra care taken to prevent the sticking motion caused by the guidance strips

5. Repeating the medium FOV measurements and studying more positions is needed to understand the development of the TBL

6. More measurements with longer t_m are required to obtain converged data for the wall normal velocity and the Reynolds shear stress

Suggestions for further research

1. Mounting and alligning the test plate to the flow is very time consuming. Designing a device that automatically alligns the plate saves measuring time and helps improving the alligning accuracy

2. Using tomographic PIV to study the cross flow can give insight into side wall flow effects. It can also be used as a stepping stone to study the flow over the riblets when smaller FOV are used

3. Using smaller vector spacing, $\frac{\mathrm{d}\delta^*}{\mathrm{d}x}$ and $\frac{\mathrm{d}\theta}{\mathrm{d}x}$ can be evaluated. These can then be used to study the TBL growth and the skin friction coefficient respectively

4. Once converged $\overline{u'v'}$ is measured, the FIK identity can be used to in-depth study the drag reduce of the coatings

5. The meshing program in Appendix C was designed to generate conventional and herringbone riblets. Because the initial proposition of performing a parameter study into the latter was not possible, due to manufacturing restrictions, it can still be used in future work to design specific riblets. These mapped surfaces can then be given to manufacturer for production

Appendices

Appendix A

Pitot tube results

Prior to the PIV measurements, several velocity measurements with Pitot tubes were performed. Inconclusive results between the used tubes and with the PIV data was the major reason these results were moved to this Appendix.
This chapter start by describing the measuring principle and used measuring positions. First the mean flow was measured at the test sections center at upstream and downstream position, using both tubes. Using the smaller tube, an investigation into the TBL velocity profile was made at the downstream position. Using these results the displacement and momentum thickness were determined.
Unfortunately, freestream velocities between both tubes showed inconsistent results. In addition, the shape factor measured by the small tube the presence of a very strong pressure gradient, which was not measured in the freestream. Based on these findings all Pitot tube results were deemed insufficient to make accurate flow prediction.

A.1 Principle and measuring positions

A pitot tube is a hollow pipe with its circumference placed perpendicular to the flow. Because the fluid inside the tube is a closed system, the flow stalls and builds up pressure. This pressure can be converted to the entering velocity using eq. 3.1

$$P = \frac{1}{2}\rho U^2 \tag{3.1}$$

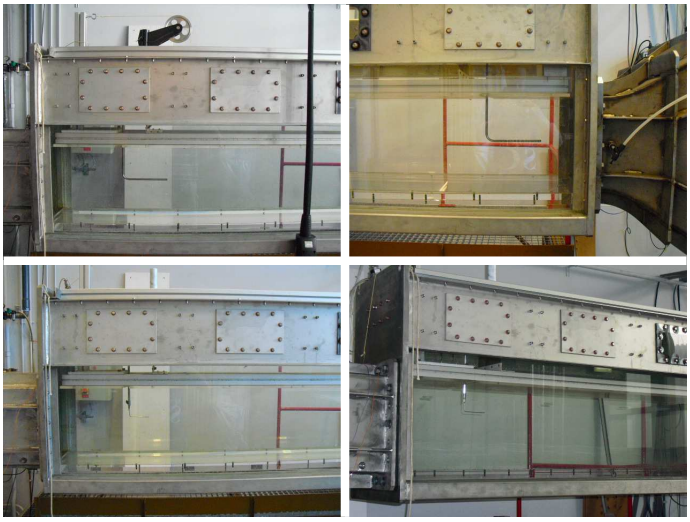

Figure A.1: Up : Large tube at front and back of the tunnel section
Down: Small tube at back for two different height configurations

Two different Pitot tubes were used, which were already shown section 3.4.5. Fig. A.1 shows the positions and the configurations of the used tubes. The large tube was placed at the center line near the leading edge and end of the test plate. This allows the study of the freestream velocity and possible pressure gradient.
The smaller tube was placed at the end of test plate in two configurations. First the freestream velocity was measured as a comparison to the large tube. Secondly the TBL was analysed by translating the pitot tube along the wall-normal coordinate.

A.2 Results

A.2.1 Freestream velocity

Fig. A.2 shows the results for the large Pitot tube at the front and back. Similar to the velocity deficit in section 4.3.1. the difference between test section and contraction exit velocity is given as a percentage. Both tubes performed 3 independent measurements over the interval $0..4 \leq U_\infty \leq 4[\frac{\mathrm{m}}{\mathrm{s}}]$. Because of a connection problem, the fourth measurement at the back position was not registered, therefore only 3 measurements are displayed.

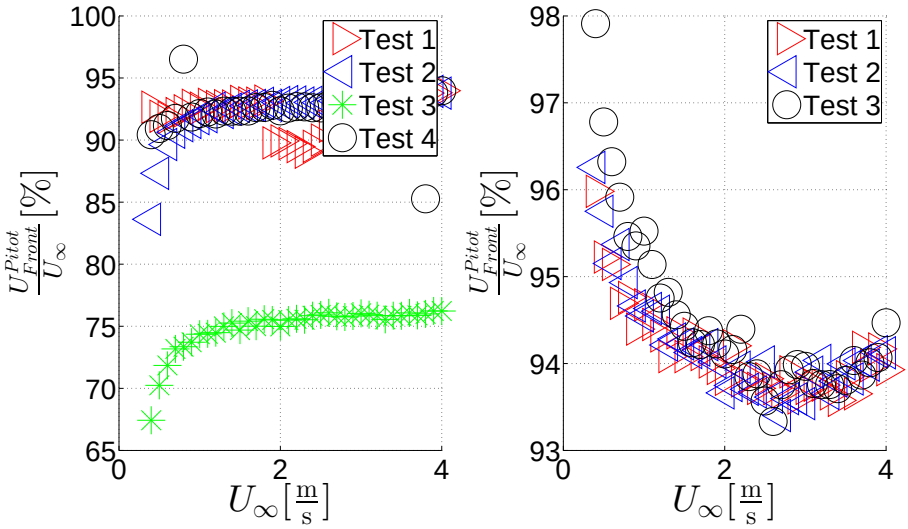

Figure A.2: Left : Large tube at front and back of the tunnel section
Right: Small tube at back for two different height configurations

Both figures show a significant velocity deficit exists between for both positions. This deficit decreases with increased downstream position, which was also measured with PIV. Test 3 for the front plate shows very different results compared to the other tests. Investigation showed this was a result of a wrongly calibrated pressure sensor.
All results show reasonable repeatability, with uncertainty averaging 1%. The trend observed in the left plot corresponds qualitatively to the findings of the PIV system. Both figures however, show a deficit that is much smaller. To analyse this behaviour. The small pitot tube was placed at the back position to measure the mean flow, yielding the result in fig. A.3.

This fig. shows that the results between both tubes do not overlap. Exact reasons for this could not be determined.

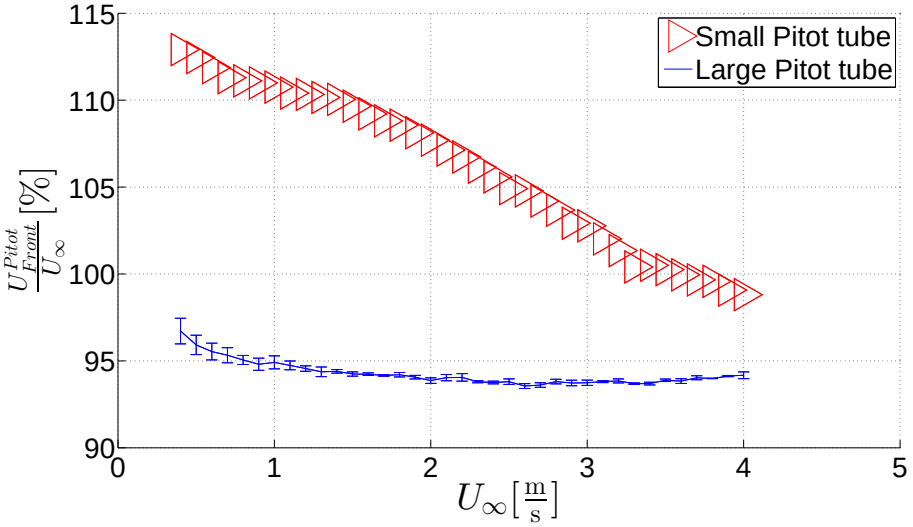

Figure A.3: Left : Large tube at front plate position
Right: Large tube at back plate position

A.2.2 Boundary layer

Using the small tube the boundary layer was analysed as well. Fig. A.4 shows the results of 5 independent measurements with the small pitot tube. By translating the tube with increments of 0.2 mm the near wall velocity profile was reconstructed.
Although results show good repeatability, the boundary layer velocity profile is not continuous. This behaviour is unexpected and could not be clarified. When the shapefactor for the mean profile was calculated it yielded the result of 0.15, which would correspond to a very strong pressure gradient. With regard to its inconclusive result with the large pitot tube, this result was deemed incorrect.

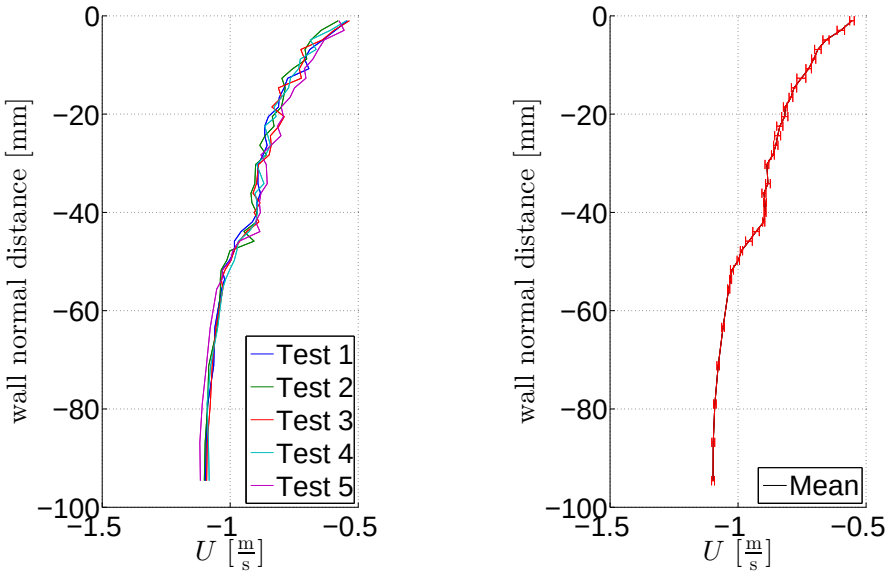

Figure A.4: Left : TBL test for the small pitot tube
Right: Mean and uncertainty of the TBL measurements

Appendix B

Matlab codes

B.1 Data processing code

```
% This m-file loads and plots the data from the similar named test.
clear all
close all
clc
% Names of tests
testrun={'_f1';'_f2' ;'_f3' ;'_f4';'_f5'};              % Test numbers

% Parameters
path='C:/Users/documents/measurements/smooth';
A=2*0.298;                                              % surface flat plate [m]
alpha=2.07e-4;                                          % expansion coefficient water [1/T]
po=998.2071;                                            % reference density water [kg/m^3]
L1=0.735;                                               % entrance contraction
L2=0.3;                                                 % exit contraction

% Preallocated vectors
U=0.4:0.2:4;                                            % measuring range [m/s]
Cd=zeros(length(U),length(testrun));                    % preallocate drag coefficient
Force=Cd;                                               % preallocate drag force
Temperature=Cd;                                         % preallocate temperature
Rel=zeros(length(U),1);                                 % preallocate Rel
Velocity=Cd;                                            % preallocate velocity
for j=1:length(testrun)
   %% Zeros
        zero=strcat(path,'Zero',testrun(j),'.dat');     % zero output load cell
        zero=load(zero{1});
        zero=mean(zero(:,14));                          % zero measurement
        zero(j)=zero;                                   % store zero
   %% Velocity
        for i=1:length(U)
        number=U(i)*10;                                 % velocity index
        if number<10
            number=['0' num2str(number)];               % velocity lower than 1 m/s
        else
            number=num2str(number);                     % velocity higher than 1/ms
        end
    %% Load data
        name=strcat(path,'U_',number,testrun(j),'.dat');% specify file
        M=load(name{1});                                % load test_data
        M=[mean(M(:,8)) mean(M(:,9)) mean(M(:,14))];    % obtain mean temperature, pressure and force
    %% Temperature and Viscosity
        T(i,j)=M(1);                                    % temperature
        rho=po/(1+alpha*(M(1)-20));                     % density
        mu=2.414e-5*10^(247.8/((M(1)+273)-140));        % kinematic viscosity
        nu=mu/rho;                                      % dynamic viscosity
        Vuncor=sqrt(2*M(2)/(rho*(1-(L2/L1)^4)));        % biased velocity measurements
```

```
        % Velocity correction
        Velocity(i,j)=Vuncor(i);                          % velocity with PIV correction
%         Velocity(i,j)=U(i);
        Rel(i,j)=Velocity(i,j)*2/nu;                      % Reynolds number
    %% Fd and Cd
        Force(i,j)=M(3)-zero;                             % force
        Cd(i,j)=2*(M(3)-zero)/(po*(Velocity(i,j)^2)*A); % drag coefficient
    end
    progress=j*100/length(testrun)                        % number of tests processed
end
%% Interpolate data
xmin=max(Rel(1,:));                                       % maximum of the smallest measured Reynolds number
xmax=min(Rel(end,:));                                     % minimum of the largest measured Reynolds number
xinterp=xmin:1e4:xmax;                                    % interpolation interval which is smaller than any bou
% Linear interpolation
Cdinterp=interp1(Rel,Cd,xinterp);                         % interpolation the data

%% Plot data
% Raw
figure(1)
subplot(2,2,1)
hold on
plot(Rel,Cd)                                              % plot raw data
plot(mean(Rel,2),0.031./(mean(Rel,2).^(1/7)),'k')         % plot theoretic reference from White
xlabel(['Reynolds number'])
ylabel(['Cd'])
% Interpolated
plot(xinterp,Cdinterp)                                    % plot interpolated data
plot(xinterp,0.031./(xinterp.^(1/7)),'k')                 % plot theoretic reference from White
xlabel(['Reynolds number'])
ylabel(['Cd'])

%% Save data
save('Rel','Rel')
save('Cd','Cd')
save('T','Temperature')
```

B.2 Riblet meshing programme

```
%% This file produces the mapping needed for defining the structure.
% It does this by defining the mapping f(x,y) to construct one half feather
% structure and mirroring this structure until the full plate width is
% reached
% This model is for scalloped riblets with linear varying height
% last updated 13-01-2016
clear all
close all
clc

%% Parameters that may be changed
% Plate
L=1e-1;                         % length of the plate [m]
W=L;                            % width of the plate [m]
% Riblet
theta=40;                       % yaw angle [must be chosen 0<j<90], though 89 gives errors as well
gamma=20;                       % riblet angle
h=400e-6;                       % riblet height @ centerline [m]
s=400e-6;                       % riblet spacing [m]
Nr=10;                          % number of elements in spanwise cut

%% discretization
% Note that dy cannot be given. This is because it's a function of dx and
% theta. This ensures the grid can plot the angle theta

% Derived geometric parameters that may not! be changed
sl=s/sind(theta);               % streamwise spacing
sn=sl*tand(theta);              % spanwise spacing
Wn=sn*Nr;                       % half width feather
Ll=sl*Nr;                       % streamwise length feather
Lf=sqrt(Wn^2+Ll^2);             % length feather
Wr=h*tand(gamma/2);             % riblet half width @ X=Wn
Wl=Wr/sind(theta);              % half width riblet streamwise @ X=Wn

%% Discretization input that may be changed
dx=Wn/20;                       % spacing x based of feather halfwidth
factor=20;                      % number of dy s.t: atan(dx/(factor.dy))=theta

%% Obtain and plot 1 riblet
[CorX,CorY,Z,Wn,Ll,nsr,N,error_s]=riblet_v1(theta,gamma,h,s,Nr,dx,factor);
figure(2)
hold on
surf(CorX,CorY,Z)               % plot structure
[size1,size2]=size(CorX);       % parameters needed to translate half riblet
surf(-CorX+2*CorX(end,end)*ones(size1,size2),CorY,Z)
axis equal

%% Make structure that can be copied
CcorX=zeros(1+2*nsr,1);         % preallocating
CcorY=CcorX;                    % "         "
Zcor=CcorX;                     % "         "
for i=1:size2;
    CcorX=[CcorX CorX(1:2*nsr+1,i)];
    blow=nsr+(i-1)*N-nsr+1;     % low boundary
    bup=nsr+(i-1)*N+nsr+1;      % upper boundary
    CcorY=[CcorY CorY(blow:bup,i)];
    Zcor=[Zcor Z(blow:bup,i)];
end
CcorX=CcorX(:,2:end);
CcorY=CcorY(:,2:end);
Zcor=Zcor(:,2:end);
% Plot cropped structure
figure(3)
surf(CcorX,CcorY,Zcor)
axis equal
```

```
%% Filling the plate
% Parameters for filling
Nx=W/Wn;                        % number of riblets in spanwise cut
Nxr=floor(Nx);                  % rounded "      "
Ny=L/(Ll+sl);                   % number of riblets in streamwise cut
Nyr=floor(Ny);                  % rounded "      "

% Plot length plate, note that edge effects are not (yet) included
[size1,size2]=size(CcorY);
for j=1:4
    if mod(j,2)==1
    CorX=CcorX+CcorX(1,end)*(j-1)*ones(size1,size2);
    else
    CorX=-CcorX+j*CcorX(1,end)*ones(size1,size2);
    end
    for i=1:Nyr
        figure(4)
        hold on
        mesh(CorX,CcorY+(i-1)*(CcorY(1,1)-CcorY(end,1))*ones(size1,size2),Zcor)
        axis equal
    end
end

%% Display message when riblet width is larger then spacing
if Wl>=sl/2
    display('Note that for chosen parameters the riblet width becomes greater than spacing s. Consider decreas
end


function [CorX,CorY,Z,Wn,Ll,nsr,N,error_s]=riblet_v1(theta,gamma,h,s,Nr,dx,factor)
% This function uses the parameters given by the users to construct 1
% riblet. The output will be the meshgrid of the riblet and a meshplot of
% the surface

%% Derived geometric parameters
sl=s/sind(theta);               % streamwise spacing
sn=sl*tand(theta);              % spanwise spacing

Wn=sn*Nr;                       % half width feather
Ll=sl*Nr;                       % streamwise length feather
Lf=sqrt(Wn^2+Ll^2);             % length feather

Wr=h*tand(gamma/2);             % riblet width @ X=Wn
Wl=Wr/sind(theta);              % width riblet streamwise @ X=Wn

%% Coordinates and discretization
dymin=dx/tand(theta);           % minimal spacing to plot yaw angle
dy=dymin/factor;                % spacing y

N=dx/tand(theta)/dy;            % number of steps in y needed to mimic angle theta
Nr=floor(N);                    % number of steps in y needed to mimic angle theta

x=0:dx:Wn;                      % coordinates x
y=0:-dy:(-Lf-Wl);               % coordinates y
[CorX,CorY]=meshgrid(x,y);      % meshgrid X and Y
Z=zeros(length(CorY),length(x));% height matrix

%% Filling algorithm
for i=2:length(x)               % point (x,y)=[0,0] is already known
    j=(i-1)*Nr;                 % coordinate y

    % Values of centerline
    yexp=x(i)*-Ll/Wn;           % value of y corresponding to y
    hmax=h/Wn*x(i);             % centerline height
    Wlb=Wl/Wn*x(i);             % bandwidth

    % Center point
    Z(j,i)=hmax;                % since central point is at centerline
```

```
    % Values of bandwidth

    if j>1;                     % Ensure dy/dx<1
        j=j-1;
        % Upper & Lower bandwidth
        count=0;
        while abs(y(j)-yexp)<Wlb && j>1          % if y(x) is still within bandwidth of function
            Z(j,i)=hmax-abs(y(j)-yexp)*hmax/Wlb;    % determine height as function of position
            Z(j+2+count,i)=Z(j,i);                  % use the symmetry of the problem
            count=count+2;
            j=j-1;
        end
    end
end
%% Warning if angle gamma is poorly approximated
if count==0
   display('Note that angle gamma may be poorly displayed. Consider increasing the factor for smaller dy')
end
figure(1)
hold on
surf(CorX,CorY,Z)
plot((x+Wn),Ll/Wn*x-Ll,'r')
axis equal

%% add Sl/2 at boundaries
ns=1/2*sl/dy;                   % number of grid cells in y direction to span Sl
nsr=floor(ns);                  % rounded "           "
% ns must at least be equal to 4 to give a good representation of the
% riblet. If this is not the case the code will still work but give an
% imperfect representation
if ns<4
   display('Note that for current choice of discretization the riblet cannot be plotted completely due to the
end

error_s=(ns-nsr)*dy;            % error caused by rounding
yup=dy:dy:sl/2;
ydown=y(end)-dy:-dy:y(end)-sl/2;
[Corb,Ycorup]=meshgrid(x,yup);
[~,Ycordown]=meshgrid(x,ydown);
[size1,size2]=size(Corb);
Zb=zeros(size1,size2);

CorX=[Corb;CorX;Corb];
CorY=[flipud(Ycorup);CorY;Ycordown];
Z=[Zb;Z;Zb];
```

Appendix C

Schematics of flow shields

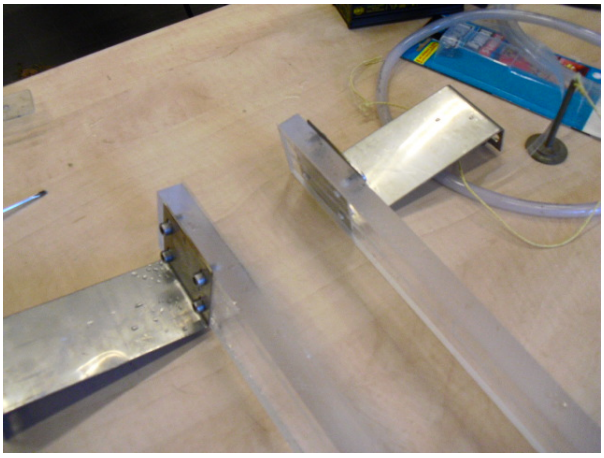

Figure C.1: Flow shields before mounting

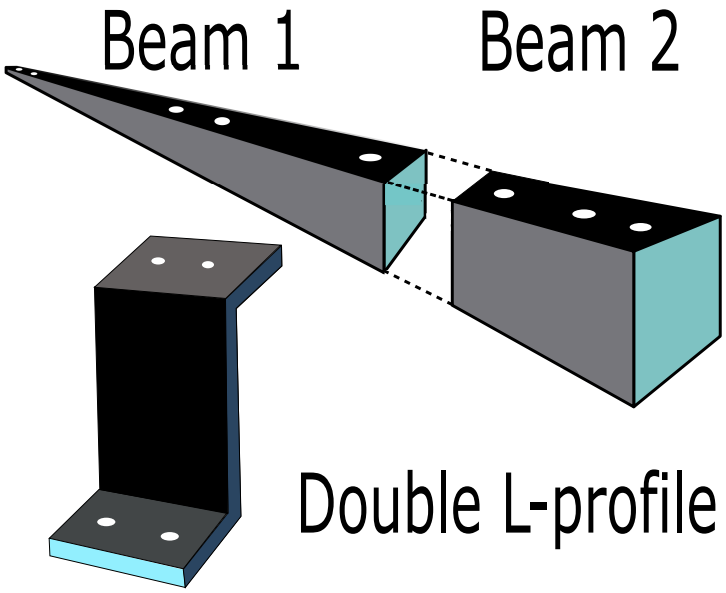

Figure C.2: Schematics of the flow shields components

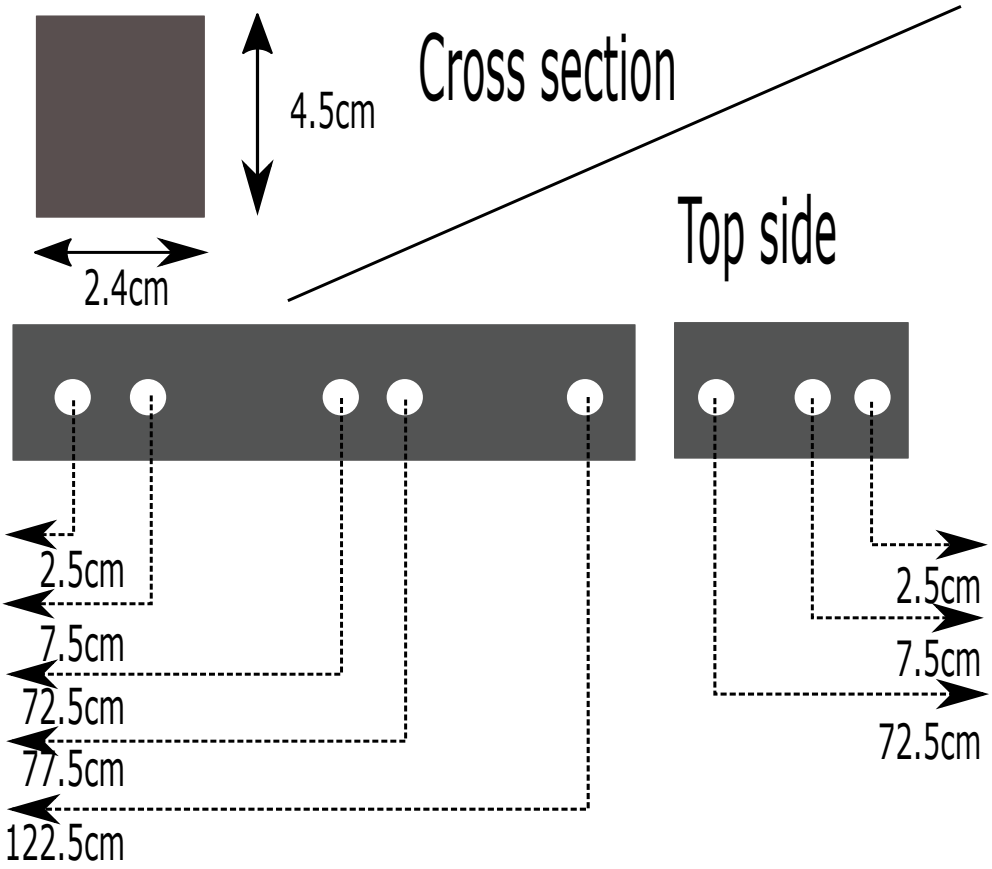

Figure C.3: Schematics of the beams

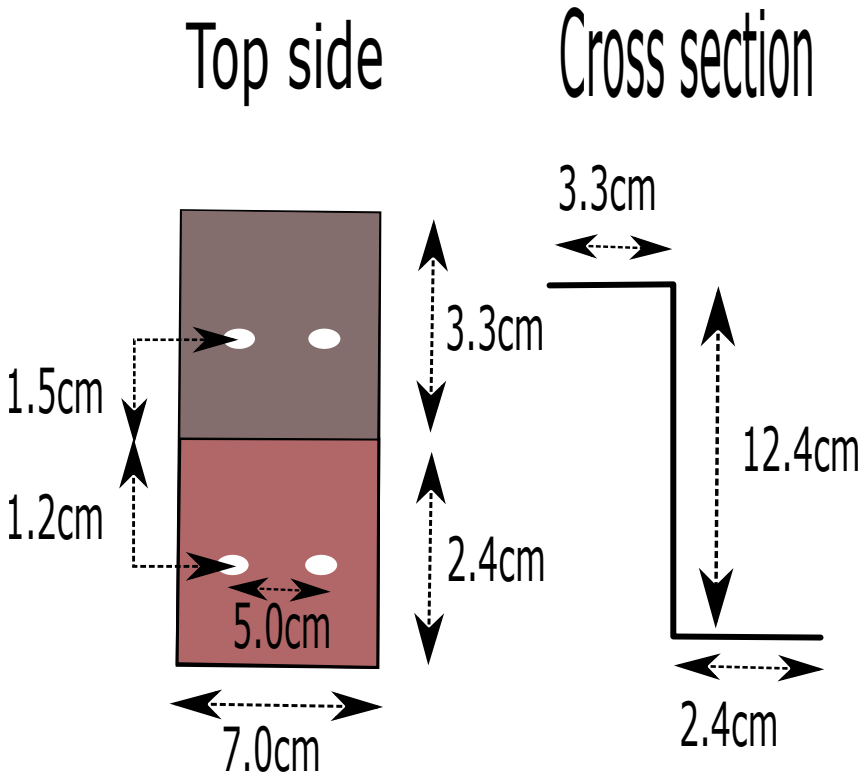

Figure C.4: Schematics of the profiles

Appendix D

Safety regulations PIV

Safety report regarding PIV measurements at the cavitation tunnel

date : 08-08-2016
version : no. 1

General Introduction

As part of a master and phd project it is planned to perform planar PIV measurements at the Cavitation Tunnel located behind the towing tank. As this measuring campaign requires usage of a Class 4 ND:YAG laser, which can cause permanent physical damage if ill handled, safety precautions should be followed. This report gives the details about the measurement setup and safety regulations that will be taken into effect according to regulations given by TU report no. 5-02 and no. 15-94 which are based on IAVM report no.12: "Richtlijnen laserveiligheid, voor research en onderwijs".
The given setup and measurement routines will be in effect for two different timeblocks, namely 22-31 August and 19 September/14 October of 2016.

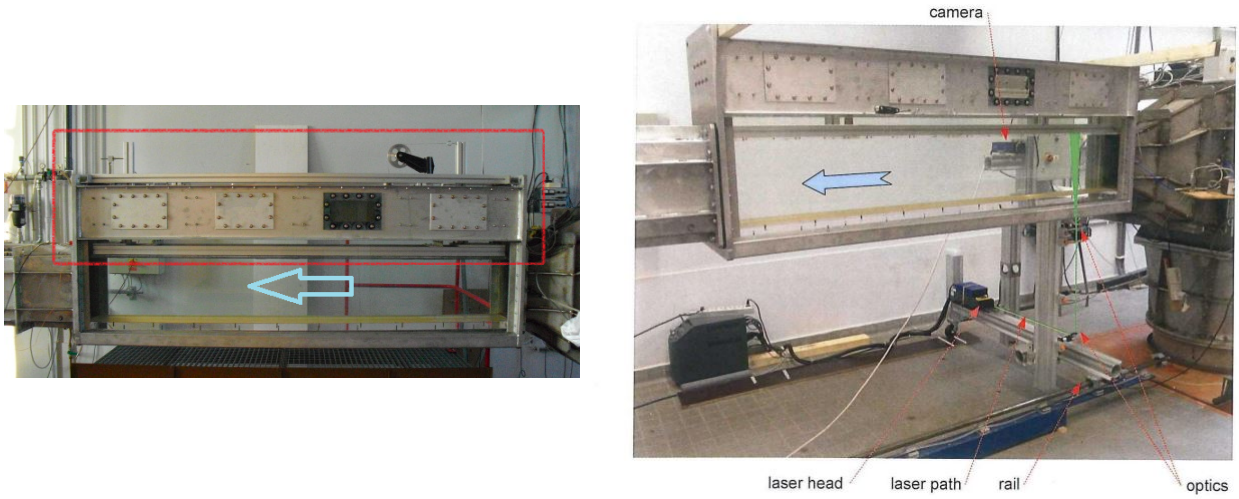

Figure D.1: Left: Test section
Right: Test section with laser setup [Zverkhovskyi,2014].

Measurement Setup

To evaluate the mean velocity, boundary layer and reynoldsstress profile over a flat plate a planar PIV system is constructed to capture this information simultaneously with the drag measurements, see fig.D.1 left. To accomplish this an external frame that holds both laser and camera will be constructed in similar fashion to the PHD work of O.Zverkhovskyi[1].
In this setup the laser beam is guided and directed perpendicular towards the test plate where the laser sheet is formed. The frame also allows for translation of the system in the flow direction, which is only done between tests. Measurements are estimated to last between 2 till 5 minutes.

Laser Specifications

The laser to be used is a Litron laser L-classe 50-50. Output energy at wavelength 532 nm is given to be 50 mJ. The operation modus of the laser will be around 50 Hz. The mean optical power of the laser is 2.5 W. With a laser beam of 4 mm this results in a power density of 5.3 $10^5 \frac{W}{m^2}$. The illuminated plane has dimensions 30cm, reducing the power density to $175 \frac{W}{M^2}$. During calibration these values can be reduced. For more specifacations see the appendix.

Safety routines

Laser beam covering

In order to protect the researcher, various laser blocking shields will be placed around the test section which minimalize scattered light. Furthermore the researcher will be positioned

Cavitation tunnel covering

To prevent scattered laser light from reaching bystanders the facility will be locked, see next paragraph. Furthermore any windows present in the facility will be blocked by thick absorbing curtains that prevent any light source from leaving (or entering) the facility.

Restriction of access to facility

The only access to the facility will be locked during the measurements from the inside, which can only be opened with the required key. In addition visuable warnings are present at the entrance, such as warning signs, lights and tape, emphasizing forbidden access while the door is locked and warning lights are displayed.

[1] O.Zverkhovskyie: Ship Drag Reduction by Air Cavities, 2014

Bibliography

R. J. Adrian and J. Westerweel. *Particle image velocimetry*. Number 30. Cambridge University Press, 2011.

T. Al-Shemmeri. *Engineering Fluid Mechanics*. Bookboon, 2012.

Baumerprocess. Cable sensor, pt100/pt1000, August 2016. URL `http://www.baumer.com/fileadmin/user_upload/international/Services/Download/Datenblaetter/PI/B1_Electronic_Temperature/Pt100_Pt1000_cablesensor_EN.pdf`.

D. Bechert, M. Bruse, W. Hage, J. T. Van der Hoeven, and G. Hoppe. Experiments on drag-reducing surfaces and their optimization with an adjustable geometry. *Journal of fluid mechanics*, 338:59–87, 1997.

A. Boomsma and F. Sotiropoulos. Riblet drag reduction in mild adverse pressure gradients: A numerical investigation. *International Journal of Heat and Fluid Flow*, 56:251–260, 2015.

C. Boyer, M. H. Stenzel, and T. P. Davis. Building nanostructures using raft polymerization. *Journal of Polymer Science Part A: Polymer Chemistry*, 49(3):551–595, 2011.

F. Charruault. *Cavity*. 2016.

H. Chen, F. Rao, X. Shang, D. Zhang, and I. Hagiwara. Flow over bio-inspired 3d herringbone wall riblets. *Experiments in fluids*, 55(3):1–7, 2014.

E. R. Corino and R. S. Brodkey. A visual investigation of the wall region in turbulent flow. *Journal of Fluid Mechanics*, 37(01):1–30, 1969.

B. Dean and B. Bhushan. Shark-skin surfaces for fluid-drag reduction in turbulent flow: a review. *Philosophical Transactions of the Royal Society of London A: Mathematical, Physical and Engineering Sciences*, 368(1929):4775–4806, 2010.

G. Elsinga and J. Westerweel. Tomographic-piv measurement of the flow around a zigzag boundary layer trip. *Experiments in fluids*, 52(4):865–876, 2012.

E.-J. Foeth. *The structure of three-dimensional sheet cavitation*. TU Delft, Delft University of Technology, 2008.

K. Fukagata, K. Iwamoto, and N. Kasagi. Contribution of reynolds stress distribution to the skin friction in wall-bounded flows. *Physics of Fluids*, 14(11):L73–L76, 2002.

R. Garcia-Mayoral and J. Jimenez. Hydrodynamic stability and breakdown of the viscous regime over riblets. *Journal of Fluid Mechanics*, 678:317–347, 2011.

W. Hage, D. Bechert, and M. Bruse. Yaw angle effects on optimized riblets. pages 278–285, 2001.

N. Hutchins and I. Marusic. Large-scale influences in near-wall turbulence. *Philosophical Transactions of the Royal Society of London A: Mathematical, Physical and Engineering Sciences*, 365(1852):647–664, 2007.

W. Jung, N. Mangiavacchi, and R. Akhavan. Suppression of turbulence in wall-bounded flows by high-frequency spanwise oscillations. *Physics of Fluids A: Fluid Dynamics (1989-1993)*, 4(8):1605–1607, 1992.

Y. Kametani and K. Fukagata. Direct numerical simulation of spatially developing turbulent boundary layers with uniform blowing or suction. *Journal of Fluid Mechanics*, 681:154–172, 2011.

J. Kim. Physics and control of wall turbulence for drag reduction. *Philosophical Transactions of the Royal Society of London A: Mathematical, Physical and Engineering Sciences*, 369(1940):1396–1411, 2011.

K. Kim, R. J. Adrian, S. Balachandar, and R. Sureshkumar. Dynamics of hairpin vortices and polymer-induced turbulent drag reduction. *Physical review letters*, 100(13):134504, 2008.

J. C. Klewicki. Reynolds number dependence, scaling, and dynamics of turbulent boundary layers. *Journal of fluids engineering*, 132(9):094001, 2010.

S. Kline, W. Reynolds, F. Schraub, and P. Runstadler. The structure of turbulent boundary layers. *J. Fluid Mech*, 30(4):741–773, 1967.

K. Koeltzsch, A. Dinkelacker, and R. Grundmann. Flow over convergent and divergent wall riblets. *Experiments in fluids*, 33(2):346–350, 2002.

E. T. Lee and J. Wang. *Statistical methods for survival data analysis*, volume 476. John Wiley & Sons, 2003.

S.-J. Lee and S.-H. Lee. Flow field analysis of a turbulent boundary layer over a riblet surface. *Experiments in fluids*, 30(2):153–166, 2001.

P. Luchini, F. Manzo, and A. Pozzi. Resistance of a grooved surface to parallel flow and cross-flow. *Journal of Fluid Mechanics*, 228:87–109, 1991.

I. Marengo. Mapping areas at risk of marine invasion from biofouling, march 2017.

I. Marusic, B. McKeon, P. Monkewitz, H. Nagib, A. Smits, and K. Sreenivasan. Wall-bounded turbulent flows at high reynolds numbers: Recent advances and key issues. *Physics of Fluids (1994-present)*, 22 (6):065103, 2010.

F. T. M. Nieuwstadt. *Turbulentie: inleiding in de theorie en toepassingen van turbulente stromingen*. Epsilon, 1992.

B. Nugroho. Highly ordered surface roughness effects on turbulent boundary layers. 2015.

B. Nugroho, N. Hutchins, and J. Monty. Large-scale spanwise periodicity in a turbulent boundary layer induced by highly ordered and directional surface roughness. *International Journal of Heat and Fluid Flow*, 41:90–102, 2013.

P. Orlandi and J. Jimenez. On the generation of turbulent wall friction. *Physics of Fluids (1994-present)*, 6(2):634–641, 1994.

R. L. Panton. Overview of the self-sustaining mechanisms of wall turbulence. *Progress in Aerospace Sciences*, 37(4):341–383, 2001.

A. Papoulis. *Signal analysis*, volume 191. McGraw-Hill New York, 1977.

P. Pennings. *Dynamics of Vortex Cavitation*. PhD thesis, TU Delft, Delft University of Technology, 2016.

S. B. Pope. Turbulent flows, 2001.

C. Pulles, K. K. Prasad, and F. Nieuwstadt. Turbulence measurements over longitudinal micro-grooved surfaces. *Applied Scientific Research*, 46(3):197–208, 1989.

S. K. Robinson. Coherent motions in the turbulent boundary layer. *Annual Review of Fluid Mechanics*, 23(1):601–639, 1991.

M. Sasamori, H. Mamori, K. Iwamoto, and A. Murata. Experimental study on drag-reduction effect due to sinusoidal riblets in turbulent channel flow. *Experiments in Fluids*, 55(10):1–14, 2014.

SEAFRONT. Synergistic fouling control technologies, march 2017.

J. S. Strand and D. B. Goldstein. Direct numerical simulations of riblets to constrain the growth of turbulent spots. *Journal of Fluid Mechanics*, 668:267–292, 2011.

S. Tamano, T. Kitao, and Y. Morinishi. Turbulent drag reduction of boundary layer flow with non-ionic surfactant injection. *Journal of Fluid Mechanics*, 749:367–403, 2014.

J. Taylor. *Introduction to error analysis, the study of uncertainties in physical measurements*. 1997.

TDB. High precision measurements, tdb. *ed: McGraw-Hill, Boston*, 2006.

H. Tennekes and J. L. Lumley. *A first course in turbulence*. MIT press, 1972.

T. Theodorsen. Mechanism of turbulence. In *Proceedings of the Second Midwestern Conference on Fluid Mechanics*, pages 1–18. Ohio State University, 1952.

A. Townsend. The properties of equilibrium boundary layers. *Journal of Fluid Mechanics*, 1(06):561–573, 1956.

UN. Adoption of the paris agreement, march 2015.

M. Walsh. Turbulent boundary layer drag reduction using riblets. In *20th aerospace sciences meeting*, page 169, 1982.

M. J. Walsh. Riblets as a viscous drag reduction technique. *AIAA journal*, 21(4):485–486, 1983.

F. M. White. Fluid mechanics, wcb. *ed: McGraw-Hill, Boston*, 1999.

F. M. White. Fluid mechanics,(2003), 2003.

O. Zverkhovskyi. *Ship drag reduction by air cavities*. TU Delft, Delft University of Technology, 2014.